Universität Hamburg
DER FORSCHUNG | DER LEHRE | DER BILDUNG

Advanced Fiber-Optic Ultrafast Laser Sources for Multiphoton Microscopy

Dissertation
zur Erlangung des Doktorgrades
an der
Fakultät für Mathemathik, Informatik und Naturwissenschaften,
Fachbereich Physik der Universität Hamburg

vorgelegt von
Hsiang-Yu Chung
am
16.11.2018

Gutachter: Prof. Dr. Franz X. Kärtner
Prof. Dr. Guoqing Chang

Date of oral defense: 17 June, 2019

The following evaluators recommend the admission of the dissertation:
Prof. Dr. Franz X. Kärtner
Prof. Dr. Daniela Pfannkuche
Prof. Dr. Nils Huse
Dr. Ingmar Hartl
Dr. Rüdiger Greinert

To my parents

Declaraction

I hereby declare that this dissertation and the work presented in it are my own and has been generated by me as the result of my own original research. The content of this dissertation has neither been accepted nor graded "failed" in a previous doctoral procedure. Any help that I have received in my research work and the preparation of the thesis itself has been acknowledged.

Hsiang-Yu Chung
Hamburg, November 2018

Acknowledgement

I would like to thank my supervisor Prof. Franz X. Kärtner for giving me the opportunity to work in his group in CFEL and pursue PhD in University of Hamburg. Prof. Kärtner provides me with not only abundant resources but also much freedom, so I can concentrate on the bio-imaging project. The results presented in this dissertation could not be achieved without his full support.

Also, I would like to thank my second supervisor Prof. Guoqing (Noah) Chang. I still remember how excited I was while receiving his recruiting email on holidays during my military service in November 2013, which is one of my most decisive moments. I benefit a lot from Noah, and I really enjoy our discussion about, but not restricted to science and research.

I would like to thank my previous supervisor Prof. Chi-Kuang Sun who encouraged me to study abroad. I was well trained in his group when I was a graduate student in Taiwan.

Besides my supervisors, I would like to especially thank our group secretary Christine Berber for taking care lots of administrative work, so I can focus on the research.

During the past few years, I was really lucky to work with many outstanding colleagues in the group and learn from them. Dr. Hung-Wen Chen taught me how to build up my very first fiber laser in 2012 even before I joined the group. Dr. Wei Liu helped me with the CPA system and fiber processing. Qian Cao provided numerical simulations and data analysis to support my experimental results. Dr. Liwei Song kindly provided his energetic OPA system, so we were able to conduct some proof-of-principle experiments. Prof. Shih-Hsuan Chia is very experienced in multiphoton microscopy.

The MPM application is very complementary and interdisciplinary between our collaborators and us. Therefore, I would like to thank Susanne Fengler for introducing me to Dr. Rüdiger Greinert—Head of Department of Molecular Cell Biology in Skin Cancer Center Buxtehude. Our collaboration started since 2015. Dr. Greinert kindly provided us with skin samples, so we can demonstrate optical virtual skin biopsy in Sec. 4.2, Sec. 4.3, and Sec. 5.2. I would like to thank Dr. Sarah Degenhardt, Dr. I-Peng Chen, and Stefan Henning for the sample preparation.

The work of protein crystal detection in Sec. 5.3 is in collaboration with Laboratory for Structural Biology of Infection and Inflammation of Prof. Christian Betzel. I learned a lot of knowledge of protein crystals while working with Qing-di Cheng, Dr. Robin Schubert, and Dr. Markus Perbandt.

Finally, I would like to thank my parents, my younger sister, and my friend Chenfei for supporting my decision to pursue PhD in Germany.

Abstract

As a powerful tool for bio-imaging, multiphoton microscopy (MPM) integrates two advanced technologies—ultrafast lasers and scanning microscope. The essence of MPM relies on the nonlinear interactions between ultrafast pulses and samples. Conventionally, the burden to drive MPM mainly falls on solid-state mode-locked lasers, e.g., Ti:sapphire lasers plus synchronously pumped optical parametric oscillators (OPOs), which operate at tens of MHz and generate ∼100-fs pulses with∼10-nJ pulse energy. However, these expensive solid-state solutions are bulky and sensitive to environmental fluctuations, and demand water cooling, which limit their further prevalence in biomedical applications.

Despite the limited emission wavelength, ultrafast fiber lasers exhibit robustness, compactness, and cost-effectiveness, which make them a potential alternative to driving MPM. Together with nonlinear fiber-optic wavelength conversion, femtosecond pulses at new wavelength can be readily generated for MPM. Recently, we demonstrated a new approach to achieve widely tunable energetic pulses desired by MPM applications. The method—self-phase modulation enabled spectral selection (SESS)—employs self-phase modulation (SPM) dominated spectral broadening in optical fibers to broaden an input narrowband spectrum. The broadened spectrum features well-isolated spectral lobes; filtering the leftmost or the rightmost spectral lobes results in nearly transform-limited pulses. For example, SESS based on an Yb-doped fiber laser (YDFL) centered at 1030 nm, allows us to generate ∼100-fs pulses tunable from 825 nm to 1210 nm. The resulting spectrum supports driving two-photon excitation fluorescence (2PEF) of many important fluorophores and harmonic generation microscopy (HGM) including second-harmonic generation (SHG) and third-harmonic generation (THG).

Inspired by the success of SESS enabled by 1-μm YDFLs, we further explored the wavelength coverage allowed by other fiber-based SESS sources. In this thesis, we implemented SESS based on a home-built Er-doped fiber laser (EDFL) centered at 1.55 μm—a unique wavelength right between two important biological transmission windows at 1.3 μm and 1.7 μm for deep-tissue imaging. We numerically and experimentally investigated SESS operating in optical fibers exhibiting different dispersions. With a 31-MHz EDFL emitting 160-nJ, 290-fs pulses, SESS generated ∼100-fs pulses widely tunable between 1.15 μm and 1.7 μm with up to >15-nJ pulse energy. We also demonstrated that SESS is feasible in optical fibers with anomalous dispersion, in which the spectral broadening is still dominated by SPM and one benefits from higher-order soliton compression, as long as one stays away from soliton fission. SESS exhibits outstanding energy scalability. With a μJ pump source, one can achieve femtosecond pulses at 1.3 μm or 1.7 μm with pulse energies exceeding 100 nJ, corresponding to a pulse peak power at the MW level.

We integrated this EDFL-based SESS source with a scanning microscope and demonstrated various MPM applications. For example, we conducted optical virtual biopsy in human skin enabled by HGM excited by 1.25-μm femtosecond pulses. We also investigated the effect of excitation wavelength within the transmission window of 1.15-1.35 μm on the resulting HGM imaging. Conventionally, the wavelength coverage is provided by solid-state OPOs or Cr:forsterite lasers. By frequency doubling part of the beam to 775 nm, the EDFL constitutes a two-color ultrafast source enabling multimodal MPM. Besides HGM demonstrated in human skin, 2PEF from the intrinsic fluorophores is available under 775-nm excitation, which allows 3-channel (SHG, THG, and 2PEF) label-free skin imaging. It is noteworthy that 775-nm excitation can also lead to three-photon excitation fluorescence (3PEF) from the amino aromatic acids of proteins. Combining with SHG together, the SHG/3PEF modality enabled us to detect and distinguish protein crystals from salt crystals.

In conclusion, we demonstrate an EDFL-based ultrafast source harnessing nonlinear fiber-optics enabling widely tunable femtosecond pulses for versatile MPM. Such a fiber-based source constitutes an alternative to solid-state lasers and has a great potential for clinical applications.

Zusammenfassung

Multiphotonen-Mikroskopie (MPM) ist eine der wichtigsten Anwendungen von Ultrakurzpuls-Lasern und ein leistungsfähiges Werkzeug für die biomedizinische Bildgebung. Die Essenz von MPM beruht auf der Wechselwirkung zwischen den ultraschnellen Laserimpulsen und der Probe, die auf unterschiedlichen Mechanismen beruht. Herkömmlicherweise wird MPM hauptsächlich mittels Festkörperlasern betrieben, z. B. Ti:Saphir-Laser plus einen synchron gepumpten optischen parametrischen Oszillator (OPO), die bei einigen-zehn-MHz Pulswiederholrate betrieben werden, Impulse mit etwa 10-nJ Impulsenergie und etwa 100-fs Impulsdauer erzeugen, und eine bestimmte Wellenlängenabstimmbarkeit besitzen. Diese Festkörperlösungen sind jedoch sperrig, benötigen Wasserkühlung, sind empfindlich gegenüber Umweltschwankungen und teuer, welches die weitere Verbreitung von MPM in biologischen Studien und in der klinischen Anwendung begrenzt.

Trotz der begrenzten Emissionswellenlänge sind faserbasierte Ultrakurzpulslaser, die Robustheit, Kompaktheit und kosteneffektives Merkmal aufweisen, in letzter Zeit zu einer potentiellen Alternative zum Antreiben von MPM geworden. Durch den Einsatz verschiedener nichtlinearer faseroptischer Methoden können neue Spektren für MPM erzeugt werden. Vor kurzem haben wir einen neuen Ansatz demonstriert, um weit abstimmbare hochenergetische Impulse für eine solche Anwendung zu erreichen. Das Verfahren—durch Selbstphasenmodulation Spektralselektion (SESS)—verwendet eine von der Selbstphasenmodulation (SPM) dominierte spektrale Verbreiterung in der optischen Faser, gefolgt von einer Filterung der am weitesten links oder der am weitesten rechts liegenden spektralen Keulen der daraus resultierenden Spektren. Zum Beispiel ermöglicht die Verwendung eines Yb-dotierten Faserlasers (YDFL), der bei 1030 nm als Pumpquelle zentriert ist, SESS zur Erzeugung von nahezu transform-limitierten Impulsen, die von 825 nm bis 1210 nm abstimmbar sind. Das resultierende Spektrum ist vergleichbar mit dem von Ti: Saphir-Lasern und unterstützt die Zwei-Photonen-Fluoreszenz (2PEF) vieler wichtiger Fluorophore und die harmonische Generationsmikroskopie (HGM), einschließlich Frequenzverdopplung (SHG) und Frequenzverdreifachung (THG).

Inspiriert durch den Erfolg von SESS mit 1-μm YDFLs erforschen wir hier die weitere Wellenlängenabdeckung, die mittels anderer faserbasierter SESS-Quellen möglich ist. In dieser Doktorarbeit implementieren wir SESS basierend auf einem selbst gebauten Er-dotierten Faserlaser (EDFL), der bei 1,55 μm zentriert ist—eine einzigartige Wellenlänge genau zwischen zwei wichtigen biologischen Transmissionsfenstern bei 1,3 μm und 1,7 μm für die Tiefengewebe-Bildgebung. Wir untersuchen numerisch und experimentell SESS, das optische Fasern mit unterschiedlicher Dispersion benutzt. Mit einer 31-MHz-EDFL-Pumpquelle, die Pulse mit 160 nJ Pulsenergie und 290 fs Pulsdauer erzeugt, kann SESS zu Pulsen führen, die abstimmbar zwischen 1,15 μm und 1,7 μm sind, >15 nJ Pulsenergie und Pulsdauern kürzer als 100 fs haben. Wir zeigen auch, dass SESS in optischen Fasern mit anomaler Dispersion machbar ist, in denen die spektrale Verbreiterung immer noch durch den SPM-Effekt dominiert wird und durch Soliton-Kompression höherer Ordnung begünstigt wird, solange man Soliton-Spaltung vermeidet. SESS weist

eine herausragende Energie-Skalierbarkeit auf. Mit einer μJ-Pumpquelle kann man Femtosekundenpulse bei 1,3 μm oder 1,7 μm mit einer Pulsenergie von mehr als 100 nJ erreichen, was einer Pulsspitzenleistung im MW-Bereich entspricht.

Wir integrieren diese EDFL-basierte SESS-Quelle mit einem Scanning-Mikroskop und demonstrieren ihre Anwendung für MPM. Zum Beispiel führen wir eine optische virtuelle Biopsie der menschlichen Haut durch, die durch HGM aktiviert wird, und Femtosekundenimpulse bei 1,25 μm verwendet. Wir untersuchen auch den Einfluß der Anregungswellenlänge im Transmissionsfenster von 1,15-1,35 μm auf die resultierende HGM-Bildgebung. Herkömmlicherweise werden in diesem Wellenlängenbereich Festkörper-OPOs oder Cr:Forsterit-Laser benutzt. Durch die Frequenzverdopplung eines Teils des Pumpstrahls auf 775 nm bildet der EDFL eine zweifarbige ultraschnelle Quelle, die ein multimodales MPM ermöglicht. Neben HGM, das in der menschlichen Haut demonstriert wurde, steht 2PEF aus den intrinsischen Fluorophoren unter 775-nm Anregung zur Verfügung, was 3-Kanal (SHG, THG und 2PEF) markierungsfreie Hautbildgebung ermöglicht. Es ist bemerkenswert, dass eine 775-nm Anregung zu einer Drei-Photonen-Fluoreszenz (3PEF) von den aminoaromatischen Säuren des Proteins führen kann. Durch die Kombination mit SHG ermöglicht die SHG/3PEF-Modalität die Erkennung und Unterscheidung von Proteinkristallen und Salzkristallen.

Zusammenfassend demonstrieren wir eine EDFL-basierte ultraschnelle Quelle, die nichtlineare Faseroptiken nutzt und breit abstimmbare Femtosekundenpulse für vielseitige MPM ermöglicht. Eine solche faserbasierte Quelle stellt eine robuste und kostengünstige Alternative zu Festkörperlasern dar und ist für klinische Anwendungen geeignet.

List of Publications

Journal Articles

1. Q.-D. Cheng, **H.-Y. Chung**, R. Schubert, S.-H. Chia, G. Q. Chang, F. X. Kärtner, M. Perbandt, and C. Betzel, "Multiphoton microscopy for nanocrystal detection and scoring driven by a fiber-based ultrafast source," manuscript in preparation (2018).

2. **H.-Y. Chung**, R. Greinert, F. X. Kärtner, and G. Q. Chang, "Multimodal imaging platform for optical virtual skin biopsy enabled by a fiber-based two-color ultrafast source," submitted to *Biomed. Opt. Express* (2018).

3. **H.-Y. Chung**, W. Liu, Q. Cao, R. Greinert, F. X. Kärtner, and G. Q. Chang, "Tunable, ultrafast fiber-laser between 1.15 and 1.35 μm for harmonic generation microscopy in human skin," *IEEE J. Sel. Topics in Quantum Elec.* 25(1), 6800708 (2019).

4. **H.-Y. Chung**, W. Liu, Q. Cao, L. W. Song, F. X. Kärtner, and G. Q. Chang, "Megawatt peak power tunable femtosecond source based on self-phase modulation enabled spectral selection," *Opt. Express* 26(3), 3684–3695 (2018).

5. **H.-Y. Chung**, W. Liu, Q. Cao, F. X. Kärtner, and G. Q. Chang, "Er-fiber laser enabled, energy scalable femtosecond source tunable from 1.3 to 1.7 μm," *Opt. Express* 25(14), 15760–15771 (2017).

6. W. Liu, S.-H. Chia, **H.-Y. Chung**, R. Greinert, F. X. Kärtner, and G. Q. Chang, "Energetic ultrafast fiber laser sources tunable in 1030-1215 nm for deep tissue multi-photon microscopy," *Opt. Express* 25(6), 6822–6831 (2017).

Conference Proceedings

1. **H.-Y. Chung**, W. Liu, R. Greinert, F. X. Kärtner, and G. Q. Chang, "Novel fiber-based ultrafast platform for multimodal optical virtual skin biopsy," in *Laser Congress 2018 (ASSL)*, OSA Technical Digest (Optical Society of America, 2018), paper ATh5A.2.

2. **H.-Y. Chung**, W. Liu, R. Greinert, F. X. Kärtner, and G. Q. Chang, "Ultrafast sources for optical virtual skin biopsy: a fiber-based solution to pulses at 1250 nm," in *Frontiers in Optics/Laser Science*, OSA Technical Digest (Optical Society of America, 2018), paper JTu2A.116.

3. S.-H. Chia, **H.-Y. Chung**, W. Liu, F. X. Kärtner, and G. Q. Chang, "Deep tissue multiphoton microscopy based on advanced femtosecond fiber sources," in *2018 20th International Conference on Transparent Optical Networks (ICTON)*, paper Th.B6.1.

4. **H.-Y. Chung**, W. Liu, Q. Cao, R. Greinert, F. X. Kärtner, and G. Q. Chang, "Excitation wavelength optimization of harmonic generation microscopy in human skin enabled by fiber-based femtosecond source tunable in 1.15-1.35 μm," in *Conference on Lasers and Electro-Optics*, OSA Technical Digest (online) (Optical Society of America, 2018), paper AM1J.2.

5. **H.-Y. Chung**, L. W. Song, W. Liu, Q. Cao, F. X. Kärtner, and G. Q. Chang, "Megawatt peak power femtosecond source at 1.3 μm based on self-phase modulation enabled spectral selection," in *Conference on Lasers and Electro-Optics*, OSA Technical Digest (online) (Optical Society of America, 2018), paper SM4K.4.

6. **H.-Y. Chung**, W. Liu, Q. Cao, R. Greinert, F. X. Kärtner, and G. Q. Chang, "Virtual skin biopsy enabled by ultrafast fiber source tunable between 1.15 and 1.35 μm," in *Focus on Microscopy 2018*, paper: TU-AF1-PAR-C.3.

7. **H.-Y. Chung**, W. Liu, F. X. Kärtner, and G. Q. Chang, "SPM-enabled femtosecond source tunable from 1.3 to 1.7 μm for multi-photon excitation microscopy," in *Ultrafast Optics 2017*, paper: P1-12.

8. **H.-Y. Chung**, W. Liu, Q. Cao, and G. Q. Chang, "Er-fiber laser enabled femtosecond source tunable from 1.3 to 1.7 μm for nonlinear optical microscopy," in *Conference on Lasers and Electro-Optics*, OSA Technical Digest (online) (Optical Society of America, 2017), paper: SM3L.2.

9. **H.-Y. Chung**, W. Liu, F. X. Kärtner, and G. Q. Chang, "Femtosecond source widely tunable from 1.3 to 1.7 μm for three-photon microscopy," in *Focus on Microscopy 2017*, paper: P1-A/4.

10. S.-H. Chia, **H.-Y. Chung**, W. Liu, F. X. Kärtner, and G. Q. Chang, "Multiphoton microscopy based on 1 GHz - 1 MHz energetic tunable ultrafast fiber sources," in *Focus on Microscopy 2017*, paper: SU-AF-PAR-D.3.

11. W. Liu, S.-H. Chia, **H.-Y. Chung**, F. X. Kärtner, and G. Q. Chang, "Energy scalable ultrafast fiber laser sources tunable in 1030-1200 nm for multiphoton microscopy," in *Lasers Congress 2016 (ASSL, LSC, LAC)*, OSA Technical Digest (online) (Optical Society of America, 2016), paper: ATh1A.5.

12. W. Liu, C. Li, **H.-Y. Chung**, S.-H. Chia, Z. G. Zhang, F. X. Kärtner, and G. Q. Chang, "Ultrafast laser source tunable in 825-1210 nm for multi-photon microscopy," in *Euro-Photon 2016*, paper: FWG-3.

13. W. Liu, C. Li, **H.-Y. Chung**, S.-H. Chia, Z. G. Zhang, F. X. Kärtner, and G. Q. Chang, "Widely tunable ultrafast source for multi-photon microscopy," in *Conference on Lasers and Electro-Optics*, OSA Technical Digest (online) (Optical Society of America, 2016), paper: SM2I.7.

14. S.-H. Chia, **H.-Y. Chung**, W. Liu, F. X. Kärtner, and G. Q. Chang, "Virtual skin biopsy based on ultrafast fiber lasers," in *Focus on Microscopy 2016*, paper: WE-MO1-PAR-D.5.

15. **H.-Y. Chung**, W. Liu, S.-H. Chia, F. X. Kärtner, and G. Q. Chang, "Fiber-nonlinearity enabled femtosecond laser sources for nonlinear light microscopy," in *Focus on Microscopy 2016*, paper: P1-C/32.

Contents

List of Figures

List of Tables

Chapter 1

Introduction

Multiphoton microscopy (MPM), also known as nonlinear optical microscopy (NLOM), demands ultrafast pulses as the driving source, and the conventional solution mainly relies on solid-state lasers. In recent years, fiber lasers are becoming more and more important because they are robust, compact, and cost-effective. In this thesis, we demonstrate novel fiber-based tunable ultrafast sources for driving MPM. Before we present the results, we first introduce in this chapter common modalities of MPM and the requirements for the driving source. Then we review the current commercially available solutions and the development of fiber-optic approaches to drive MPM.

1.1 Multiphoton microscopy

Optical microscope featuring sub-μm optical resolution is a powerful tool for bio-imaging. The Rayleigh criterion, which sets the standard of lateral resolution of an optical microscope, is defined by

$$r = \frac{1.22\lambda}{2n\sin\theta} = \frac{0.61\lambda}{NA} \tag{1.1}$$

where r is the minimum distance between resolvable points, λ the illumination wavelength, n the refractive index of the media surrounding the radiating points, θ the half angle of the pencil of light that enters the objective, and NA the numerical aperture of the objective.

As a result, the lateral resolution can be improved either by employing illumination with shorter wavelength or by using objectives with higher NA. However, the actual performance usually cannot reach such level since the conventional wide-field optical microscope lacks for sectioning ability. The imaging is not background free—light scattered from the non-focal plane contributes to the background and blurs the image, thus degrades the lateral resolution.

In 1957, Marvin Minsky demonstrated confocal microscopy that can improve the lateral resolution by integrating pinholes into the microscope system. In this scheme, pinholes as a spatial filter are aligned to select only the light reflected from the same focal plane and block those scattered from the non-focal plane. The lateral resolution can be improved by using smaller pinholes, but the associated signal-to-noise ratio (SNR) becomes lower because the pinhole blocks part of the signal light as well. A trade-off between the resolution improvement and SNR is a drawback for confocal microscopy. Increasing the illumination power seems a straightforward solution to this issue; however, it also increases the risk of damaging the sample, especially for biological tissues.

The invention of laser and the development of ultrafast sources have stimulated the progress of nonlinear optics, which provides an alternative to confocal microscopy to achieve intrinsic 3D sectioning ability without using pinholes. The nonlinear dependence of dielectric polarization P on the electric field E of light can be expressed as [1]

$$P = \chi^{(1)}E + \chi^{(2)}EE + \chi^{(3)}EEE + ... \tag{1.2}$$

where $\chi^{(n)}$ is the n_{th}-order susceptibility. Compared with the linear term $\chi^{(1)}E$, the second-order term $\chi^{(2)}EE$ and the third-order term $\chi^{(3)}EEE$ are proportional to the square and the cubic power of the electric field, respectively. These higher-order terms are sensitive to the variation of light intensity. This feature can be utilized to realize 3D sectioning ability by combing an ultrafast laser and a high-NA objective. The sectioning ability is automatically achieved without using pinholes because the nonlinear optical process can only occur efficiently in a small volume near the objective focus where the light intensity reaches the maximum. Depending on the interaction between ultrafast pulses and the samples, different mechanisms are applicable to MPM and lead to three common modalities:

1. Harmonic generation (HG) is related to the sample's geometric structure. For example, second-harmonic generation (SHG) is due to optical non-centrosymmetry, and third-harmonic generation (THG) comes from optical inhomogeneity.

2. Multiphoton excitation fluorescence (MPEF)—e.g., 2-photon excitation fluorescence (2PEF) and 3-photon excitation fluorescence (3PEF)—is the fluorescence emission induced by the absorption of multiple photons. They are related to the electronic states of the fluorophores.

3. Coherent Raman scattering (CRS) employs the vibration of molecular bonds. They can be conducted either by coherent anti-Stokes Raman scattering (CARS) or stimulated Raman scattering (SRS).

In this thesis, we discuss only HG and MPEF, which can be realized by a single excitation beam. To conduct CRS, one requires two beams—one as the pump beam and another one as the Stokes beam, of which the energy difference corresponds to the vibrational states of the molecular bond.

1.1.1 Harmonic generation

Optical HG is the nonlinear process that n photons with the same frequency ω (wavelength λ) interact with a sample and generates one photon with new frequency $n\omega$ (wavelength λ/n). Different from MPEF, HG involves no photon absorption by the sample and electron transition between real energy states. SHG ($n = 2$) and THG ($n = 3$) are the most common HG processes.

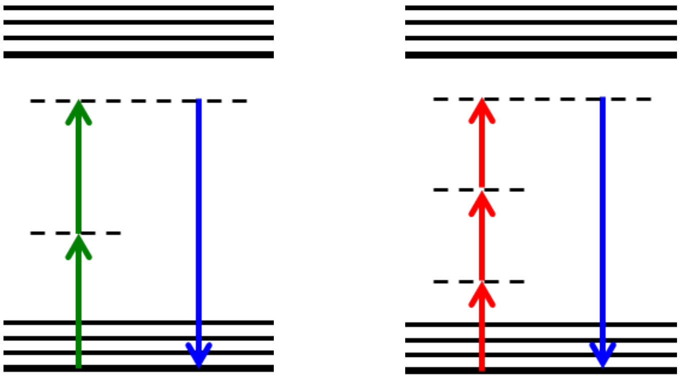

(a) SHG (b) THG

Figure 1.1: Jablonski diagrams of (a) SHG and (b) THG process.

In Fig. 1.1 we depict the Jablonski diagrams of SHG and THG process. The thick black lines are the electronic energy states, thin black lines the vibrational states, and dashed black lines the virtual energy states. Mainly depending on the sample's intrinsic geometric structure, SHG and THG can serve as contrast agents for harmonic generation microscopy (HGM).

SHG. Assuming an electric field of a laser beam can be described as [1]

$$\widetilde{E}(t) = \frac{1}{2}\left[E(\omega)e^{-i\omega t} + E(-\omega)e^{i\omega t}\right] \tag{1.3}$$

Then the resulting second-order nonlinear polarization is

$$\begin{aligned}\widetilde{P}^{(2)}(t) &= \epsilon_0\chi^{(2)}\widetilde{E}(t)^2 \\ &= \epsilon_0\chi^{(2)}(0:\omega,-\omega)EE^* + \frac{1}{4}\epsilon_0\chi^{(2)}(2\omega:\omega,\omega)E^2e^{-i2\omega t} + c.c.\end{aligned} \tag{1.4}$$

According to the wave driven equation

$$\left(\nabla^2 - \mu_0\sigma\frac{\partial}{\partial t} - \mu_0\epsilon\frac{\partial^2}{\partial t^2}\right)\tilde{E} = \mu_0\frac{\partial^2\tilde{P}}{\partial t^2} \tag{1.5}$$

The first term $\chi^{(2)}(0:\omega,-\omega)$ on the right-hand side of Eq. 1.4 contributes to zero frequency, and generates no electromagnetic field since its second derivative is zero.

This process is also known as optical rectification, which leads to a static electric field. The second-order term $\chi^{(2)}(2\omega:\omega,\omega)$ contributes to 2ω frequency, which is related to the process of SHG. When SHG occurs, one photon of frequency 2ω is generated while two photons of frequency ω vanishing simultaneously. The intensity of the induced SHG is proportional to the square power of the excitation light.

If we change the sign of the electric field in Eq. 1.4, the sign of the induced polarization will also change, leading to

$$-\tilde{P}^{(2)}(t) = \epsilon_0\chi^{(2)}\left[-\tilde{E}(t)^2\right] = \epsilon_0\chi^{(2)}\tilde{E}(t)^2 \tag{1.6}$$

In comparison with Eq. 1.4 again, then

$$\tilde{P}^{(2)}(t) = -\tilde{P}^{(2)}(t) \tag{1.7}$$

This validates only when $\tilde{P}^{(2)}(t)$ vanishes, indicating that $\chi^{(2)}$ is zero. As a result, SHG can not be observed in the material with centrosymmetry (possessing center of inversion). It is allowed only in material with non-centrosymmetry.

The first observation of SHG was in 1961, just one year after the invention of laser, by focusing a 694-nm ruby laser beam into a quartz sample and resulting in light with wavelength of 347 nm [2]. The first SHG imaging was from polycrystalline ZnSe demonstrated in 1974 [3]. In 1986, SHG imaging was used to study the orientation of collagen fibers in rat tail tendon [4]. Since then, SHG microscopy had been applied to various biological studies, e.g., membrane potentials [5, 6, 7, 8], microtubule polarity [4, 9, 10], extracellular matrix structure [11, 12, 13], and cellular structure [14].

THG. The third-order nonlinear polarization is

$$\begin{aligned}\tilde{P}^{(3)}(t) &= \epsilon_0\chi^{(3)}\tilde{E}(t)^3\\ &= \frac{1}{8}\left[\epsilon_0\chi^{(3)}(3\omega:\omega,\omega,\omega)E^3e^{-i3\omega t} + 3\chi^{(3)}(\omega:\omega,0,0)E^2E^*e^{-i\omega t}\right] + c.c.\end{aligned} \tag{1.8}$$

Considering only the real part leads to

$$\frac{1}{4}\epsilon_0\chi^{(3)}(3\omega:\omega,\omega,\omega)E^3\cos 3\omega t + \frac{3}{4}\epsilon_0\chi^{(3)}(\omega:\omega,0,0)\left|E\right|^2 E\cos\omega t \tag{1.9}$$

The first term $\chi^{(3)}(3\omega:\omega,\omega,\omega)$ on the right hand side of Eq. 1.8 contributes to 3ω frequency, which is related to the THG process. Unlike SHG, THG intensity is proportional to the cubic power of the excitation light. When it occurs, one photon of frequency 3ω is generated while three photons of frequency ω vanishing simultaneously.

The term $\chi^{(3)}(\omega:\omega,0,0)$ contributes to ω frequency the same as the incident light, which leads to a third-order contribution to the refractive index experienced by a wave of frequency ω, known as optical Kerr effect.

$\chi^{(3)}$ does not vanish when we change the sign of the electric field. This allows THG observed in materials with all kinds of structure, including centrosymmetry. However, for a strongly focused laser beam we have to consider the Gouy phase shift, which introduces a π phase shift to the beam after passing the focus and renders a destructive interference between the THG before and after the focus. As a result, THG can not occur for a laser beam focused in a homogeneous sample. This explains why THG is sensitive to optical inhomogeneity and able to detect interfaces.

THG from a simple air-dielectric interface was demonstrated in 1995 [15]. It was also found in animal tissues [16]. The first THG imaging was performed in 1997 from an optical fiber [17]. THG microscopy were widely applied to morphological studies and interfacial imaging of cellular and subcellular organelles [18, 19, 20, 21, 22].

1.1.2 Multiphoton excitation fluorescence

The process of fluorescence is related to the photon absorption and electron transitions between real states. Common one-photon excitation fluorescence (1PEF) can be described in three steps shown in Fig. 1.2(a). First, a single excitation photon is absorbed by a fluorophore, resulting in its electron from the electronic ground state to an excited state. After the non-radiative vibrational relaxation accompanying part of the excitation energy dissipated as heat, the fluorophore returns to the ground state and emits a photon with longer wavelength compared with the incident beam. For MPEF, the process in the first step can be replaced by the absorption of multiple photons with less energy as long as the total amount of photon energy exceeds the energy gap between the ground state and the excited state of the fluorophore.

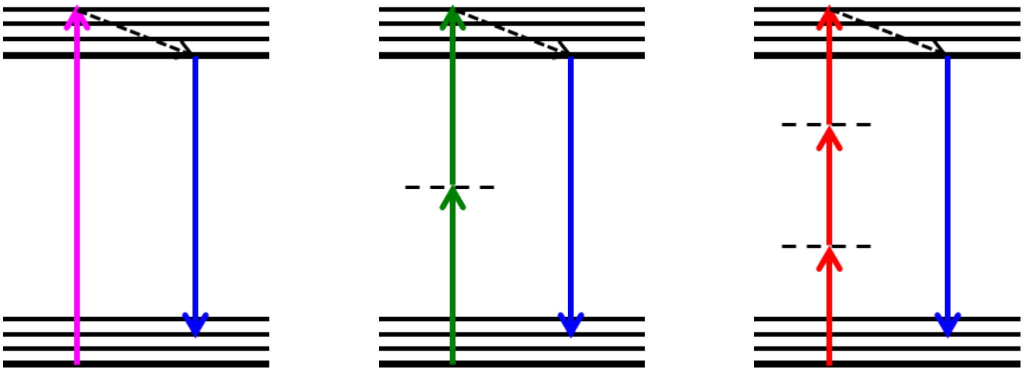

(a) 1PEF (b) 2PEF (c) 3PEF

Figure 1.2: Jablonski diagram of MPEF processes.

2PEF. The process of 2PEF is depicted in the Jablonski diagram in Fig. 1.2(b). The discussion in section 1.1.1 about HG and optical Kerr effect relates to only virtual state transitions and the real part of Eq. 1.3. However, we should also consider the imaginary part in real state transitions, such as absorption. Considering $\chi^{(3)}$ and the constitutive law, then we can derive

$$\begin{aligned}
\tilde{D} &= \epsilon\tilde{E} \\
&= \epsilon_0\tilde{E} + \tilde{P} \\
&= \epsilon_0\tilde{E} + \tilde{P}^{(1)} + \tilde{P}^{(3)} \\
&= \epsilon_0\tilde{E} + \epsilon_0\left(\mathrm{Re}\chi^{(1)} + i\mathrm{Im}\chi^{(1)}\right)\tilde{E} + \epsilon_0\left(\frac{3}{4}\mathrm{Re}\chi^{(3)}\left|\tilde{E}\right|^2 + \frac{3}{4}\mathrm{Im}\chi^{(3)}\left|\tilde{E}\right|^2\right)\tilde{E} \\
&= \epsilon_0\tilde{E} + \epsilon_0\left(\mathrm{Re}\chi^{(1)} + \frac{3}{4}\mathrm{Re}\chi^{(3)}\left|\tilde{E}\right|^2\right)\tilde{E} + i\epsilon_0\left(\mathrm{Im}\chi^{(1)} + \frac{3}{4}\mathrm{Im}\chi^{(3)}\left|\tilde{E}\right|^2\right)\tilde{E} \\
&= \epsilon_0(1 + \mathrm{Re}\chi + \mathrm{Im}\chi)\tilde{E}
\end{aligned} \tag{1.10}$$

where $\mathrm{Re}\chi = \mathrm{Re}\chi^{(1)} + \frac{3}{4}\mathrm{Re}\chi^{(3)}\left|\tilde{E}\right|^2$, $\mathrm{Im}\chi = \mathrm{Im}\chi^{(1)} + \frac{3}{4}\mathrm{Im}\chi^{(3)}\left|\tilde{E}\right|^2$

Assuming the electric field of a propagating plane wave is

$$\tilde{E} = E_0 e^{ikz} e^{-i\omega t} \tag{1.11}$$

where z direction is the propagation direction.

The relation between the wave number k and the susceptibility χ can be presented as

$$\begin{aligned}
k &= \omega\sqrt{\mu\epsilon} \\
&= \omega\sqrt{\mu\epsilon_0\left(\mathrm{Re}\chi + \mathrm{Im}\chi\right)} \\
&= \frac{\omega}{c}\left(1 + \mathrm{Re}\chi\right)^{1/2}\left(1 + \frac{i\mathrm{Im}\chi}{1 + \mathrm{Re}\chi}\right)^{1/2} \\
&\simeq \frac{\omega n}{c} + i\frac{\omega}{2cn}\mathrm{Im}\chi \\
&= \mathrm{Re}k + i\mathrm{Im}k
\end{aligned} \tag{1.12}$$

where $n = (1 + \mathrm{Re}\chi)^{1/2}$ is the optical refractive index.

After substitution, the electric field becomes:

$$\tilde{E} = E_0 e^{i\mathrm{Re}kz - \omega t} e^{-\mathrm{Im}kz} \tag{1.13}$$

where $\mathrm{Im}k$ corresponds to absorption.

Considering Eq. 1.12 and Eq. 1.13, then we can get:

$$\frac{d\tilde{E}}{dz} \propto (i\mathrm{Re}k - \mathrm{Im}k) = i\mathrm{Re}k - \frac{\omega}{2cn}\left(\mathrm{Im}\chi^{(1)} + \frac{3}{4}\mathrm{Im}\chi^{(3)}I\right) \tag{1.14}$$

where $I = \frac{n_0}{2}\sqrt{\frac{\epsilon_0}{\mu_0}}\left|E\right|^2$ is the intensity of excitation. The term $\mathrm{Im}\chi^{(1)}$ and $\mathrm{Im}\chi^{(3)}$ contribute to linear and nonlinear absorption respectively. If we introduce E_{2p} as the two-photon absorbed electric field strength, the nonlinear contribution can be shown as

$$\left|\frac{dE_{2p}}{dz}\right| = \frac{3}{4}\left|\frac{\omega}{cnn_0}\mathrm{Im}\chi^{(3)}\sqrt{\frac{\mu_0}{\epsilon_0}}\right| \tag{1.15}$$

If the intensity of nonlinear absorption is

$$I_{2p} = E_{2p} \times E_{2p}^{*} \tag{1.16}$$

then we can get

$$\frac{dI_{2p}}{dz} \propto I^2 \tag{1.17}$$

The resulting 2PEF intensity is proportional to the square power of the excitation light (so is SHG).

The concept of 2PEF was first proposed by Maria Göppert-Mayer in 1931 [23], almost thirty years before the invention of lasers. The phenomenon was first observed by Kaiser and Garrett while illuminating CaF_2 with red light and generating blue fluorescence in 1961 [24]. The realization of 2PEF microscopy was demonstrated by Denk in 1990 [25].

1.2 Ultrafast source to drive MPM

The performance of MPM highly depends on the ultrafast driving source, which is quantified by the four parameters: excitation wavelength λ, pulse energy E_p, pulse duration τ, and repetition rate f. The selection of excitation wavelength is of particular importance especially for MPEF. Fluorophores are selective to the excitation wavelength and the fluorescence emission becomes more efficient as the fluorophore is illuminated at its peak absorption band. These bands differ from each other for different fluorophores. For common fluorophores emitting visible light (400-700 nm), the corresponding 2PEF excitation wavelength varies from 700 nm to 1200 nm. For 3PEF, longer excitation wavelength between 1000 nm and 1700 nm is required. As a result, driving sources that can be wavelength tuned within near-infrared (NIR) region are highly desired for MPEF. Although the excitation of HG exhibits no such wavelength selectivity, it is still recommended to employ longer wavelength (i.e., >800 nm for SHG, and >1200 nm for THG) because the resulting HG falls within the range of visible light, and therefore suffers less optical attenuation and can be efficiently detected.

The optical attenuation in biological tissues is mainly due to light scattering and absorption. In general, longer-wavelength beams scatter less in comparison with the shorter-wavelength one. The optical absorption spectra can differ from tissue to tissue due to the existence of different endogenous chromophores, such as lipids (fat), protein, blood (oxy- and deoxyhemoglobin), and melanin. However,

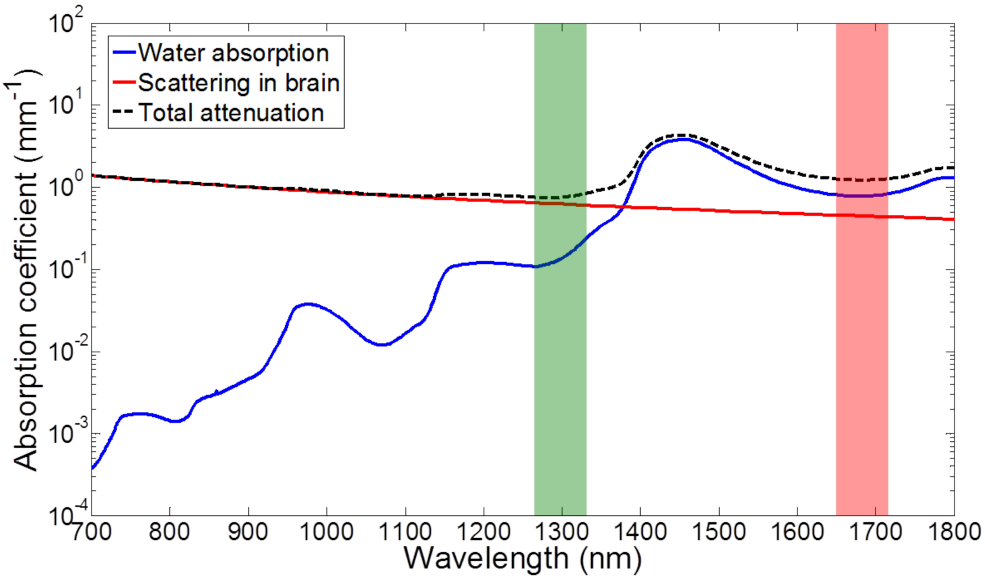

Figure 1.3: Optical attenuation in a brain tissue and possible excitation bands for 3PEF imaging.

the main absorption is due to water [135], which usually constitutes 60-80% of biological samples.

Considering both light scattering and water absorption, the total effective attenuation curve features several transmission windows within NIR range [26, 27]. We plot in Fig. 1.3 the wavelength-dependent optical attenuation in the brain tissue. Deep-tissue imaging is allowed by conducting MPM within these transmission windows [28, 29, 30]. For example, 3PEF functional imaging of GCaMP6s-labeled neurons can reach ~1-mm depth in mouse brain excited by 1300-nm femtosecond pulses within the window in the range of 1100-1350 nm (light green band in Fig. 1.3) [30]. 3PEF imaging of Texas-Red-labeled vasculature and red-fluorescent-protein (RFP)-tagged neurons in mouse brain can also reach similar depth while using 1675-nm excitation within the window between 1600 nm and 1870 nm (light red band in Fig. 1.3) [28].

For the process of n-photon excitation fluorescence, the photon flux $\left\langle F^{(n)}(t)\right\rangle$ of the emitted fluorescence can be described as [31]

$$\left\langle F^{(n)}(t)\right\rangle \propto \frac{1}{n}\frac{(NA)^{2n-4}\left\langle P(t)\right\rangle^{n}}{(f\tau)^{n-1}\lambda^{2n-3}} \tag{1.18}$$

where NA is the numerical aperture of the objective, and $\langle P(t)\rangle$ the average power of the illumination. With the relation $\langle P(t)\rangle = fE_p$, Eq. 1.18 can also be written as

$$\left\langle F^{(n)}(t)\right\rangle \propto \frac{1}{n}\frac{(NA)^{2n-4}f{E_p}^{n}}{(\tau)^{n-1}\lambda^{2n-3}} \tag{1.19}$$

Apparently, using objectives with higher NA improves the optical resolution and increases the emitted n-photon excitation fluorescence when $n>2$ (e.g., 3PEF). Once the excitation wavelength and the objective are decided, Eq. 1.18 becomes

$$\left\langle F^{(n)}(t)\right\rangle \propto \frac{1}{n}\frac{\langle P(t)\rangle^{n}}{(f\tau)^{n-1}} \tag{1.20}$$

For most of the modalities, the pulse energy required at the objective focus is at nJ level to achieve fine imaging contrast, and the pulse duration after the objective is ∼100 fs. The applied average power might vary from several mW to tens of mW depending on the laser repetition rate. To increase the signal photon flux, one usually uses higher-power illumination with shorter pulse duration. However, higher illumination power increases the risk of photodamage or photobleaching in the biological sample. The cross-section of three-photon absorption (3PA) of fluorophores is much smaller than that of two-photon absorption (2PA) such that the pulse energy required to induce 3PEF is higher than 2PEF. For deep-tissue 3PEF imaging, tens of nJ pulse energy is necessary. To avoid sample damage while increasing the pulse energy, ultrafast lasers operating at low repetition rate (∼1 MHz) are desired [28, 30].

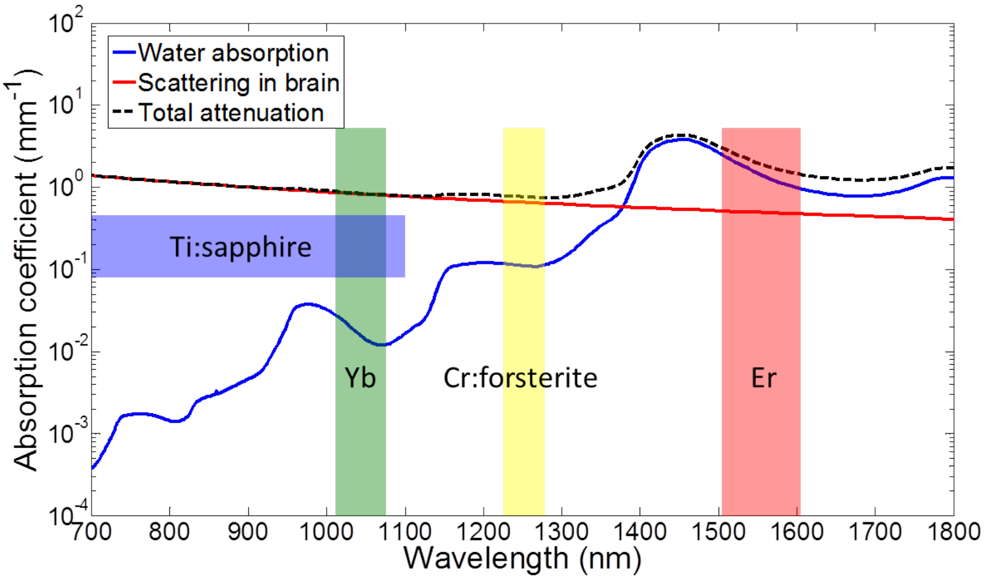

Figure 1.4: Optical attenuation and wavelength coverage of common ultrafast lasers.

Many ultrafast lasers are developed and applied to nonlinear optics. These sources normally consist of a mode-locked laser producing femtosecond pulses at different wavelength depending on the gain media. Normally, their center wavelengths are fixed and with limited optical bandwidth. For better comparison, we mark their wavelength coverage with the optical attenuation curve in Fig. 1.4. We briefly introduce their basic features in the following paragraph.

Ti:sapphire laser. First demonstrated in 1982 [32], nowadays Ti:sapphire lasers have become one of the most important ultrafast driving sources for MPM. The center wavelength is at ∼800 nm with the highest efficiency. The outstanding wavelength tunability over a wide range of 700-1100 nm covers the 2PA band of most of the important fluorophores and fluorescent proteins [33, 34, 35]. Besides 2PEF imaging, Ti:sapphire lasers are suitable to drive SHG modality.

Cr:forsterite laser. The center wavelength is around 1250 nm [36], which can induce fluorophores emitting red light. Despite the lower gain, poorer thermal property, and narrower optical bandwidth compared with Ti:Sapphire lasers [37], the direct emission within the transmission window of 1100-1350 nm makes Cr:forsterite lasers an ideal source to drive HGM [21, 38, 39]. Under this excitation, the resulting SHG and THG are both visible light, which suffer from less optical attenuation in the biological tissue.

Yb:fiber laser. The center wavelength of Yb-doped fiber lasers (YDFLs) is typically in the range of 1020-1060 nm, which is within the wavelength coverage of Ti:sapphire lasers. They are normally pumped by 975-nm laser diodes, which allows a high optical-to-optical conversion efficiency. This feature is in favor of the development of high-power sources. Ultrafast YDFLs are able to drive SHG and 2PEF imaging of limited fluorophores emitting yellow or orange light.

Er:fiber laser. Er-doped fiber lasers (EDFLs) can be pumped by 1480-nm or 975-nm diodes, and generate pulses of center wavelength between 1530 nm and 1610 nm [40]. The lack of high-power 1480-nm diodes makes the development of high-power EDFLs relying on 975-nm pump diodes, which results in a low optical-to-optical conversion efficiency. Ultrafast EDFLs can drive THG modality [41, 42], but they are not commonly adopted due to the higher water absorption at this wavelength range. On the other hand, they are widely used in optical communications because the wavelength range 1530-1565 nm (C-band) exhibits the lowest transmission loss in optical fibers made of fused silica.

In general, the conventional solution to ultrafast driving sources for MPM still relies on solid-state Ti:sapphire lasers due to the excellent wavelength coverage. The gaps in Fig. 1.4 can be solved by integrating the source laser with additional nonlinear optical devices to extend the wavelength coverage. An exemplary combination is a mode-locked laser plus a synchronously pumped optical parametric oscillator (OPO) or an optical parametric amplifier (OPA). Pumped by 800-nm femtosecond pulses, the resulting signal and idler beams are tunable in the range of 1-2 μm. However, the configuration of such a solid-state laser system usually contains much free space; the cavity requires accurate beam alignment and is sensitive to environmental fluctuations. In some cases, the beam quality is compromised. For a high-power source, water-cooling is inevitable to cope with the heat dissipation. These issues limit the application of MPM to specialized laboratories and thus spur the development of fiber-based driving sources.

Compared with solid-state lasers, the most distinct feature of fiber lasers is to employ optical fibers for light transmission, thus makes them robust and insensitive to environmental fluctuations. Optical fibers are flexible and can be coiled to reduce the laser footprint. When doped with different rare earth elements, optical fibers can work as gain media. They also exhibit outstanding heat dissipation ability compared with bulk materials due to their geometric structure has a high surface-to-volume ratio. The scheme of master oscillator power amplifier (MOPA) allows further power scaling. The fiber output has a nearly Gaussian spatial profile since only the fundamental mode experiences the lowest loss during the transmission. In addition, optical fibers and their related components are cost-effective compared with bulk optics. These advantages make fiber lasers a potential candidate to be the ideal source for driving MPM in clinical applications.

1.3 Fiber-optic methods for wavelength conversion

In spite of the advantages mentioned above, fiber lasers can only emit at a few wavelengths with narrow optical bandwidth. Common wavelength conversion devices such as OPO and OPA rely on second-order nonlinearity in nonlinear crystals; in contrast, due to the centrosymmetric structure, optical fibers host third-order nonlinearities for wavelength conversion. Several fiber-optic nonlinear mechanisms—such as four-wave mixing (FWM) [43, 44], dispersive wave (DW) generation [or so-called Cherenkov radiation (CR)] [45, 46, 47, 48, 49, 50, 51, 52], and soliton self-frequency shift (SSFS) [45, 53, 46, 54, 55, 28, 29, 56, 57, 58, 59, 60, 61, 51, 62]—were demonstrated for producing wavelength tunable pulses. They can significantly expand the wavelength coverage of an input narrowband spectrum. We summarize the representative results in Table 1.1, including the wavelength tuning range λ, the resulting pulse energy E_p, pulse duration τ_p, and the repetition rate f_{rep} of the fiber laser pump source.

FWM method normally results in sub-picosecond or picosecond pulses. For example, a fiber OPO enabled by FWM pumped by a μJ-level fiber laser system at 1040 nm produces 560-fs pulses after post compression with up to 27-nJ pulse energy [43]. DW can generate pulses below 100 fs. However, the wavelength tunability is limited to ~100 nm due to the phase matching requirement between the DW and the soliton that emits it. The resulting DW pulses are normally positively chirped and require post compression for later applications. SSFS can continuously red-shift the center wavelength of a femtosecond pulse propagating inside an optical fiber with negative group-velocity-dispersion (GVD). Although the amount of wavelength shift is tunable by varying the input pulse energy, SSFS can only lead to tunable pulses with their center wavelength longer than the pump wavelength. This implies that use of EDFLs as the pump source can only generate SSFS beyond 1550 nm. Wavelength coverage at shorter wavelength can be achieved via frequency doubling of SSFS pulses [63, 64, 65, 66].

SSFS-enabled wavelength tunable pulses are optical fundamental solitons. Its pulse energy needs to satisfy the well-known soliton area theorem [67]; which is

$$E_p = \frac{\lambda A_{eff}\,|\beta_2|}{\pi n_2 T_0} \tag{1.21}$$

where λ is the pulse center wavelength, A_{eff} the effective mode-field area (MFA), β_2 the GVD at the wavelength of λ, and n_2 the nonlinear-index coefficient of optical fibers. T_0 is connected to the full-width-at-half-maximum (FWHM) pulse width by $T_0 \sim T_{FWHM}/1.763$. Among all the parameters, A_{eff} is the most flexible one and can vary in a large range. For conventional single-mode fibers (SMFs), A_{eff} is typically less than 100 μm^2, which limits the soliton energy to below 1 nJ. Apparently, use of large-mode-area (LMA) fibers can lead to higher soliton energy. For example, SSFS in a photonic crystal rod with a MFA of 2300 μm^2 can generate 67-nJ pulses at 1675 nm [28, 29].

SFSS works successfully for generating high soliton energy in LMA fibers pumped by EDFLs (with a typical center wavelength around 1550 nm), since the requirements of large MFA and negative GVD are simultaneously achievable. However, these LMA fibers exhibit positive GVD for wavelength <1300 nm, which prevents the use of YDFLs (with a typical center wavelength around 1030 nm) as the pump source. By utilizing higher-order modes ($\mathrm{LP}_{0,\mathrm{m}}$), which exhibit negative GVD between 1 μm and 1.3 μm, energetic solitons can be generated in LMA higher-order-mode (HOM) fibers pumped by YDFLs [68, 69, 70, 71]. Although soliton with MW level peak power can be achieved at 1300 nm, the system complexity is also increased, since an additional spatial light modulator to generate HOMs is required. For succeeding applications, an axicon is used to convert the beam to Gaussian-like one with better spatial coherence.

Table 1.1: Nonlinear fiber-optic approaches for wavelength conversion.

	λ	E_p	τ_p	f_{rep}	Pump laser	Ref.
	nm	nJ	fs	MHz		
FWM	1200-1300	max 27	min 560	0.785	Yb	[43]
	1040-1305	max 8	n.a.	1	Yb	[44]
DW	1130-1300	<0.23	<25	67	Er	[45]
	600-700	<0.03	n.a.	41.3	Yb	[46]
	750-950	<0.13	14	3000	Yb	[47]
	370-850	max 2.3	25	50	Er	[48]
	600-800	>4	min 404	54.77	Yb	[49, 51]
	1200-1300	max 1.05	125	52.4	Er	[50]
	1300	0.076	29	42.4	Er	[52]
SSFS	up to 1950	<0.23	40*	67	Er	[45]
	1030-1330	0.1-0.5	<100	60	Yb	[53]
	1050-1690	max 0.24	100-150	41.3	Yb	[46]
	1580-2130	max 45	70	1	Er	[54]
	1160-1260	max 6.4	82	50	Yb	[55]
	1675	67	65	1	Er	[28, 29]
	1100-1700	n.a.	n.a.	54.77	Yb	[56, 51]
	1250	0.6	26	61	Yb	[57]
	1150-1350	max 0.3	136	3000	Yb	[58]
	1700	0.55	137	110	Er	[59]
	1200-1285	max 3	n.a.	39.6	Yb	[60]
	1650	21	86	100	Er	[61]
	1600-1700	9	75	50	Er	[62]
SSFS SHG	850-1100	0.08	n.a.	50	Er	[63]
	775-950	7.2-14	88-245	1	Er	[64]
	1150	6.5	86	11.25	Er	[65]
	950-1260	max 21	77-180	0.66	Er	[66]
SSFS HOMF	1064-1200	0.8	49	80	Yb	[68]
	1085	6.3	216	n.a.	Yb	[69]
	1030-1317	max 30	53.6	0.12	Yb	[70]
	1317	80	74	0.12	Yb	[71]
SPM	825-1210	1.1-3.3	70-120	55	Yb	[72]
	1030-1215	max 22	50-90	55	Yb	[73]
	920-1030	4.9-10.1	80-117	37	Yb	[74]

Among many nonlinear fiber-optic phenomena, self-phase modulation (SPM) can also broaden an optical spectrum to generate new wavelengths [75]. In 1998, Mamyshev proposed to use SPM-induced spectral broadening followed by offset spectral filtering for optical data regeneration [76]. The resulting optical pulse reshaping can be used in optical communications to suppress the noise in "zeros" and the amplitude fluctuations in "ones" [77, 78]. In these applications, long (more than tens of meters) optical fibers are required because the input pulses are several picosecond in duration with ∼1-W level peak power. In recent years, the idea of Mamyshev regenerator has been revived in the field of femtosecond pulse generation. For example, it allows the generation of femtosecond pulses using picosecond Q-switched lasers [79] or gain-switched lasers [80]; it is also used to enhance the temporal contrast of mJ femtosecond pulses [81]. Incorporation of Mamyshev regenerator inside a laser cavity has resulted in a new type of mode-locked lasers [82, 83]. In all above applications, SPM-induced spectral broadening increases the input spectral bandwidth by ∼50 nm at most, such that the regenerated pulse after optical filtering has a center wavelength close (<30 nm) to the initial pulse prior to the spectral broadening. This ensures that the regenerated pulse can be further amplified by the same gain medium that is used to amplify the initial pulse.

Recently the idea underlying Mamyshev regenerator was extended and applied to implementing wavelength widely tunable (∼400 nm) femtosecond sources [72, 73]. The essence of the idea is to employ SPM-dominated nonlinearity to dramatically broaden an input narrowband optical spectrum to a spectral width of hundreds of nm. The resulting broadened spectrum features well-isolated spectral lobes with a considerable portion of power contained by the leftmost and the rightmost lobes. Using optical filters to select the leftmost and the rightmost spectral lobes produces nearly transform-limited femtosecond pulses with the center wavelength widely tunable. We dub this methodology as SPM-enabled spectral selection (SESS).

This new application is clearly distinct from the conventional Mamyshev regenerator in that the filtered pulses may have the center wavelength far from the initial pulses' center wavelength and beyond the gain bandwidth, leading to a wide tuning range of hundreds of nm. For example, based on an ultrafast YDFL centered at 1030 nm, SESS allows us to generate ∼100-fs nearly transform-limited pulses (without external compression), tunable from 825 nm to 1210 nm with >1-nJ pulse energy [72]. SESS exhibits superior energy scalability; the resulting pulse energy can be scaled up by using shorter fibers with larger MFA. While SESS is implemented in 2-cm LMA fiber pumped by an ultrafast YDFL, we can achieve energetic pulses with up to >20-nJ pulse energy tunable in the range of 1030-1215 nm [73]. Such a powerful source enabled us to drive a video-rate laser scanning microscope to study human skin tissue based on HGM [73]. Unlike SSFS that always red-shifts an input spectrum, SPM-enabled spectral broadening can generate both blue-shifted and red-shifted spectral lobes. For example, employing SESS in a tapered PCF for dispersion management pumped by an ultrafast YDFL leads to femtosecond pulses at 920 nm with 10-nJ pulse energy [74]. This wavelength corresponds to the 2PA peak of one of the most important bio-markers—green fluorescent protein (GFP).

Indeed MPM can be driven by fiber-based ultrafast sources. Inspired by the success of SESS employed by YDFLs, ultrafast EDFLs are also potential for such a application. It is noteworthy that GFP and RFP can be excited by 1.3-μm and 1.7-μm femtosecond pulses through 3PA respectively. Ultrafast sources tunable in this wavelength range are crucial for 3PEF microscopy [84], which offers increased penetration depth for deep-tissue imaging [28, 29, 30]. Though compared with YDFLs, EDFLs exhibit lower quantum efficiency, the uniqueness of the direct emission at 1.55 μm right between two transmission windows (i.e., 1.3 μm and 1.7 μm) serves as a strong motivation to develop such SESS sources based on EDFLs. Another attractive thing is the versatile options of optical fibers for implementing SESS within this wavelength range. By engineering the waveguide dispersion, optical fibers are allowed to exhibit different GVD at 1.55 μm. For example, there exist dispersion-compensating fibers (DCFs), dispersion-shifted fibers (DSFs), and highly nonlinear fibers (HNLFs) besides standard SMFs. They are widely applied in optical communications and commercially available.

1.4 Structure of this thesis

In this thesis, we develop fiber-based ultrafast sources for MPM. We implement SESS in different optical fibers based on a home-built EDFL to generate energetic femtosecond pulses beyond the wavelength coverage of conventional Ti:sapphire lasers. The resulting SESS source are able to drive multimodal MPM. The thesis is composed of 6 chapters. The first part (Chapter 2 and Chapter 3) describes the development of an EDFL system that serves as the pump source and SESS in different optical fibers for later applications. The second part (Chapter 4 and Chapter 5) presents the MPM bio-imaging results enabled by such a powerful SESS source.

In Chapter 2 we first numerically study the SPM-dominated spectral broadening between 1.3 μm and 1.7 μm in optical fibers featuring different GVD and evaluate their potential for SESS. We then describe the construction of an EDFL that operates at 31-MHz repetition rate and generates 290-fs pulses centered at 1.55 μm with 160-nJ pulse energy (corresponding to 5-W average power).

Besides the excitation wavelength, the available pulse energy and average power that can be provided by a SESS source are also important for MPM. In Chapter 3 we demonstrate two energy-scaling approaches for SESS, i.e., shortening the fiber length and using fibers with larger MFA. Typically, SESS based on our EDFL pump source generates ~100-fs pulses continuously tunable between 1.3 μm and 1.7 μm with ~10-nJ pulse energy, corresponding to 100-kW level peak power. We further show that MW-level peak power is achievable by optimizing both the pumping laser source and the SESS process.

We dedicate Chapter 4 to our first MPM application driven by an EDFL-based SESS source. The developed SESS source is tuned to the transmission window of 1.15-1.35 μm and integrated with a scanning microscope. We carry out optical virtual biopsy enabled by HGM in human skin *ex vivo* and study the effect of different excitation wavelengths on the HGM performance.

In Chapter 5, we incorporate frequency doubling into our SESS source and generate femtosecond pulses at the Ti:sapphire laser wavelength. As a result, our EDFL-based source constitutes a two-color ultrafast source and allows us to perform 3-channel multimodal imaging. We apply this powerful MPM imaging platform to label-free human skin imaging (SHG, THG, and 2PEF) and protein crystal detection (SHG, THG, and 3PEF).

Finally we conclude our work with an outlook in Chapter 6.

Chapter 2

SESS based on EDFLs

In this chapter, we demonstrate an EDFL-based femtosecond source tunable between 1.3 μm and 1.7 μm. Before we present the experimental results, we first present a theoretical study of nonlinear porpagation of ultrafast pulses inside an optical fiber under the situation that SPM dominates the spectral broadening. We then construct a high-power EDFL system and use it to implement SESS generating wavelength widely tunable femtosecond pulses

2.1 SPM-dominated spectral broadening

For an ultrashort pulse with a Gaussian shape and constant phase, the intensity at time t is given by

$$I(t) = I_0 \cdot \exp\left(-\frac{t^2}{\tau^2}\right) \tag{2.1}$$

where I_0 is the peak intensity, and τ is half of the pulse duration. If the pulse propagates in an optical fiber, the optical Kerr effect leads to a refractive index change with respect to its intensity.

$$n(I) = n_0 + n_2 \cdot I \tag{2.2}$$

where n_0 is the linear refractive index, and n_2 is the second-order nonlinear refractive index of the medium. As the pulse propagates, the intensity in the fiber rises and then falls following the pulse, which produces a time-varying refractive index

$$\frac{dn(I)}{dt} = n_2 \frac{dI}{dt} = n_2 \cdot I_0 \cdot \frac{-2t}{\tau^2} \cdot \exp\left(-\frac{t^2}{\tau^2}\right) \tag{2.3}$$

This refractive-index variation exerts a shift in the pulse phase

$$\phi(t) = \omega_0 t - kz = \omega_0 t - \frac{2\pi}{\lambda_0} \cdot n(I)L \tag{2.4}$$

where ω_0 is the carrier frequency, λ_0 the wavelength of the pulse in vacuum, and L the propagation distance (fiber length). The phase shift results in a frequency shift.

The instantaneous frequency ω_t is given by

$$\omega_t = \frac{d\phi(t)}{dt} = \omega_0 - \frac{2\pi L}{\lambda_0}\frac{dn(I)}{dt} \tag{2.5}$$

Plugging Eq. 2.3 in Eq. 2.5 leads to

$$\omega_t = \omega_0 + \frac{4\pi L n_2 I_0}{\lambda_0 \tau^2} \cdot t \cdot \exp\left(-\frac{t^2}{\tau^2}\right) \tag{2.6}$$

ω_t describes the frequency shift of each part of the pulse. The leading edge ($t < 0$) shifts to lower frequencies, whereas the trailing edge ($t > 0$) shifts to higher frequencies. The very peak of the pulse ($t = 0$) remains the same. For the central portion of the pulse (between $t = \mp\tau/2$), the frequency shift varies linearly with time resulting in

$$\omega_t = \omega_0 + \alpha \cdot t \tag{2.7}$$

where α is

$$\alpha = \left.\frac{d\omega}{dt}\right|_0 = \frac{4\pi L n_2 I_0}{\lambda_0 \tau^2} \tag{2.8}$$

It is clear that SPM broadens the pulse spectrum symmetrically and the pulse envelope in the time domain remains unchanged. However, in real optical fibers the effects of dispersion simultaneously affect the pulse. For example, in the region of positive GVD, low-frequency part of the pulse has a higher velocity than the high-frequency part; that is, the front of the pulse moves faster than the back, and the pulse is temporally broadened.

Nonlinear spectral broadening of ultrashort pulses in an optical fiber can be precisely modeled by the well-known generalized nonlinear Schrödinger equation (GNLSE) [67]

$$\frac{\partial A}{\partial z} + \left(\sum^{n=2} \beta_n \frac{i^{n-1}}{n!}\frac{\partial^n}{\partial T^n}\right) A = i\gamma\left(1 + \frac{i}{\omega_0}\frac{\partial}{\partial T}\right)\left(A(z,T)\int_{-\infty}^{+\infty} R(t')\left|A(z,T-t')\right|^2 dt'\right) \tag{2.9}$$

where $A(z,t)$ is the amplitude envelope of the pulse, β_n the n-th order fiber GVD. The nonlinear parameter γ is defined as $\gamma = \omega_0 n_2/(cA_{eff})$, where ω_0 is the pulse center frequency, n_2 the nonlinear-index coefficient of fused silica with a typical value of $2.4 \times 10^{-20}\ m^2W^{-1}$, c the speed of light in vacuum, and A_{eff} the effective MFA. A_{eff} is connected to the mode-field diameter (MFD) d by $A_{eff} = \pi(d/2)^2$. $R(t)$ describes both the instantaneous electronic and delayed molecular responses (i.e., stimulated Raman scattering) of fused silica, and is defined as

$$R(t) = (1 - f_R)\delta(t) + f_R({\tau_1}^2 + {\tau_2}^2)/(\tau_1{\tau_2}^2)\exp(-t/\tau_2)\sin(t/\tau_1) \tag{2.10}$$

where typical value of f_R, τ_1, and τ_2 are 0.18, 12.2 fs, and 32 fs, respectively. Taking into account dispersion, SPM, self-steepening (SS), and stimulated Raman scattering (SRS), Eq. 2.9 has been widely used to study the nonlinear propagation of ultrashort optical pulses inside an optical fiber. Such a nonlinear propagation can significantly broaden the pulse spectrum and, under certain conditions, lead to supercontinuum generation [85].

To gain physical insight, we first neglect the dispersion effect and investigate the role of each nonlinear effect—namely SPM, SS, and SRS. In Sec. 2.1.3, we include the dispersion term into the simulation and show its effect on the nonlinear spectral broadening.

2.1.1 Pure SPM effect

We first consider only SPM and neglect the effect of dispersion, SS, and SRS. Consequently Eq. 2.9 is simplified as

$$\frac{\partial A}{\partial z} = i\gamma|A|^2 A \tag{2.11}$$

Equation 2.11 has an analytical solution $A(z,t) = A(0,t)\exp(i\gamma|A|^2 z)$. Using this solution, we simulate a 300-fs hyperbolic secant-squared pulse (center wavelength at 1.55 μm with 40-nJ pulse energy) propagating inside an optical fiber with a MFD of 4 μm. Figure 2.1(a) shows that the optical spectrum broadens dramatically along the fiber length and is composed of well-isolated spectral lobes; the number of these spectral lobes is linearly proportional to the fiber length—a unique feature of SPM-dominated spectral broadening. For example, after propagating 4-cm distance the optical spectrum develops 13 spectral lobes with the leftmost one peaking at 1374 nm and the rightmost one at 1776 nm [Fig. 2.1(b)], which covers the spectral range between 1.3 μm and 1.9 μm —a wavelength range highly desired by MPM.

We then numerically filter both the leftmost and the rightmost spectral lobes, and plot them as the insets of Fig. 2.2(a) and 2.2(b), respectively. The blue curves in these two figures are the corresponding pulses due to spectral lobe filtering and the red curves are the transform-limited (TL) pulses calculated from the leftmost and the rightmost spectral lobes [i.e., the spectra shown as the black curves in the insets of Fig. 2.2(a) and 2.2(b)]. More specific, the filtered leftmost spectral lobe produces 79-fs, 10-nJ pulses and the rightmost spectral lobe produces 89-fs, 9.9-nJ pulses. The transform-limited pulses calculated from the filtered spectra are 76 fs and 88 fs in duration, respectively, showing that the filtered pulses are nearly transform-limited.

Another interesting feature of the SPM-broadened spectrum is that the leftmost and the rightmost spectral lobes are the strongest; these two spectral lobes have a total energy of ∼20 nJ (∼10 nJ for each), accounting for 50% conversion of the total energy. Note that other spectral lobes in Fig. 2.1(b) can also be filtered; however, these intermediate spectra possess much less pulse energies compared with the leftmost and the rightmost spectral lobes.

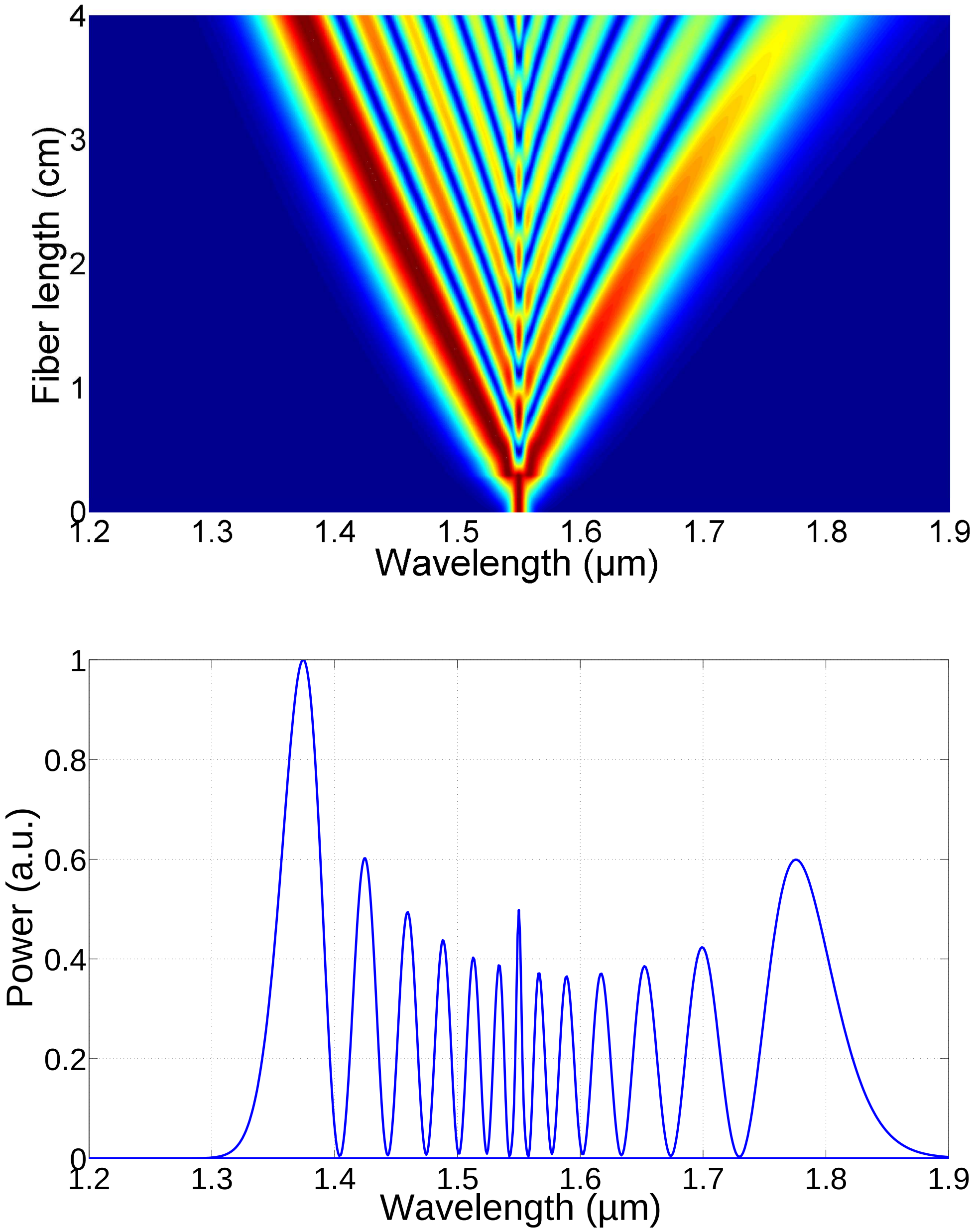

Figure 2.1: Spectral broadening enabled by pure SPM. (a) Spectral evolution along the propagation length. (b) Final output spectrum.

Simulation results in Fig. 2.1 and Fig. 2.2 suggest a novel method to implement a multi-color ultrafast source. The filtered two spectral lobes plus the original laser wavelength enable the laser system to produce ultrashort pulses at three different center wavelengths. More important, the center wavelength of these filtered spectral lobes can be continuously tuned by adjusting the energy coupled into the optical fiber with a fixed fiber length.

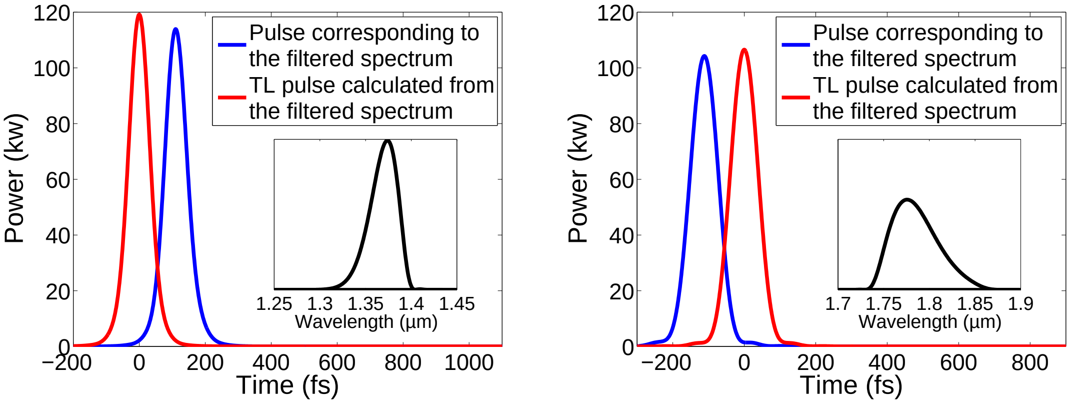

Figure 2.2: Filtered pulses of (a) the leftmost and (b) the rightmost spectral lobes.

2.1.2 Effect of SS and SRS

The results in Fig. 2.1 and Fig. 2.2, though informative and impressive, are unpractical since only SPM is considered. Other nonlinear effects such as SS and SRS take place as well. To investigate their role in the nonlinear spectral broadening, we redo the simulation by further including SS or both SS and SRS; the resulting spectra after 4-cm propagation are plotted in Fig. 2.3(a). The spectrum broadened due to SPM and SS [blue curve in Fig. 2.3(a)] is significantly blue shifted compared with the pure SPM-broadened spectrum [Fig. 2.1(b)]. When SRS is also included, the resulting spectrum [red curve in Fig. 2.3(a)] almost overlaps the blue curve. If we let the pulse propagate 2 cm more, the resulting spectrum [red curve in Fig. 2.3(b)] becomes slightly narrower due to the small red shift of those spectral lobes on the left side in comparison with the result considering only SPM and SS [blue curve in Fig. 2.3(b)].

Figure 2.4(a) shows the spectral evolution of a pulse propagating in 4-cm fiber considering SPM, SS, and SRS. The initial condition is same as in Sec. 2.1.1. We numerically filter the leftmost and the rightmost spectral lobes from the broadened spectrum at the fiber output, and plot the corresponding optical pulses in Fig. 2.4. The filtered spectral lobes are shown as insets in Fig. 2.4(b) and Fig. 2.4(c). The filtered pulse at the shorter wavelength centered at 1320 nm has a duration of 56 fs with 7.6-nJ pulse energy; the other filtered pulse with longer wavelength centers at 1722 nm with 107-fs duration and 11.7-nJ pulse energy. Both pulses are nearly transform-limited (off by <10 fs).

The simulation results in this section reveal the following effects exerted by SS and SRS on the nonlinear spectral broadening and energy conversion to the leftmost and the rightmost spectral lobes:

1. SS extends the broadened spectrum more towards the shorter wavelength [comparison between Fig. 2.1(b) and blue curve in Fig. 2.3(a)].
2. For pure SPM-broadened spectrum, the leftmost and the rightmost spectral

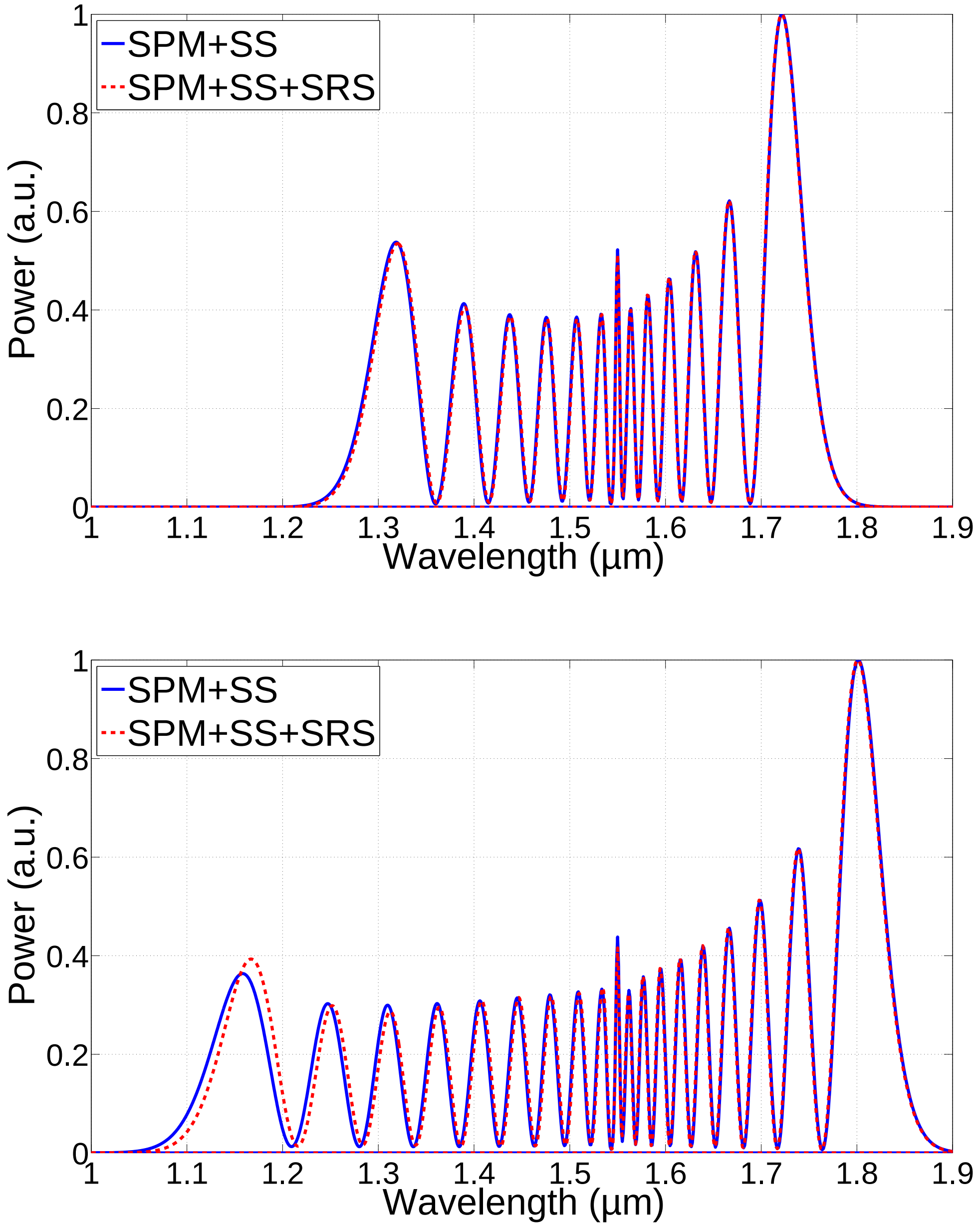

Figure 2.3: Spectral broadening considering SS and SRS in (a) 4-cm and (b) 6-cm optical fibers.

lobes share the same energy (Fig. 2.2). When SS and SRS are included, more energy is converted into the rightmost spectral lobe, though total conversion efficiency into these two spectral lobes is comparable for the two cases—∼50% for pure SPM-broadened spectrum and if SS and SRS are considered as well [Fig. 2.4(b) and Fig. 2.4(c)].

3. The effect of SRS is minimal compared with SS [Fig. 2.3(a) and Fig. 2.3(b)].

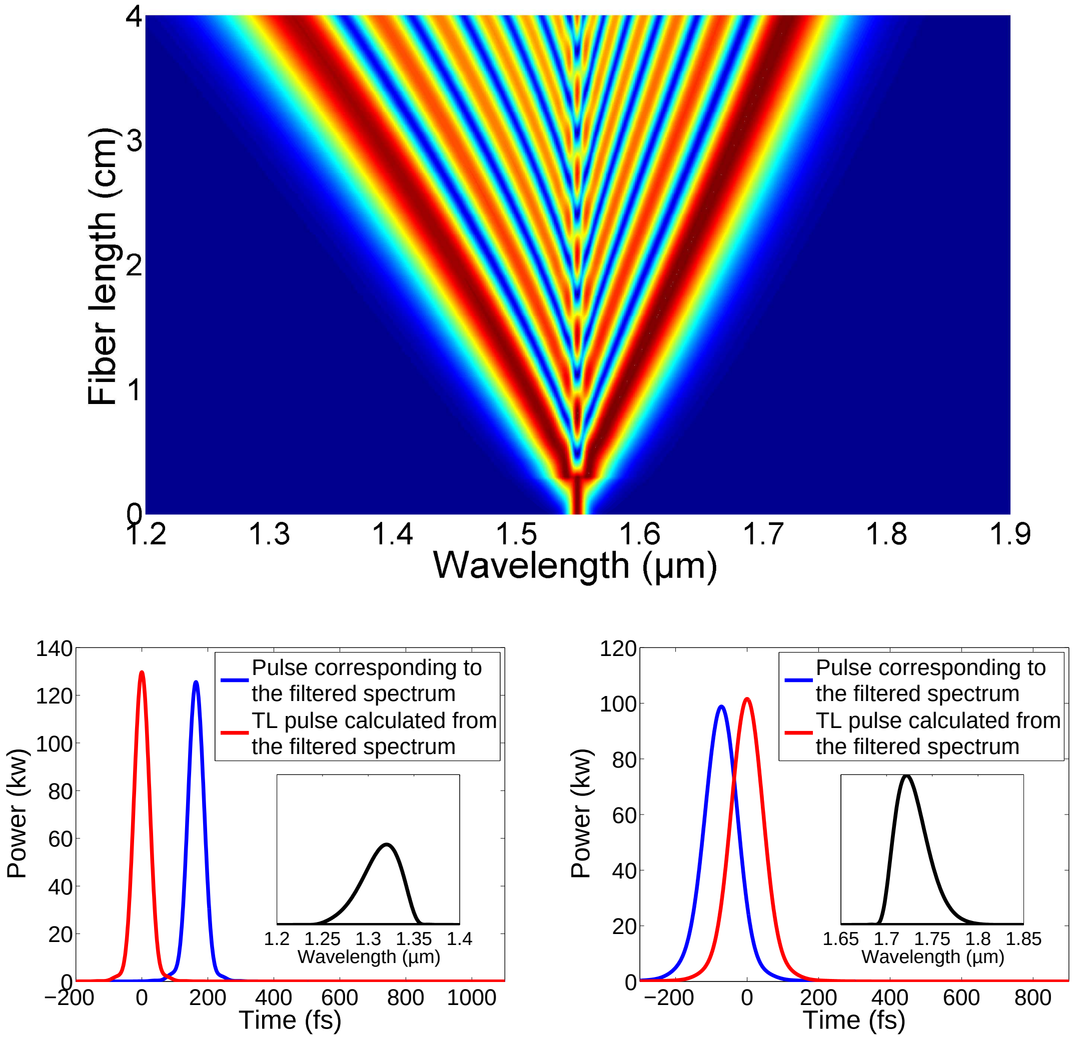

Figure 2.4: (a) Spectral broadening in 4-cm fiber considering SPM, SS, and SRS; and the filtered pulses from (b) the leftmost and (c) the rightmost spectral lobes at the fiber output.

2.1.3 Effect of dispersion

To illustrate the effect of dispersion, including GVD (denoted by β_2) and third-order dispersion (TOD) (denoted by β_3), we redo the simulation for three different dispersion combinations: (β_2 = 40 fs^2/mm, β_3 = 0), (β_2 = 40 fs^2/mm, β_3 = 200 fs^3/mm), and (β_2 = 40 fs^2/mm, β_3 = -200 fs^3/mm). We keep all other parameters unchanged and plot the broadened spectra in Fig. 2.5. The blue curve shows the broadened spectrum using the fiber with constant GVD of 40 fs^2/mm (β_3 = 0). Comparison of this curve and the blue curve in Fig. 2.3(a) indicates that positive GVD has two consequences:

1. The broadened spectrum becomes narrower.

2. The spectral-lobe structures tend to wash out manifesting as shallower spectral valleys.

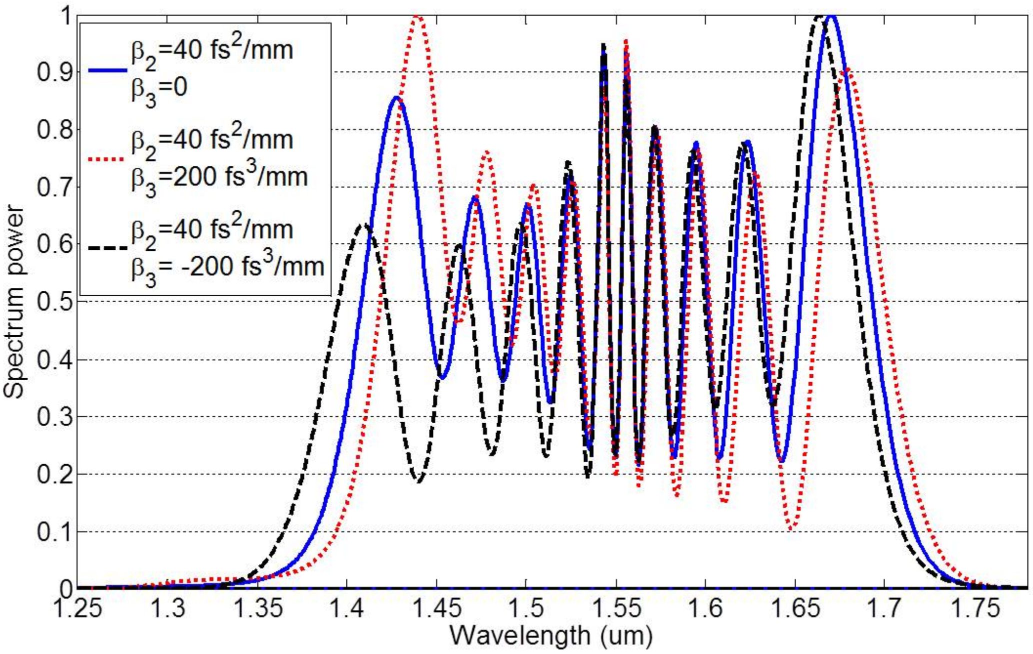

Figure 2.5: Simulation results of different dispersion combinations.

TOD leads to frequency-dependent GVD and plays an important role as well. For positive TOD (β_2 = 40 fs^2/mm, β_3 = 200 fs^3/mm), GVD decreases with an increased wavelength and the resulting optical spectrum is broadened more towards longer wavelength (red dotted curve in Fig. 2.5). Compared with the constant GVD case (blue curve in Fig. 2.5), positive TOD generates deeper (shallower) spectral valleys on the long (short) wavelength side. In contrast, negative TOD (β_2 = 40 fs^2/mm, β_3 = -200 fs^3/mm) causes the spectrum broadened more towards shorter wavelength, with the shallower (deeper) spectral valleys on the long (short) wavelength side [black dashed curve in Fig. 2.5]. The simulation results in Fig. 2.5 suggest that the spectral broadening and formation of clear spectral lobes benefit from a smaller positive GVD.

2.2 EDFL pump source

The development of high-power and high-pulse-energy ultrafast EDFLs mainly faces two challenges: the low quantum efficiency and the fiber nonlinearity. The low quantum efficiency originates from the huge wavelength difference between the pump and the signal emission. Though 976-nm diodes are commonly used as the pump for YDFLs and EDFLs, the wavelength difference between the pump and the emitted signal results in quite different slope efficiency for these two lasers. The typical slope efficiency (pump conversion efficiency) for Yb-doped fiber amplifiers (YDFAs) can easily reach 70% even under high-power amplification, while Er-doped fiber amplifiers (EDFAs) have ∼30% slope efficiency.

The issue that nonlinearity might distort the pulse while amplification can be solved by chirped-pulse amplification (CPA) [86]. Several works on developing high-power and high-pulse-energy ultrafast EDFLs are reported. The parameters are listed in Table 2.1, including the average output power P_{avg}, the repetition rate f_{rep}, the pulse energy E_p, the pulse duration τ_p, and the pulse peak power P_p. The pulse peak power P_p is defined as

$$P_p \approx 0.88\frac{E_p}{\tau_p} \tag{2.12}$$

assuming a hyperbolic-secant temporal shape for a soliton pulse. For a Gaussian-shaped pulse, the constant 0.88 is replaced by 0.94. P_p listed in Table 2.1 is calculated assuming a hyperbolic-secant pulse.

Most demonstrated ultrafast EDFLs work at tens-of-MHz repetition rate [87, 88, 89, 90, 91]. Most of them generate pulses with the duration limited to >450 fs, except the one in Ref. [91], which introduces SPM-induced spectral broadening to overcome the gain narrowing during the amplification. Ultrafast EDFLs operating at lower repetition rate of only hundreds of kHz to several MHz are able to generate pulses with ∼2-MW peak power [92, 93]. The reported pulse duration is in the range of 0.6-1 ps. Using LMA and high efficiency media (HEM) fibers, impressive experimental results are obtained in Ref. [94] in terms of pulse energy, peak power, and pulse duration. However, the extremely low repetition rate (<5 kHz) is not suitable to drive laser scanning microscopy (LSM).

Table 2.1: High-power and high-pulse-energy EDFLs based on CPA.

P_{avg} (W)	f_{rep} (MHz)	E_p (nJ)	τ_p (fs)	P_p (MW)	Ref.
8.65	50	173	835	0.182	[87]
8	35	229	850	0.237	[88]
10	165	61	450	0.119	[89]
3.4	75	45	765	0.052	[90]
3.5	43	80	175	0.409	[91]
0.45	0.3	1.5k	605	2.18	[92]
2	1	2k	880	2	[93]
1.07	0.5	2.14k	880	2.14	[93]
0.425	0.2	2.125k	950	1.968	[93]
0.208	0.1	2.08k	1050	1.743	[93]
4.4	0.0048	913k	485	1.657k	[94]

The parameters of the desired EDFL for implementing SESS should be similar to the YDFL system reported in Ref. [72, 73]. Repetition rate of tens of MHz is suitable for driving LSM. >100-nJ pulse energy allows the resulting SESS source that can be tuned between 1.3 μm and 1.7 μm with considerable pulse energy (10 nJ) later for MPM. The SESS pulse duration is ~1/3 of the input pulse. Thus, the pulse duration of this pump source is aimed to be 300 fs in hope of producing ~100-fs pulses by SESS.

Besides these desired parameters, we build the EDFL system following the principles below:

1. To reduce the detrimental effect of environmental fluctuations and maintain a small footprint, the system should contain as little free space for beam alignment as possible. Or namely, use as much fiber for configuration as possible. If free-space alignment is inevitable, then make it compact.
2. The system should employ polarization-maintaining (PM) devices to ensure a stable pulse generation.

The oscillator is mode-locked by a semiconductor saturable absorber mirror (SAM) (from Baptop). Fig. 2.6 shows the picture of the seed oscillator, which is compact due to the use of optical fibers and in-line fiber-optic components. This seed oscillator operates at 31-MHz repetition rate and generates ~100-pJ pulses centered at 1550 nm. The repetition rate is intentionally chosen to be ~30 MHz in order to enable video-rate (i.e., 30 frames/s) imaging in a laser scanning microscope, assuming that each image consists of 512 × 512 pixels with 4 pulses per pixel or 1024 × 1024 pixels with 1 pulse per pixel on average.

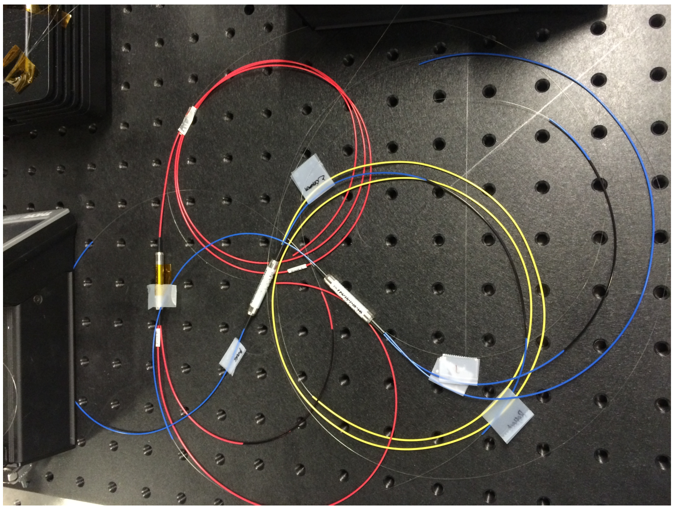

Figure 2.6: Picture of the seed oscillator.

Figure 2.7 depicts the total setup of the Er:fiber CPA system. A PM fiber stretcher exhibiting positive GVD at 1550 nm stretched the pulse duration from the oscillator output to ~15 ps, which were then amplified to 8-nJ pulse energy by two stages of EDFA. The main EDFA was constructed using a PM Er:Yb co-doped fiber pumped by two 976-nm laser diodes. The amplified 200-nJ pulses were dechirped by a transmission diffraction-grating pair with 966.2-lines/mm groove density. The grating pair was set in a double-pass configuration with 80% transmission efficiency. The oscillator, the fiber stretcher, and two stages of EDFA are constructed on a 600 mm × 600 mm breadboard; the main power amplifier and the grating compressor are mounted on another breadboard with the same size. The nearly all-fiber configuration enables the system compactness. The all-PM configuration assures a stable linearly polarized output spectrum with 23-dB polarization extinction ratio (PER).

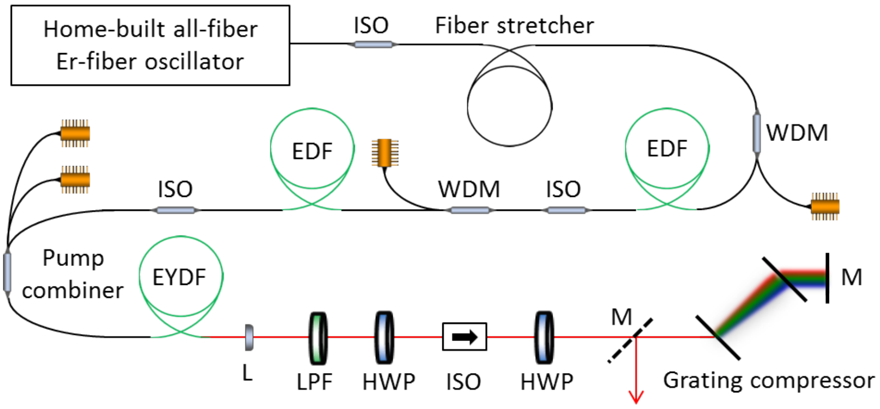

Figure 2.7: Schematic setup of the Er:fiber CPA system. ISO: isolator, WDM: wavelength-division multiplexing, EDF: erbium-doped fiber, EYDF: erbium ytterbium co-doped fiber, L: lens, LPF: long pass filter, HWP: half-wave plate, M: mirror.

To generate high-quality pulses, the total dispersion (especially the TOD) of the CPA system must be carefully managed. In Fig. 2.8 we plot the group-delay dispersion (GDD) contribution from the optical fiber and the gratings in the CPA system. The diffraction grating-pair as the pulse compressor provides negative GVD and TOD (blue curve in Fig. 2.8). Our fiber stretcher consists of PM dispersion-compensating fiber (denoted as PM-DCF) and conventional PM-SMF (denoted as PM1550). The PM-DCF provides positive GDD and negative TOD (black curve in Fig. 2.8), whereas PM1550 provides negative GVD and TOD (red curve in Fig. 2.8). An optimal length combination of these two kinds of fiber allows us for the dispersion management.

Figure 2.9 shows the measured autocorrelation trace (red curve) of the compressed pulse. The pulse duration is estimated to be 290 fs assuming a hyperbolic-secant pulse profile. Inset of Fig. 2.9 records the optical spectrum of the compressed pulse. Black dashed curve in Fig. 2.9 indicates the calculated autocorrelation trace of the transfom-limited pulse allowed by the optical spectrum. Apparently the compressed pulse is close to be transform-limited.

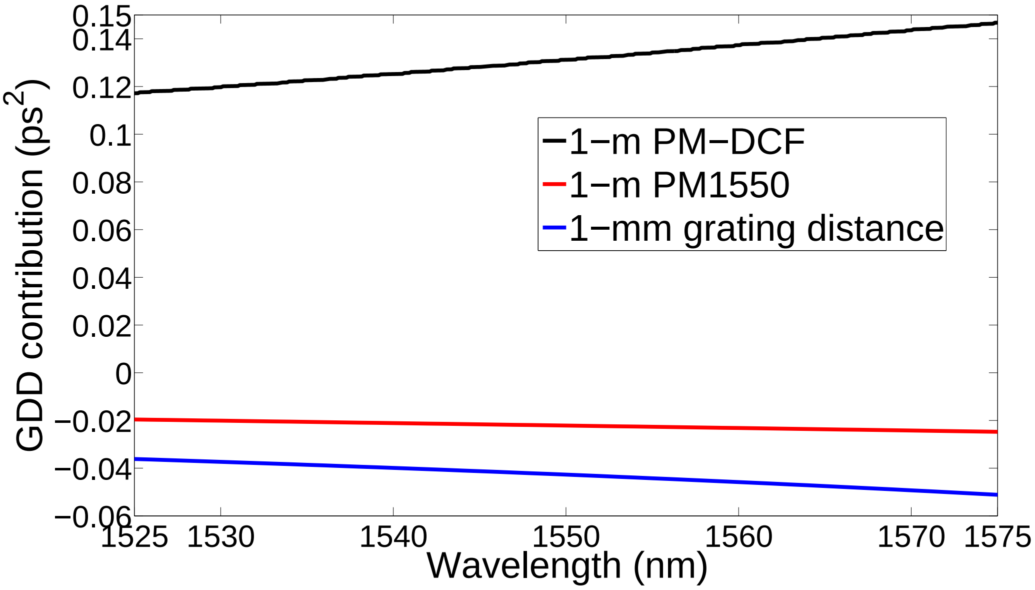

Figure 2.8: GDD contribution from optical fibers and gratings.

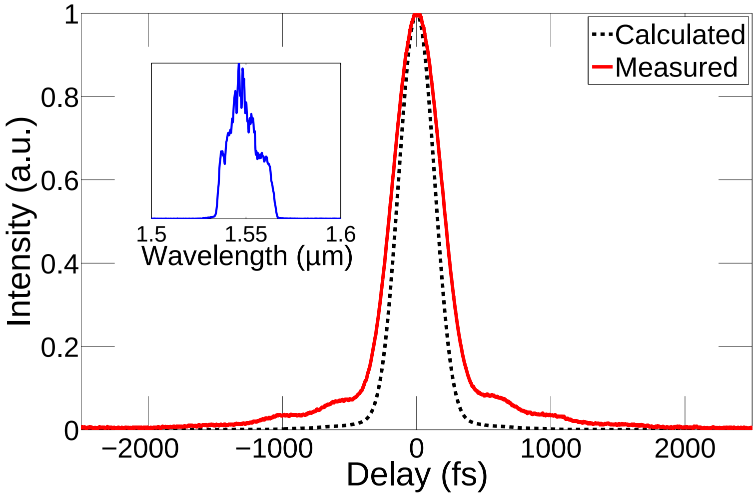

Figure 2.9: Measured (red) and calculated (black dashed) autocorrelation traces of the compressed pulse.

2.3 Spectral broadening in common optical fibers

In this section, we tested six commercially available optical fibers to evaluate their potential for implementing SESS. These optical fibers include standard SMFs, dispersion-shifted fibers (DSFs), highly nonlinear fibers (HNLFs), and dispersion-compensating fibers (DCFs). They exhibit different GVD and TOD at the 1.55-μm pump wavelength. Their optical parameters are listed in Table 2.2.

Table 2.2: Properties of common optical fibers.

Fiber Type	D ps/nm/km	β_2 fs^2/mm	β_3 fs^3/mm	MFD μm	γ W^{-1}km^{-1}
SMF	18	-23	+	10.4	1.6
DSF	8	-10	+	9.6	1.88
HNLF1	0.32	-0.408	+	4	10.8
HNLF2	2	-2.55	+	4.2	9.8
DCF3	-3	3.83	+	8	2.7
DCF38	-38.5	48.5	-	6	4.8

We first compare the spectral broadening in different fibers with the same 4-cm length. Figure 2.10 shows the schematic setup, which consists of an EDFL pump source and a fiber coupling module.

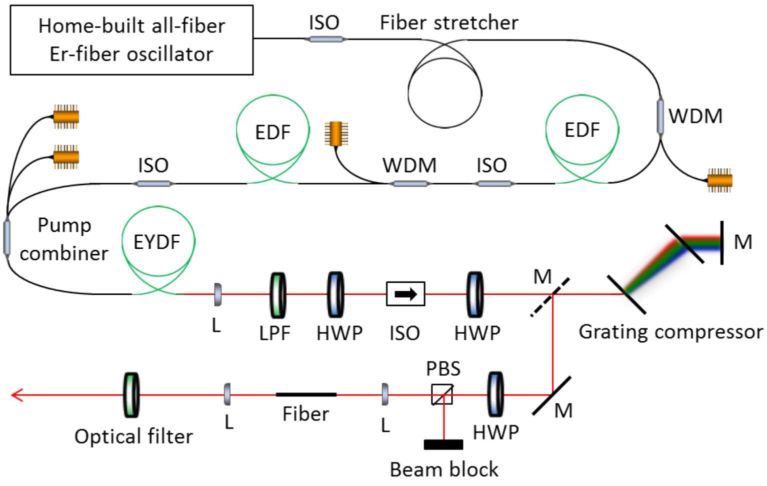

Figure 2.10: Schematic setup for SESS.

The EDFL pump source operates at 31-MHz repetition rate and generates 290-fs pulses centered at 1550 nm with 160-nJ pulse energy. The 1550-nm beam is coupled into an optical fiber for nonlinear spectral broadening followed by optical filters to select the leftmost or the rightmost spectral lobe. The fiber coupling module includes a fiber holder (HFV002, Thorlabs), a 3-axis stage (MAX313D/M, Thorlabs), and an aspheric lens. A half-wave plate (HWP) and a polarization beam splitter (PBS) are used to adjust the pulse energy coupled into the fiber. The fiber output is collimated by another aspheric lens.

2.3.1 Fibers with negative GVD

Figure 2.11 shows the spectral broadening in 4-cm standard SMF with coupled pulse energy varied from 30 nJ to 80 nJ. As the coupled pulse energy increases, the spectrum gradually broadens towards both the shorter and the longer wavelength. With 80-nJ coupled pulse energy, the leftmost spectral lobe peaks at 1.43 μm with a long tail extending to 1.3 μm [Fig. 2.12(a)]. The well-isolated spectral lobes disappear at the shorter wavelength for the coupled pulse energy at 85 nJ [Fig. 2.12(b)] and 90 nJ [Fig. 2.12(c)].

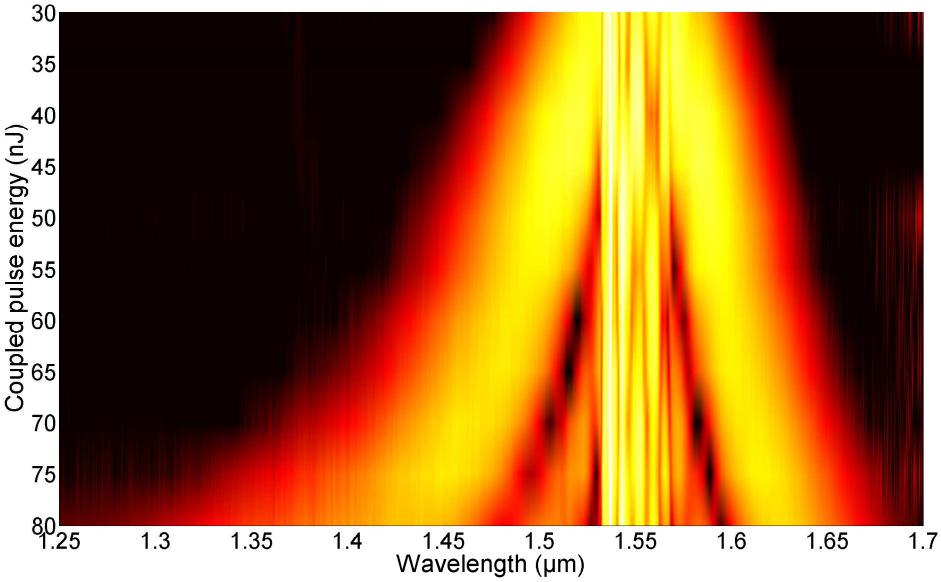

Figure 2.11: Spectral broadening in 4-cm standard SMF.

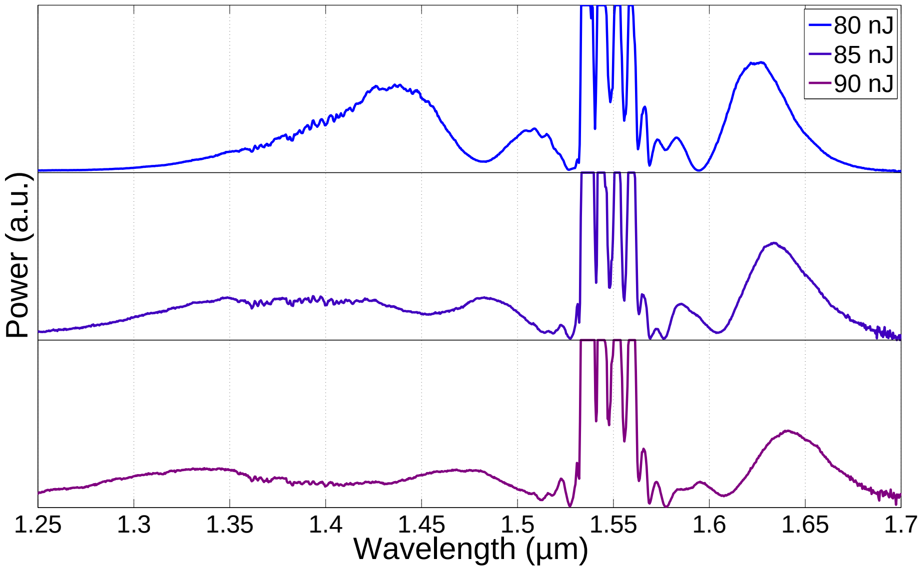

Figure 2.12: Washout of well-isolated spectral lobes in 4-cm standard SMF.

To show the effect of fiber length, we prepare another 10-cm standard SMF. The spectral broadening with respect to the coupled pulse energy varied from 10 nJ to 30 nJ is shown in Fig. 2.13. Apparently, the spectral broadening is dominated by SPM when the coupled pulse energy less than 18 nJ. Figure 2.14 depicts the spectral-lobes-washout as we change the coupled pulse energy from 17.7 nJ to 21.3 nJ. Comparison between Fig. 2.11 and Fig. 2.13 shows that the spectrum spans narrower before the spectral-lobes-washout for a longer optical fiber.

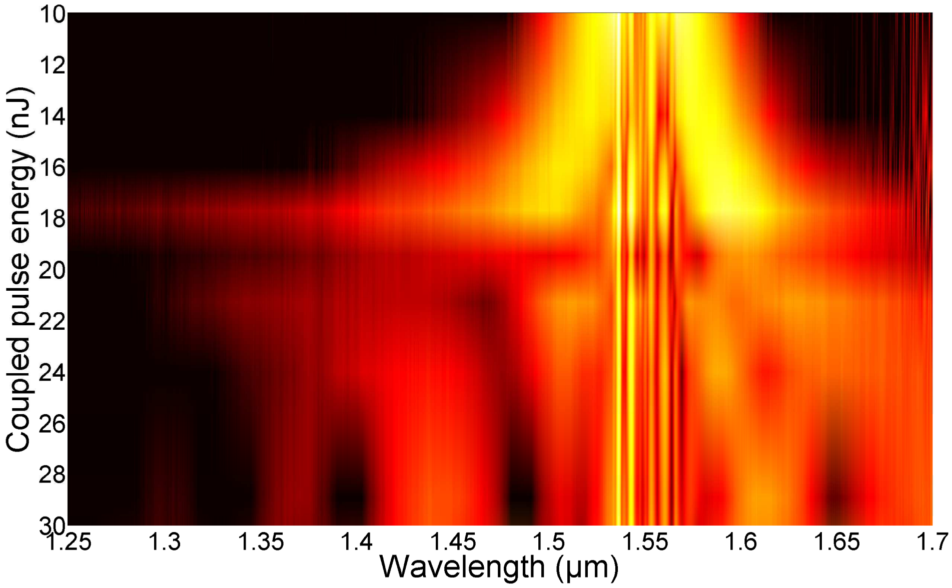

Figure 2.13: Spectral broadening in 10-cm standard SMF.

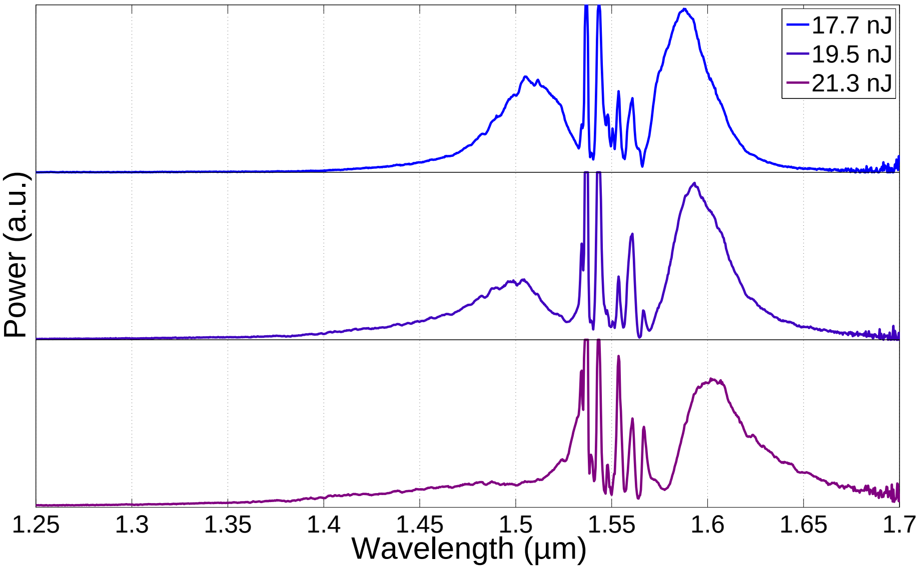

Figure 2.14: Washout of well-isolated spectral lobes in 10-cm standard SMF.

Indeed the interplay between negative GVD and SPM allows SSFS to generate wavelength red-shifted femtosecond pulses. We demonstrate this in Fig. 2.15 by using 75-cm standard SMF with coupled pulse energy varied from 2 nJ to 6 nJ. In contrast to SPM-dominated spectral broadening that extends the spectrum to both the shorter and the longer wavelength, SSFS generates red-shifted spectral lobes at the longer wavelength. Using a longpass filter (LPF) with 1.65-μm cut-on wavelength to select the isolated spectral lobe peaking at 1.7 μm, the resulting pulse energy is at 1-nJ level (~30 mW).

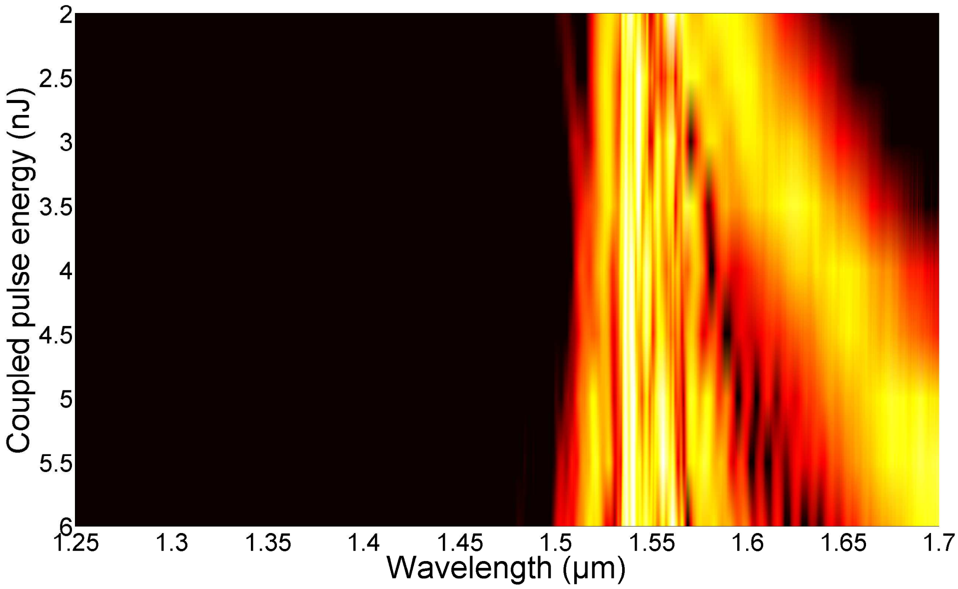

Figure 2.15: SSFS in 75-cm standard SMF.

Figure 2.16 shows the spectral broadening in 4-cm DSF with coupled pulse energy also varied from 30 nJ to 80 nJ. Although DSF has higher nonlinear parameter, the spectrum broadens less compared with in 4-cm standard SMF (Fig. 2.11), since dispersion plays an important role here. Ultrafast pulses experience higher-order soliton compression while propagating inside an optical fiber with negative GVD [67]. In comparison with standard SMF, DSF exhibits lower GVD at the pump wavelength (1.55 μm) leading to a less compressed pulse with lower peak power for SPM-dominated spectral broadening.

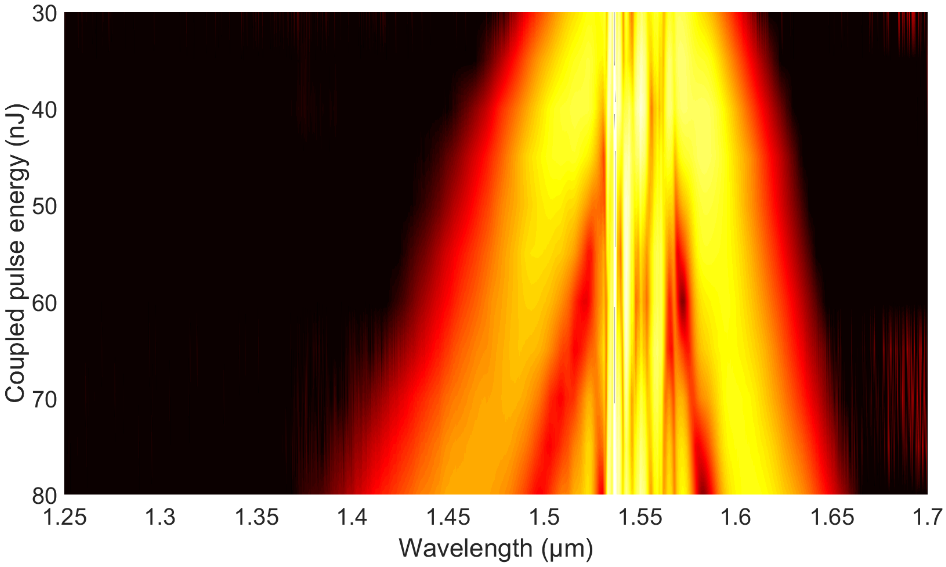

Figure 2.16: Spectral broadening in 4-cm DSF.

2.3.2 Fibers with nearly zero GVD

The two HNLFs exhibit nearly zero GVD and large nonlinear parameter (~10 $W^{-1}km^{-1}$) due to the smaller MFD (~4 μm) at 1.55 μm, which favors SPM-induced spectral broadening. Figure 2.17 shows the spectral broadening in 4-cm HNLF1 with coupled pulse energy varied from 10 nJ to 30 nJ. With 30-nJ coupled pulse energy, the leftmost and the rightmost spectral lobes of the broadened spectrum peak at 1.3 μm and 1.7 μm, respectively. Similar to HNLF1, the broadened spectrum spanning from 1.3 μm to 1.7 μm is also achievable in 4-cm HNLF2 with 24-nJ coupled pulse energy (Fig. 2.18). The less required pulse energy for the same spectral broadening can be explained by the difference of GVD. Pulse propagating in HNLF2 accumulates more negative GDD and experiences more higher-order soliton compression, leading to higher peak power for spectral broadening.

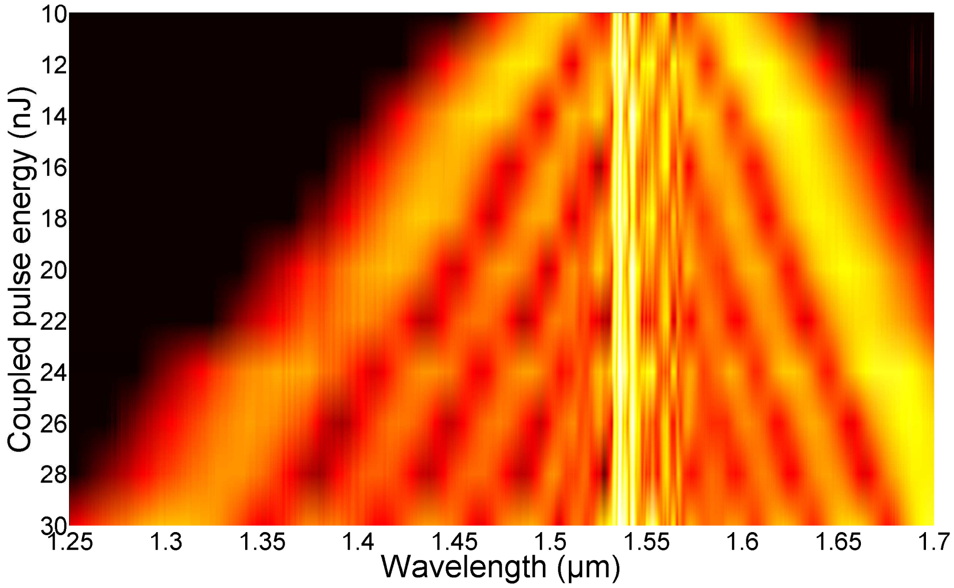

Figure 2.17: Spectral broadening in 4-cm HNLF1.

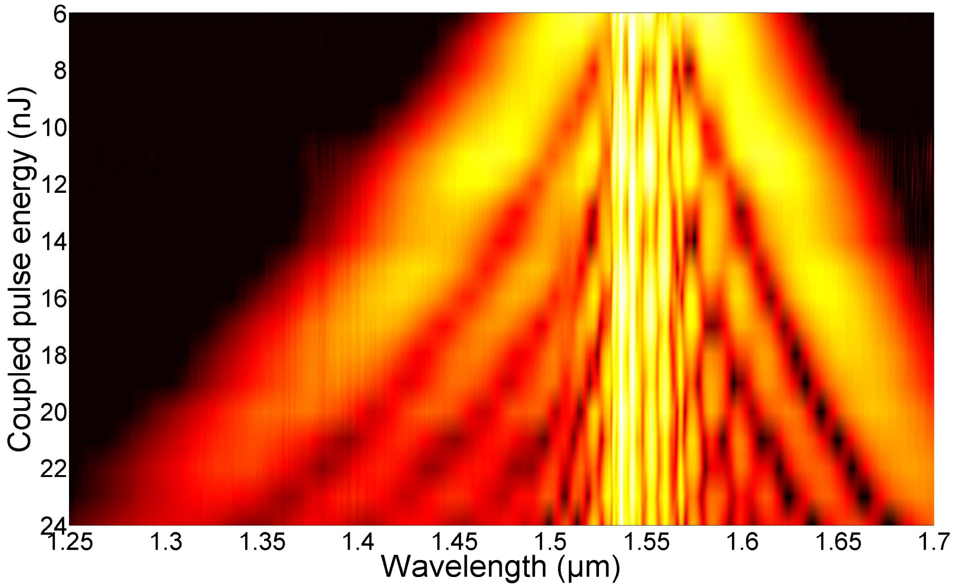

Figure 2.18: Spectral broadening in 4-cm HNLF2.

2.3.3 Fibers with positive GVD

The two DCFs exhibit different amount of positive GVD and opposite TOD sign at 1.55 μm. Figure 2.19 and Fig. 2.20 show the spectral broadening in 4-cm DCF3 and DCF38 with coupled pulse energy varied from 20 nJ to 80 nJ, respectively. The leftmost/rightmost spectral lobe from 4-cm DCF3 with 80-nJ coupled pulse energy peaks at 1.42/1.65 μm (Fig. 2.19), whereas the spectral lobe from 4-cm DCF38 peaks at 1.36/1.67 μm (Fig. 2.20). Compared with fibers with negative GVD, SPM mainly dominates the spectral broadening in fibers with positive GVD. Contrary to higher-order soliton compression, the input pulse is gradually stretched along the propagation length. The stretched pulse reduces its peak power, and thus mitigates the SPM-induced spectral broadening. Further increasing the coupled pulse energy can hardly broaden the spectrum. This effect can be observed in 4-cm DCF3 with >60-nJ coupled pulse energy (Fig. 2.19) and in 4-cm DCF38 with >65-nJ coupled pulse energy (Fig. 2.20).

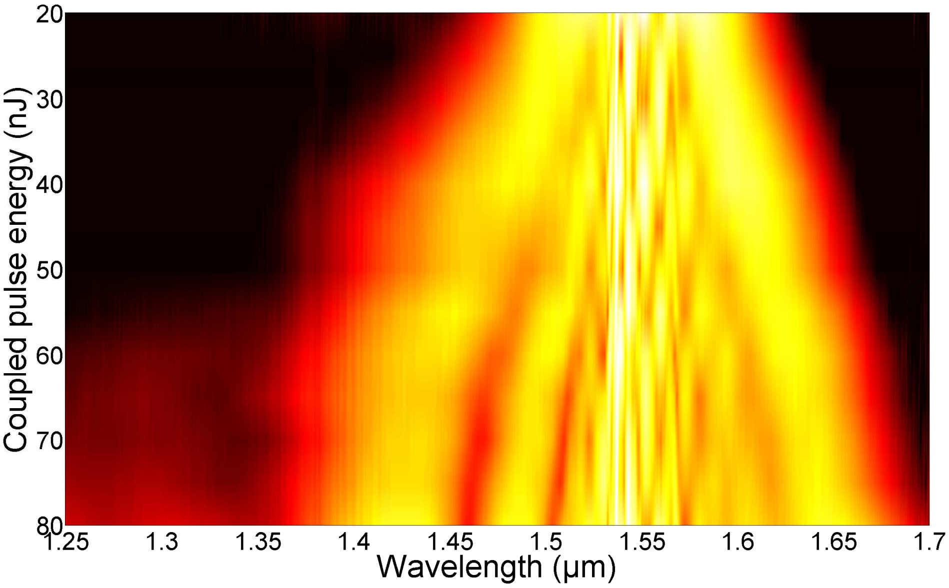

Figure 2.19: Spectral broadening in 4-cm DCF3.

Besides GVD, spectral broadening is also affected by TOD. To illustrate this effect, we plot the spectra from 4-cm DCF3 (red dashed curve) and 4-cm DCF38 (blue curve) in Fig. 2.21. To have a fair comparison, both of the rightmost spectral lobes peak at 1.625 μm with 42-nJ coupled pulse energy in DCF3 and 31-nJ pulse energy in DCF38. The inset of Fig. 2.21 shows the dispersion parameter of the two DCFs. As we expect from the simulation result in Sec. 2.1.3, negative TOD allows DCF38 to shift the leftmost spectral lobe at a wavelength shorter than that obtained from DCF3 with positive TOD.

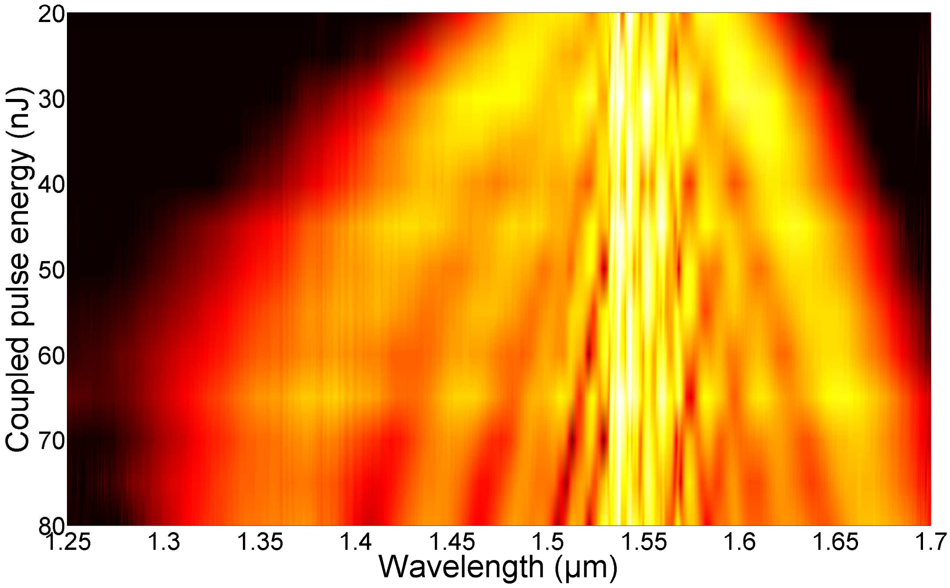

Figure 2.20: Spectral broadening in 4-cm DCF38.

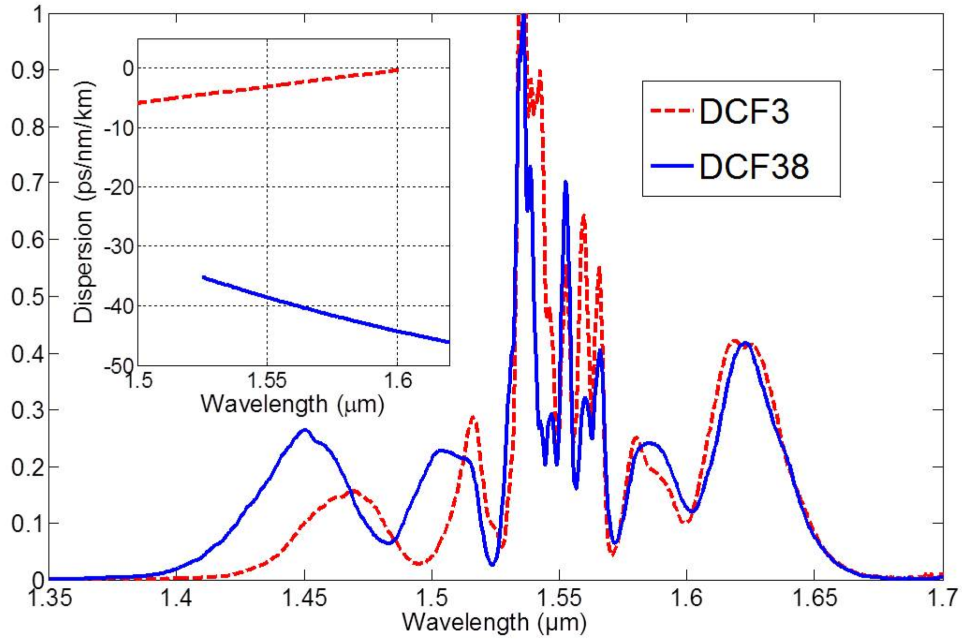

Figure 2.21: Effect of TOD on spectral broadening.

2.3.4 Tunable source between 1.3 μm and 1.7 μm

The experimental results of spectral broadening in optical fibers exhibiting different GVD at 1.55 μm can be summarized as follows:

1. Pulses propagating in fibers with negative GVD experience higher-order soliton compression. Fibers with high negative GVD are not suitable for SPM spectral broadening.

2. HNLFs featuring nearly zero GVD at the pump wavelength (1.55 μm), enables spectral broadening between 1.3 μm and 1.7 μm with well-isolated spectral lobes.

3. Pulses undergo stretching in DCFs with positive GVD, which mitigates the SPM effect.

For the application of MPM, the pulse energy and the average power are also important as well as the excitation wavelength. Figure 2.22 represents the output spectra from 4-cm HNLF1 with different coupled pulse energy of 11 nJ, 16 nJ, 22 nJ, 26 nJ, and 30 nJ. To characterize the average power of this tunable source between 1.3 μm and 1.7 μm, we use bandpass filters (BPFs) with 50-nm bandwidth (from Edmund Optics) centered at 1.3 μm, 1.35 μm, 1.4 μm, 1.45 μm, 1.6 μm, and a LPF with 1.65-μm cut-on wavelength (from Edmund Optics) to select the leftmost and the rightmost spectral lobes.

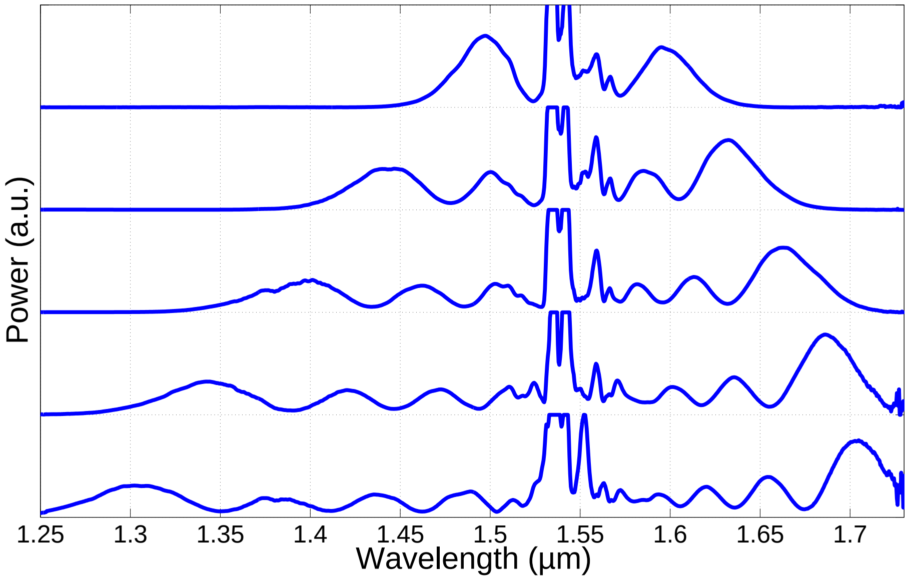

Figure 2.22: Tunable source between 1.3 μm and 1.7 μm from 4-cm HNLF1.

The corresponding filtered spectrum has an average power of 72 mW, 70 mW, 84 mW, 90 mW, 90 mW, and 122 mW, respectively, corresponding to pulse energy of 2.3 nJ, 2.3 nJ, 2.7 nJ, 2.9 nJ, 2.9 nJ, and 3.9 nJ. Typically, the microscope system will introduce >50% transmission loss (most comes from the objective), which means the available average power generated by the current source would be <50 mW (pulse energy at 1-nJ level) after the objective.

2.4 Conclusion of Chapter 2

In this chapter we numerically and experimentally studied SPM-dominated spectral broadening in optical fibers pumped by an EDFL. We first modeled ultrafast pulses propagating inside an optical fiber considering the effect of SPM, SS, SRS, and dispersion. An EDFL system was constructed under the CPA scheme with ∼5-W average output power as the pump source. This laser operates at 31-MHz repetition rate and generates 290-fs pulses centered at 1.55 μm with 160-nJ pulse energy.

We tested the spectral broadening in six optical fibers that exhibit different GVD at 1.55 μm to evaluate their potential for implementing SESS. Tunable sources in the range of 1.3-1.7 μm targeting the biological transmission window are achievable from 4-cm HNLFs. Using optical filters to select the leftmost or the rightmost spectral lobes, the resulting SESS source has an average power of 70-122 mW, corresponding to 2.3-3.9 nJ pulse energy. Considering the foreseeable microscope transmission loss while applied to MPM, the current SESS source requires further energy scaling up, which is presented in Chapter 3.

Chapter 3

Energy scalability of SESS

Besides the wavelength, the available pulse energy of the excitation pulses is as well important for MPM. In this chapter we focus on how to efficiently improve the SESS pulse energy. We also investigate the feasibility of generating SESS pulses with MW-level peak power, which is crucial for deep-tissue 3PEF imaging [28, 29, 30]

3.1 Energy scaling method for SESS

In this section we introduce two approaches to scale up the pulse energy allowed by SESS. From Eq. 3.1, we can find that the frequency shift $\Delta\omega$ due to SPM is proportional to the nonlinear phase accumulated along the propagation length L. This can be further expressed as

$$\Delta\omega \propto \phi_{NL} \propto I_0 \cdot L \propto \frac{E_p}{A_{eff}} \cdot L \tag{3.1}$$

where I_0 is the pulse peak power, L the fiber length, E_p the pulse energy, and A_{eff} the effective MFA of the fiber. It is clear that in order to achieve the same wavelength (frequency) shift, higher pulse energy is required to accumulate enough nonlinear phase for a pulse propagating in an optical fiber with a reduced fiber length or a larger MFA. Consequently the broadened spectrum has higher pulse energy distributed in each spectral lobe, thus generating SESS pulses with increased pulse energy.

3.1.1 By shortening the fiber length

We first investigate the energy scaling of SESS by shortening the fiber length. Figure 3.1 shows the simulation result of the broadened spectra for three combinations of input pulse energy (E) and fiber length (L): (blue curve, E =40 nJ, L = 4 cm), (black dashed curve, E = 80 nJ, L = 2 cm), and (red dotted curve, E = 160 nJ, L = 1 cm). The fiber has a constant GVD of 40 fs^2/mm ($\beta_3 = 0$) and a MFD of 4 μm at 1.55 μm, and the input hyperbolic-secant pulse has a duration of 300 fs.

Although the product of the input pulse energy and the fiber length is fixed at 160 nJ·cm, the combination of shorter fiber and higher input pulse energy produces more spectral broadening with deeper spectral valleys due to less GDD accumulated during the pulse propagation. Indeed the detrimental effect caused by dispersion can be reduced by using shorter fibers since dispersion is distributed along the fiber. More important, the resulting leftmost and rightmost spectral lobes account for more pulse energy. For example, the leftmost and the rightmost spectral lobes peak at 1.37 μm and 1.7 μm for 1-cm fiber with 160-nJ input pulse energy (red dotted curve in Fig. 3.1). Filtering these two spectral lobes generates ~100-fs, nearly transform-limited pulses with 32-nJ (40-nJ) pulse energy for the leftmost (rightmost) spectral lobe. Clearly using shorter fiber and higher input pulse energy for spectral broadening constitutes an efficient and energy scalable approach to obtain high-energy, wavelength widely tunable femtosecond pulses.

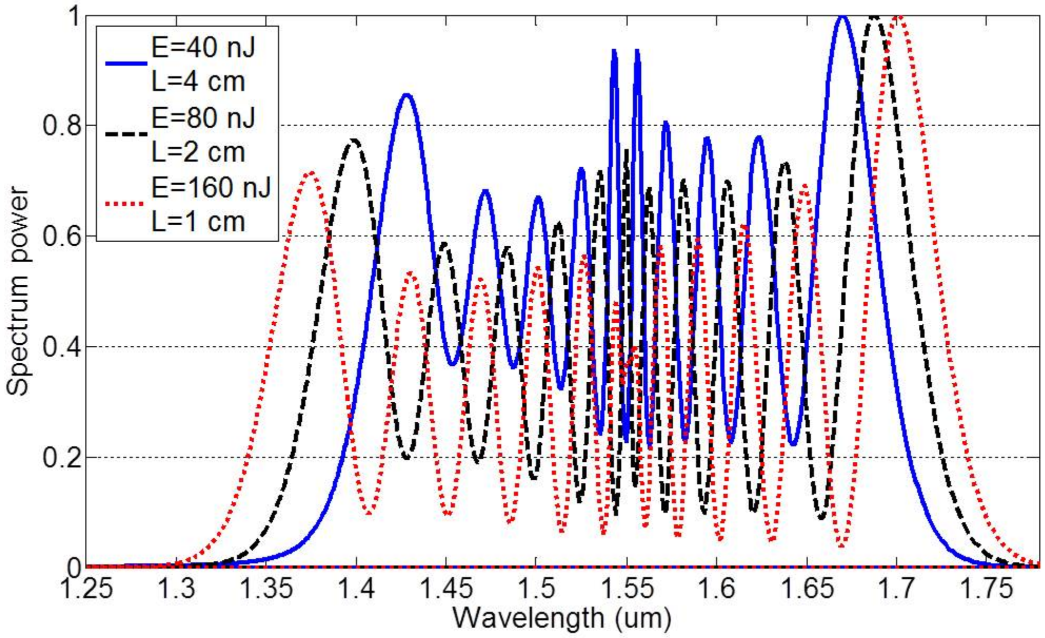

Figure 3.1: Simulation of the spectral broadening comparison among different combinations of input pulse energy and fiber length.

To experimentally demonstrate the energy scaling property offered by shortening the fiber length, we prepared another 2-cm long HNLF1 and compared its spectral broadening with those achieved in 4-cm HNLF1 (Fig. 2.17). Figure 3.2 shows the spectral broadening in 2-cm HNLF1 with coupled pulse energy varied from 10 nJ to 56 nJ. With 56-nJ coupled pulse energy, the spectrum spans from 1.3 μm to 1.7 μm featuring well-isolated spectral lobes. Except the coupled pulse energy, the spectral broadening in 2-cm HNLF1 shown in Fig. 3.2 looks almost the same with the result from 4-cm HNLF1 (Fig. 2.17).

To have a better comparison, we plotted in Fig. 3.3 the spectrum from 2-cm HNLF1 (red dotted curves) with the adjusted coupled pulse energy such that the

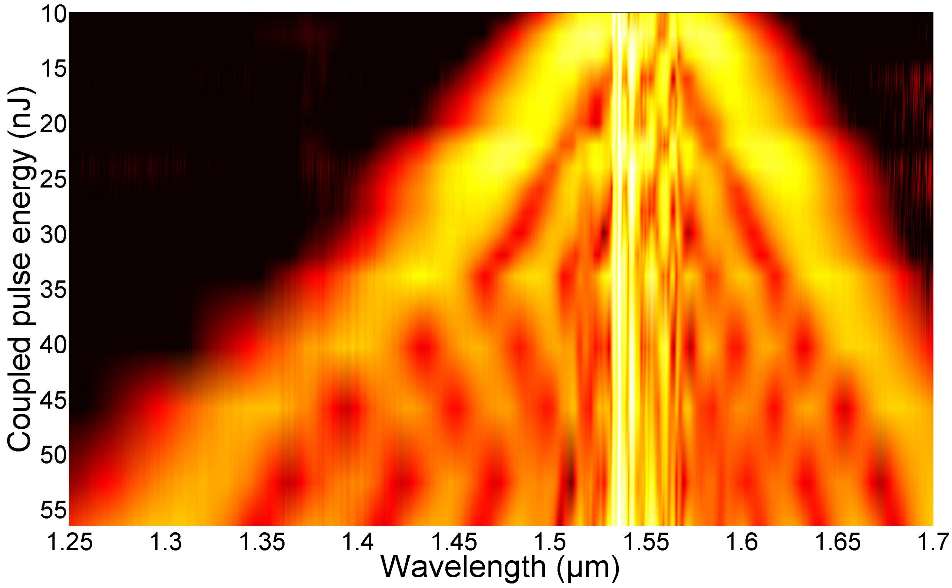

Figure 3.2: Spectral broadening in 2-cm HNLF1.

resulting rightmost spectral lobes peak at the same wavelength as those obtained from 4-cm HNLF1 (blue curves the same with Fig. 2.22).

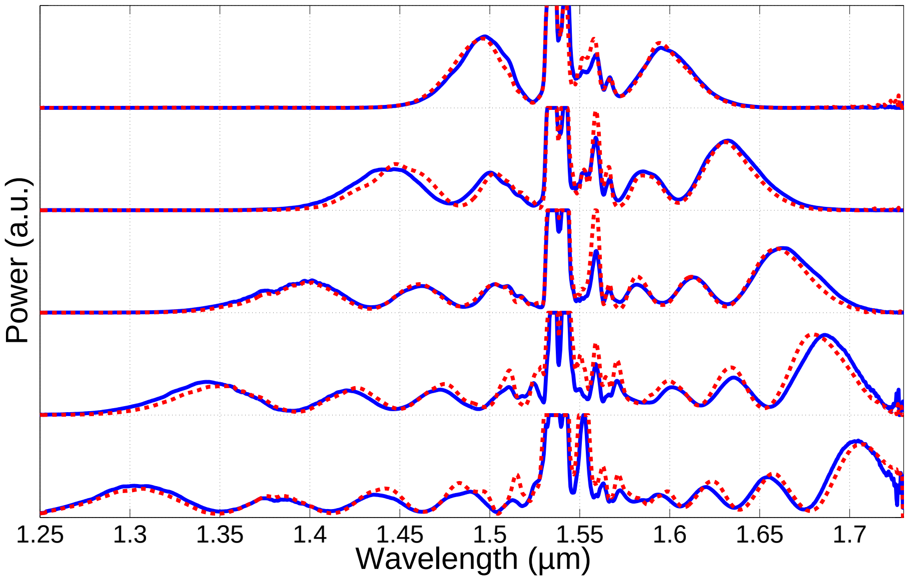

Figure 3.3: Comparison of spectral broadening in 4-cm (blue curves) and 2-cm HNLF1 (red dotted curves).

The red dotted (blue) curves in Fig. 3.3 record these output spectra with different coupled pulse energy of 18(11) nJ, 30(16) nJ, 40(22) nJ, 46(26) nJ, and 56(30) nJ. These curves almost overlap perfectly with each other. Since shortening the fiber length reduces the accumulated dispersion effect—as demonstrated by the simulation result, the ratio of pulse energies coupled into 2-cm and 4-cm HNLF1 is slightly less than two to achieve the same amount of spectral broadening.

To characterize the pulse energy and the pulse duration of the wavelength tunable source from 2-cm HNLF1, we used the same optical filters described in Sec. 2.3.4 to select the leftmost and the rightmost spectral lobes of the broadened spectrum. The left column in Fig. 3.4 presents six representatively filtered spectral lobes. They peak at 1.3 μm, 1.35 μm, 1.4 μm, 1.45 μm, 1.6 μm, and 1.7 μm with the corresponding pulse energy of 4.5 nJ, 4.8 nJ, 4.9 nJ, 5.2 nJ, 5.2 nJ, and 7.1 nJ, respectively. In contrast, the pulse energies at these six wavelengths using 4-cm HNLF1 are 2.3 nJ, 2.3 nJ, 2.7 nJ, 2.9 nJ, 2.9 nJ, and 3.4 nJ, respectively. As expected, the available pulse energies are about doubled by shortening the length of HNLF1 to its half. At 31-MHz repetition-rate, this tunable femtosecond source enabled by 2-cm HNLF1 has an average power between 140 mW and 220 mW. The corresponding pulse durations were measured by an intensity autocorrelator and the measured autocorrelation traces are shown as the red curves in the right column of Fig. 3.4. The FWHM duration of these autocorrelation traces is in the range of 149-280 fs. The pulse duration is estimated to be 97-182 fs, assuming a hyperbolic-secant pulse with a deconvolution factor of 1.54. The black dashed curves in the right column of Fig. 3.4 plot the calculated autocorrelation traces of the transform-limited pulses allowed by the filtered spectra, showing that the filtered spectra correspond to nearly transform-limited pulses.

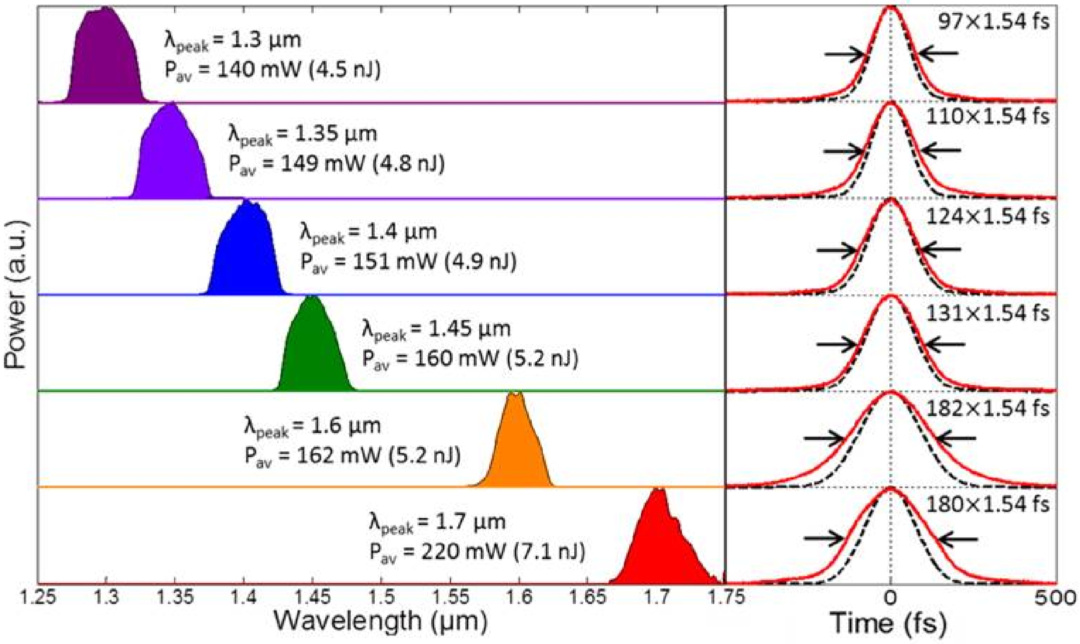

Figure 3.4: SESS between 1.3 μm and 1.7 μm from 2-cm HNLF1.

3.1.2 By using fibers with larger MFA

Besides energy scaling by shortening the fiber length, using fibers with larger MFA is another option. Larger MFD d corresponds to larger effective MFA A_{eff}, which can be described as

$$A_{eff} = \pi \left(\frac{d}{2}\right)^2 \tag{3.2}$$

In addition, larger MFA makes the free-space power coupling into the fibers less environmentally sensitive. DCFs exhibit positive GVD at 1.55 μm with their MFD larger than HNLFs. For example, DCF38 has 6-μm MFD, which is 1.5 times of the MFD of HNLF1 (4-μm), and 2.25 times of the MFA. According to Eq. 3.2, implementing SESS in DCF38 suggests an approach to double the resulting pulse energy compared with the same long HNLF1. Based on the previous result shown in Fig. 2.20, we further increased the coupled pulse energy from 80 nJ to 95 nJ in 4-cm DCF38. The spectral broadening is shown in Fig. 3.5. With the additional 15-nJ coupled pulse energy, the rightmost spectral lobe shifts to 1.7 μm, whereas the leftmost spectral lobe still remains at around 1.35 μm due to the dispersion effect.

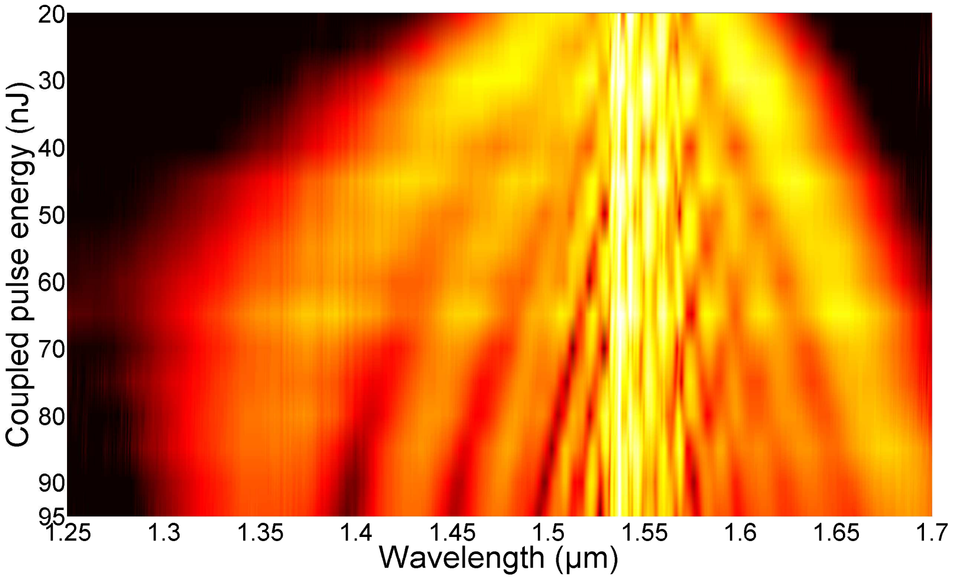

Figure 3.5: Spectral broadening in 4-cm DCF38.

With the coupled pulse energy at 96 nJ, 63 nJ, 21 nJ, and 96 nJ, 4-cm DCF38 allows us to produce a wavelength tunable source with its leftmost or rightmost spectral lobes peaking at 1.35 μm, 1.4 μm, 1.6 μm, and 1.7 μm (left column of Fig. 3.6). We used shortpass filters (SPFs) to select the spectral lobes peaking at 1.35 μm and 1.4 μm to obtain broader spectra than can be achieved by optical BPFs. As a result, the filtered spectra at these two wavelengths exhibit larger spectral bandwidth than those shown in Fig. 3.4. The corresponding pulses have the pulse energy of 10.3 nJ, 8.8 nJ, 7.4 nJ, and 10.6 nJ, respectively. The red curves in the right column of Fig. 3.6 plot the measured autocorrelation traces. Compared with the calculated autocorrelation traces of the transform-limited pulses (black dashed curves), the resulting pulses deviate considerably from transform-limited pulses mainly caused by the large GVD of DCF38. Since both positive GVD and SPM exert positive chirp to the propagating pulse, bulk materials with negative GVD can be used to dechirp the pulses given by the filtered spectra. We employed several fused-silica plates to dechirp these pulses. The measured autocorrelation traces of the dechirped pulses are shown as the purple curves in the right column of Fig. 3.6. They nearly overlap with the black dashed curves showing that the dechirped pulses are nearly transform-limited. The pulse duration is estimated to be 52-143 fs, assuming a hyperbolic-secant pulse with a deconvolution factor of 1.54.

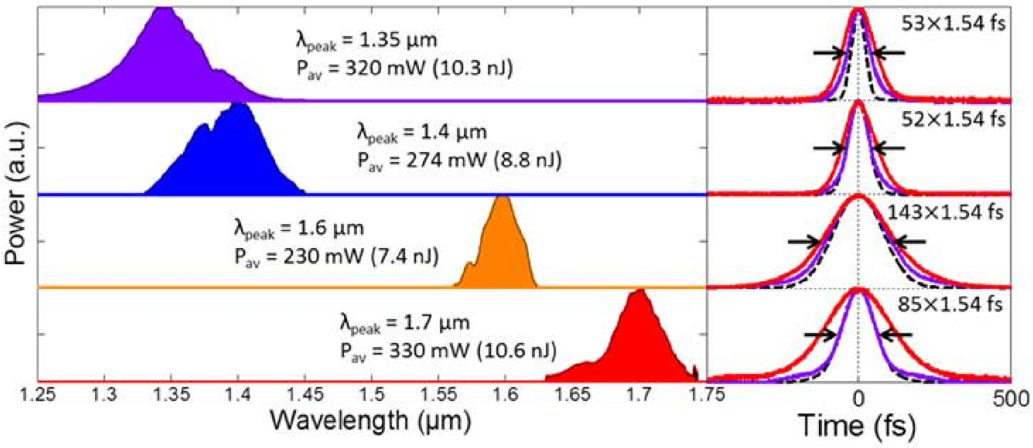

Figure 3.6: SESS between 1.35 μm and 1.7 μm from 4-cm DCF38.

Apparently SESS in 4-cm DCF38 produces wavelength tunable femtosecond pulses with higher pulse energy than in 4-cm HNLF1. For example, the 1.35-μm pulses generated by 4-cm DCF38 possess 10.3-nJ pulse energy and 53-fs pulse duration, while 2-cm HNLF produces the 1.35-μm pulses with 4.8-nJ pulse energy and 110-fs pulse duration. This means that the pulse peak power differs by a factor of 4 for these 1.35-μm sources. Use of a femtosecond source with higher pulse energy and shorter pulse duration is of particular importance to increase the signal strength in MPM. According to Eq. 1.19, the signal for 3PEF becomes 32 times stronger if the driving pulse duration is reduced by a factor of 2 while the pulse energy is doubled [95].

3.2 SESS implemented in fibers with negative GVD

SESS implemented in 4-cm DCF38 allows us to generate ~10-nJ, <100-fs pulses at 1.35 μm and 1.7 μm. In order to further scale the pulse energy up to >100 nJ and therefore achieve ~1-MW peak power—a power level required by applications such as deep-tissue 3PEF imaging [28, 29, 30], the fiber length should be reduced to ~4 mm, which becomes challenging for experimental handling. In addition, the small MFD (6 μm for DCF38) also degrades the system robustness when free-space coupling is adopted.

As we have shown, besides shortening the fiber length, energy scaling can be also achieved by employing optical fibers with larger MFA. SESS implemented in LMA fibers has been successfully demonstrated by using YDFL pump sources [73, 74]. Most of the conventional optical fibers—especially fused silica LMA fibers—exhibit positive GVD at the YDFL wavelength (i.e., ~1.03 μm), but negative GVD at the EDFL wavelength (i.e., ~1.55 μm). Though specially designed fibers at the expense of the fiber MFA may possess close-to-zero or even positive GVD at the EDFL wavelength. At 1.55 μm, however, increasing the fiber MFA normally leads to negative GVD that complicates the nonlinear propagation of an ultrashort pulse inside the fiber, shown as the result from standard SMFs demonstrated in Sec. 2.3.1. Negative GVD and strong SPM can reshape the input pulse into a higher-order optical soliton. Due to higher-order effects such as TOD, SS, and SRS, this higher-order soliton breaks into multiple fundamental solitons and emits dispersive waves; further propagation leads to wavelength red-shifted Raman solitons [85].

Ultrashort pulse propagating inside an optical fiber with negative GVD has been extensively investigated under the context of higher-order soliton pulse compression, supercontinuumm generation, and SSFS [67]. At first glance, optical fibers with negative GVD are not suitable for implementing SESS because efficient SESS requires the formation of well-isolated spectral lobes with a considerable portion of power concentrated in the leftmost/rightmost spectral lobes. However, it is still feasible to implement SESS in fibers exhibiting negative GVD since the spectral broadening is dominated by SPM prior to soliton fission. Before we present the experimental results, we first use numerical simulations to illustrate this assumption and study the effect of different sign of dispersion on the spectral broadening at the pump wavelength of 1.55 μm.

3.2.1 Higher-order soliton compression and fission

Similar to Sec. 2.1, we solve the GNLSE to investigate the effect of GVD on the spectral broadening at the pump wavelength of 1.55 μm. Without loss of generality, we propagate an ultrashort pulse inside three fibers featuring positive (10 fs^2/mm), zero (0 fs^2/mm), and negative (-10 fs^2/mm) GVD, respectively. To be more practical, we assume constant TOD of 100 fs^3/mm at 1.55 μm for all three cases. The input pulse (center wavelength at 1.55 μm) has a hyperbolic-secant shape with 300-fs pulse duration and 95-nJ pulse energy. We assume that these three fibers have the same MFD of 10 μm. The simulation results of the spectral and temporal evolution along the fiber length are shown in Fig. 3.7 and Fig. 3.8, respectively.

For pulses propagating inside the fiber with 10 fs^2/mm GVD, SPM dominates the spectral broadening and forms well-separated spectral lobes [Figure 3.7(a)]. Due to the positive GVD, the input pulse is gradually stretched along the propagation distance [Fig. 3.8(a)]. In contrast, for propagation in the fiber with zero GVD, the pulse duration remains almost constant [Fig. 3.8(b)]; consequently the broadened spectrum [Fig. 3.7(b)] spans a little wider than the spectrum achieved in the fiber with positive GVD.

Figure 3.7(c) depicts the spectral evolution of the input pulse propagating in the fiber with negative GVD of -10 fs^2/mm. Its corresponding temporal evolution is shown in Fig. 3.8(c). Due to higher-order soliton pulse compression arising from the interaction between SPM and negative GVD, the input pulse becomes shorter along the propagation length. It reaches the shortest pulse duration at the fiber length of 5.2 cm, which is defined as the soliton fission length and denoted by white dashed lines in Fig. 3.7(c) and 3.8(c). Further propagation leads to soliton fission that ejects multiple pulses, which starts to destroy the spectral structure of well-separated lobes that originates from SPM-dominated spectral broadening [Fig. 3.7(c)]. The washout process is experimentally observed in standard SMFs presented in Sec. 2.3.1.

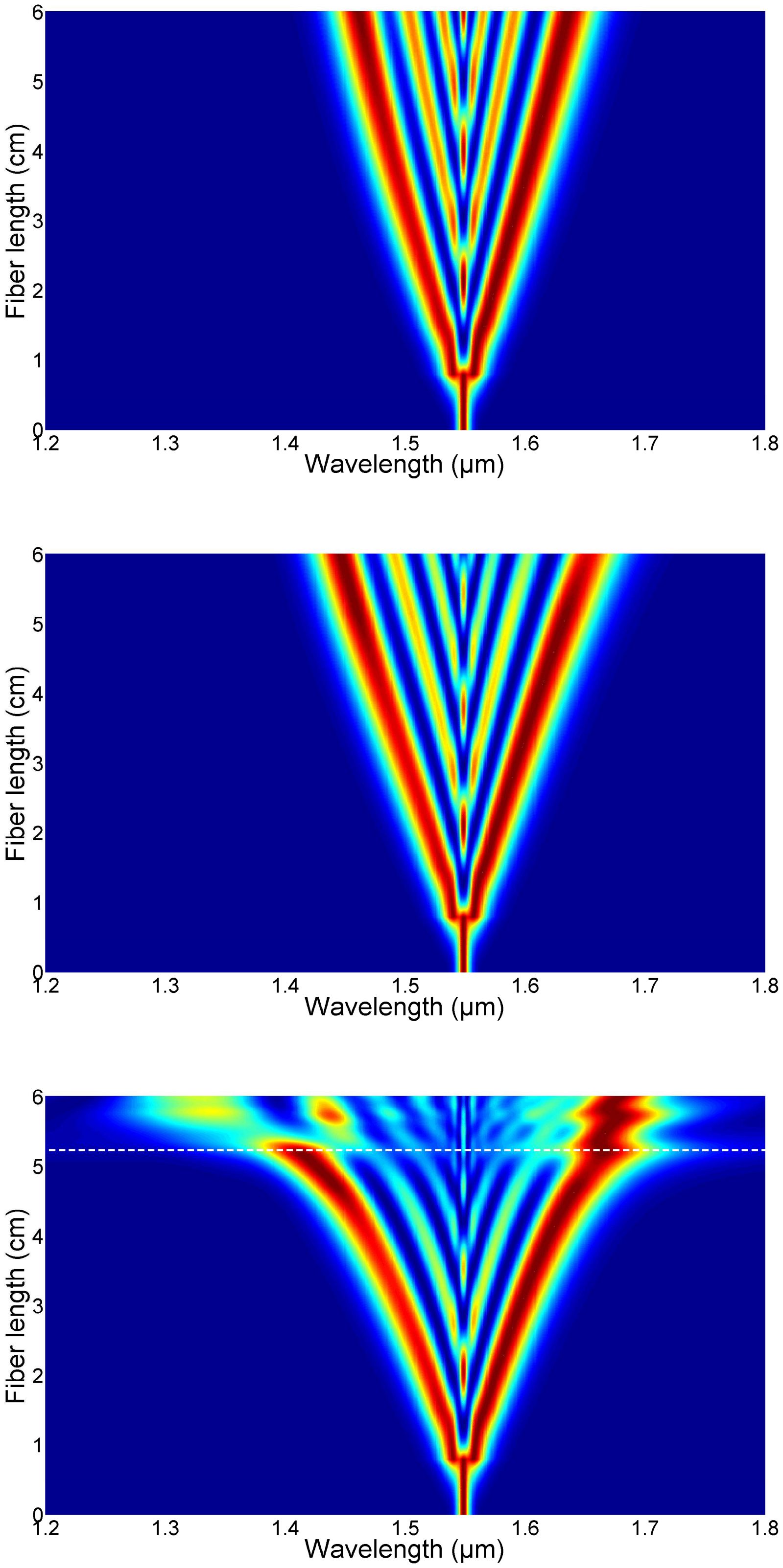

Figure 3.7: Simulation of the spectral evolution in fibers with different GVD at 1.55 μm. (a) 10 fs^2/mm. (b) 0 fs^2/mm. (c) -10 fs^2/mm.

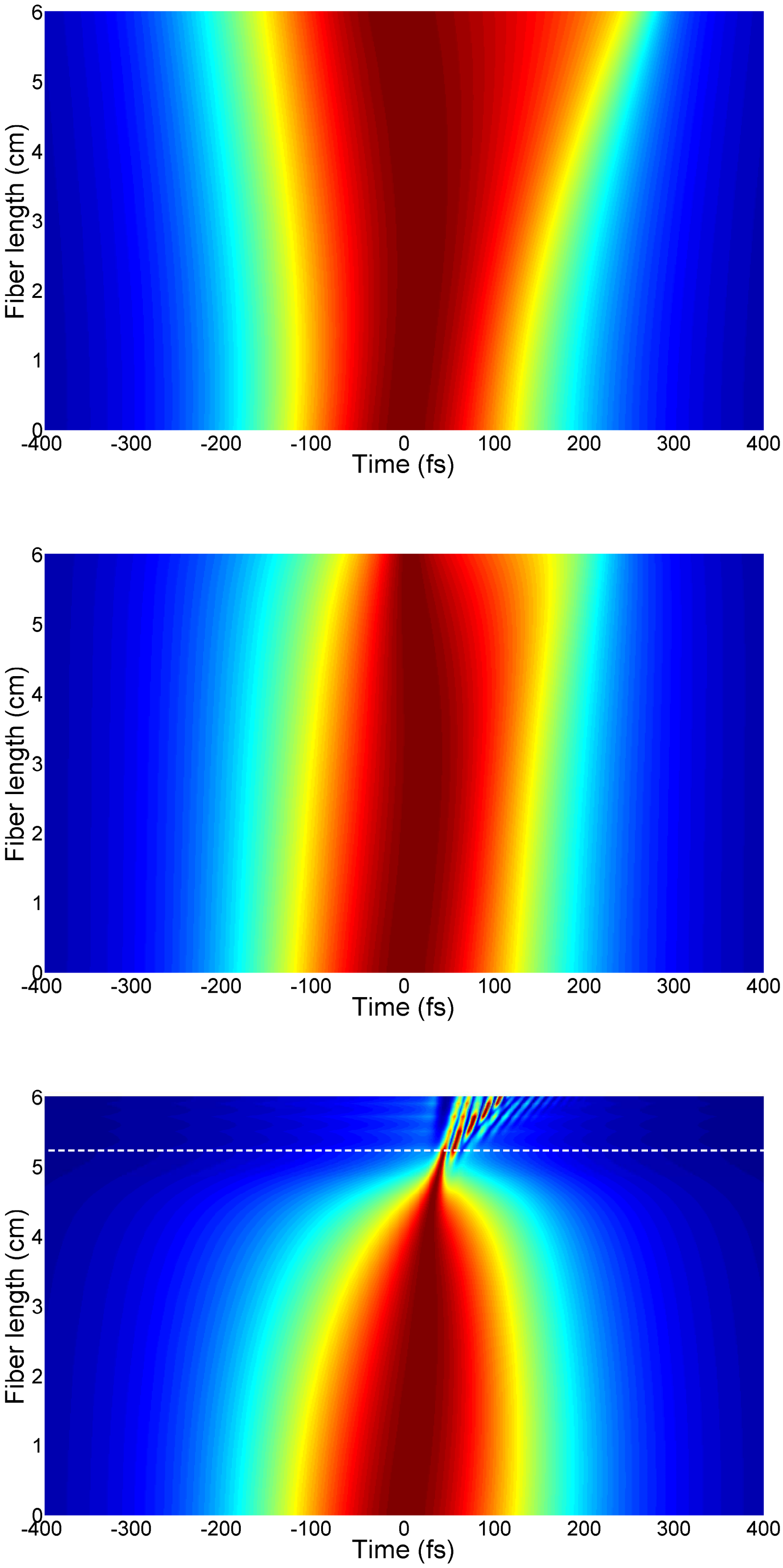

Figure 3.8: Simulation of the temporal evolution in fibers with different GVD at 1.55 μm. (a) 10 fs^2/mm. (b) 0 fs^2/mm. (c) -10 fs^2/mm.

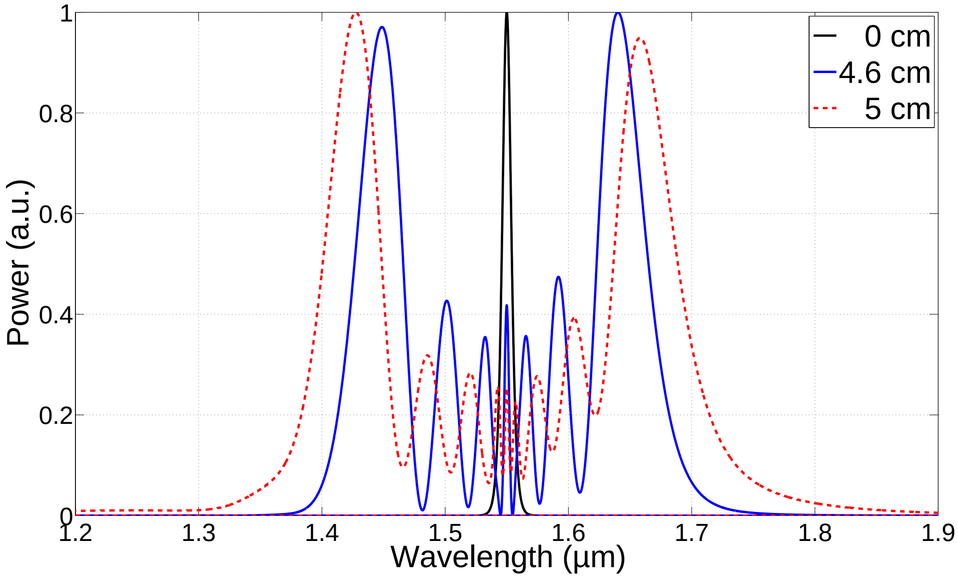

Figure 3.9: Simulation of the spectral evolution after different propagation distance.

To visualize more details, we plot in Fig. 3.9 the evolved spectra at the propagation lengths of 4.6 cm (blue curve) and 5 cm (red dashed curve). For a comparison, we plot in the same figure the spectrum at the fiber input (black curve). Clearly the input narrowband spectrum is substantially broadened and extended towards both the shorter and the longer wavelength side.

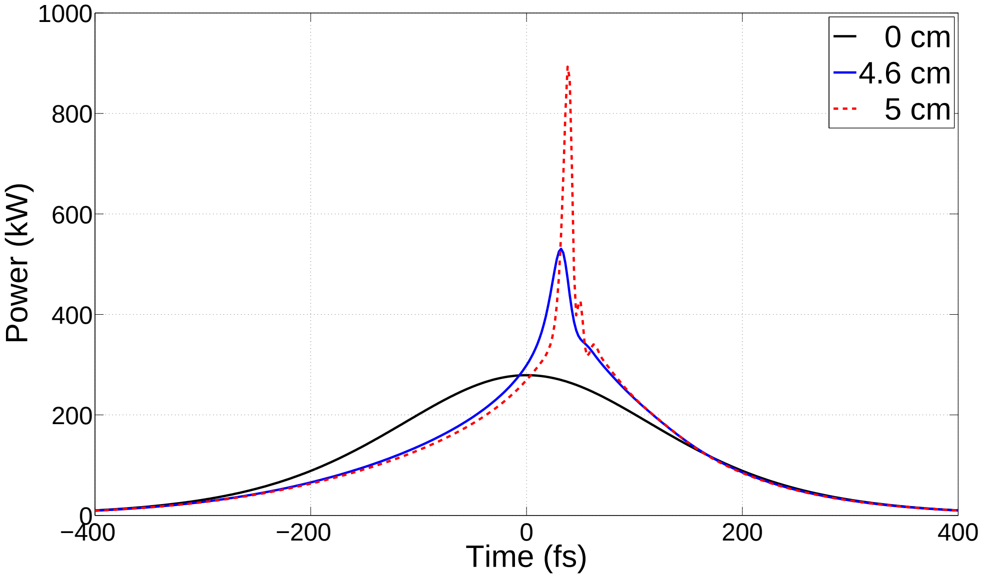

Figure 3.10: Simulation of the temporal evolution after different propagation distance.

The corresponding temporal pulses at these three propagation distances are shown in Fig. 3.10. In the time domain, the pulse experiences an accelerated pulse compression; the peak power increases from 279 kW to 530 kW after propagation of 4.6 cm (black and blue curves in Fig. 3.10). Then after further propagation of 0.4 cm, the peak power reaches 893 kW (red dashed curve in Fig. 3.10). The results suggest that when implementing SESS in optical fibers with negative GVD, fiber length should be less than the soliton fission length to ensure SPM-dominated spectral broadening. The soliton fission length can be estimated as [67]

$$L_{fiss} \sim \frac{L_D}{N} = \frac{{T_0}^2/\left|\beta_2\right|}{\sqrt{\gamma E T_0/\left|\beta_2\right|}} = \sqrt{\frac{{T_0}^3}{\left|\beta_2\right|\gamma E}} \tag{3.3}$$

where L_D is the characteristic dispersive length scale, N the soliton order, T_0 is related to the FWHM pulse duration by $T_0 \sim T_{FWHM}/1.763$ assuming a hyperbolic-secant pulse. β_2 is the GVD, γ the nonlinear parameter of the optical fiber, and E the input pulse energy. In our simulation, these parameters are T_{FWHM} = 300 fs, β_2 = -10 fs^2/mm, γ = 1.73 /W/km, and E = 95 nJ, which results in L_{fiss} = 5.5 cm and agrees well with the soliton fission length of 5.2 cm obtained by numerical simulation.

Equation 3.3 suggests that the soliton fission length is inversely proportional to the square root of the input pulse energy—a relation that favors SESS energy scaling. For example, as we quadruple the input pulse energy, the corresponding soliton fission length is reduced by half. Then we intuitively expect more accumulated nonlinear phase and a wider broadened spectrum. To numerically confirm such a speculation, we increase the input pulse energy from 95 nJ to 380 nJ, propagate the pulse in the fiber with -10 fs^2/mm GVD, and plot the spectral evolution in Fig. 3.11(b) for a fiber length up to 2.6 cm. For a clear comparison, Fig. 3.11(a) shows the spectral evolution for the input pulse with 95-nJ pulse energy and the fiber length is set to be 5.2 cm.

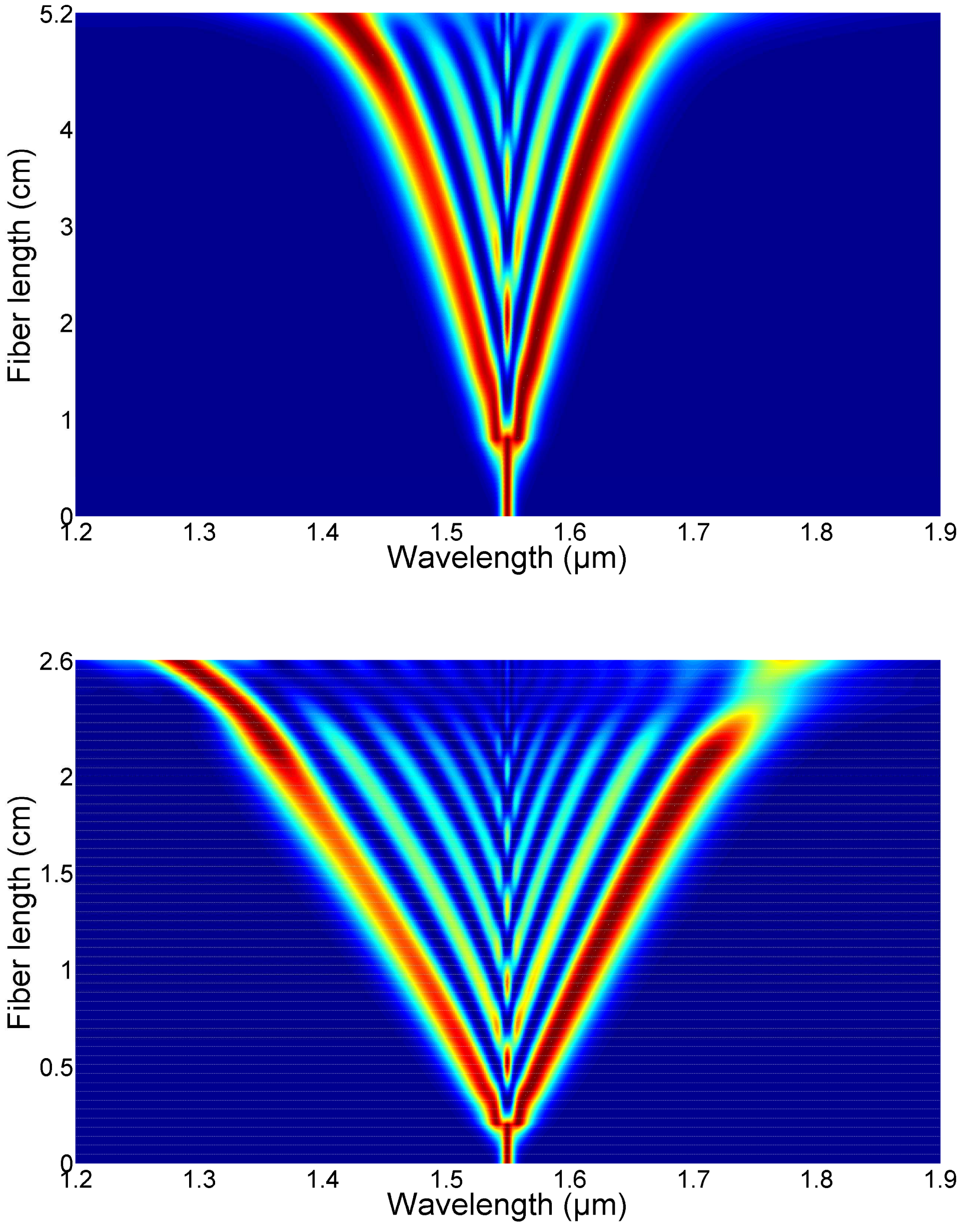

Figure 3.11: Simulation of the spectral evolution from different combinations of input pulse energy and fiber length. (a) 95 nJ, 5.2 cm. (b) 380 nJ, 2.6 cm.

Except the similar spectral evolution shown in Fig. 3.11, increasing the input pulse energy leads to a much wider SPM-dominated spectral broadening. To illustrate this point, we plot the spectra in Fig. 3.12(a) and the pulses in Fig. 3.12(b) from different combinations of pulse energy and fiber length. For 95-nJ pulse energy and 4.6-cm fiber length, the leftmost and the rightmost spectral lobes peak at 1.45 μm and 1.64 μm, respectively [blue curve in Fig. 3.12(a)]. As we increase the pulse energy to 380 nJ and reduce the fiber length to 2.3 cm, these two lobes peak at 1.34 μm and 1.74 μm, respectively [red dashed curve in Fig. 3.12(a)].

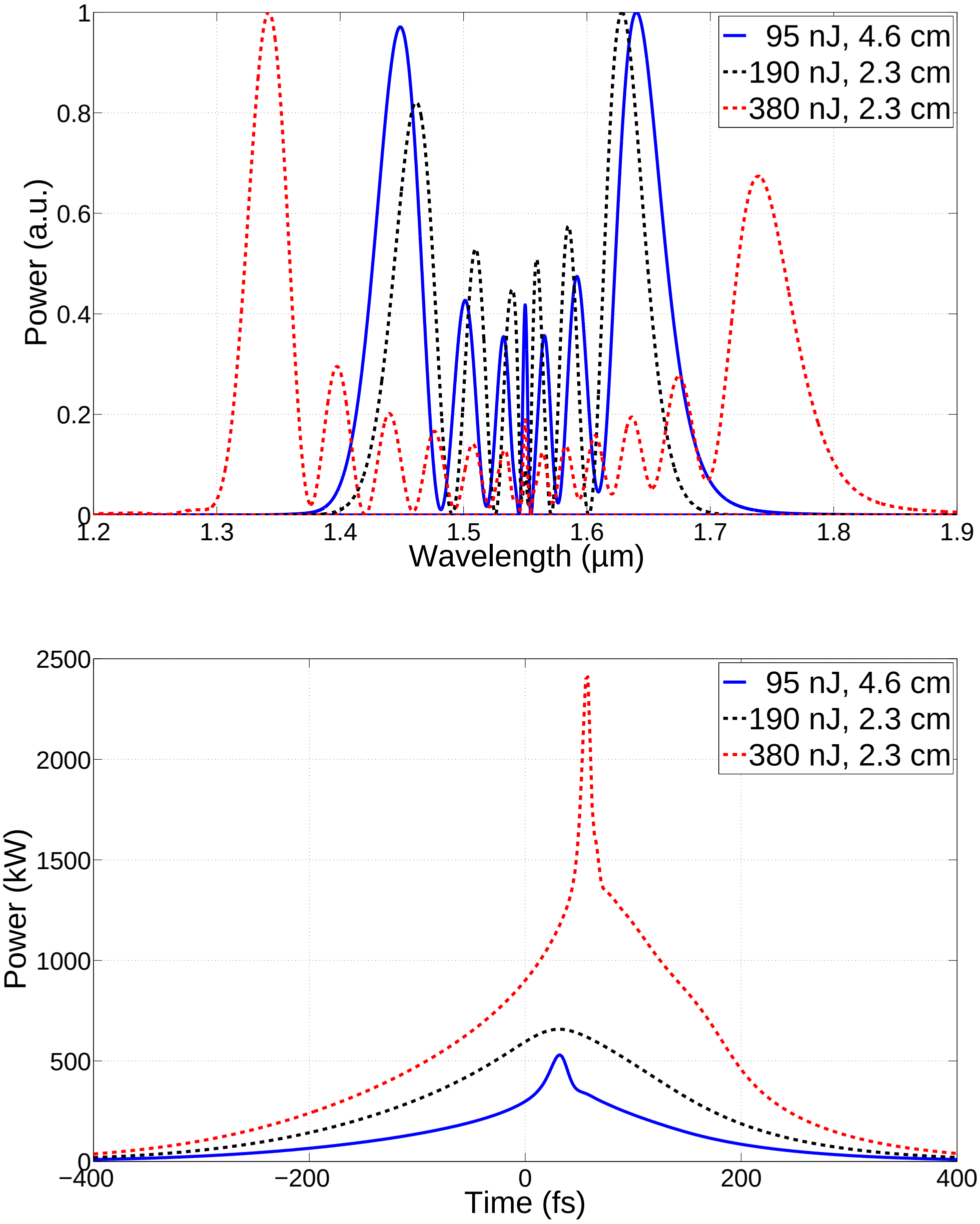

Figure 3.12: Simulation of the (a) spectral broadening and (b) evolved pulses from different combinations of input pulse energy and fiber length.

The blue curve and the red dashed curve in Fig. 3.12(b) clearly show the higher-order soliton compression. For a better understanding of energy scaling, we also plot in Fig. 3.12(b) the simulation results corresponding to 190-nJ input pulse energy and 2.3-cm fiber length. From Eq. 3.3, we can estimate that the soliton fission length for the 190-nJ pulse is about 3.9 cm. As a result, the propagation of 190-nJ pulses inside 2.3-cm fiber introduces negligible pulse compression [black dashed curve in Fig. 3.12(a)]. This explains why the resulting spectrum [black dashed curve in Fig. 3.12(a)] is narrower than the one generated from the 95-nJ pulse propagating in 4.6-cm long fiber [blue curve in Fig. 3.12(a)]. Such behavior contrasts with SPM-dominated spectral broadening in optical fibers with positive GVD, for which reducing the fiber length by a factor of two and doubling the input pulse energy leads to wider broadened spectrum due to less pulse stretching as discussed in Sec. 3.1.1.

To demonstrate SESS, we numerically filter the leftmost and the rightmost spectral lobes from the broadened spectrum given by the 380-nJ pulse propagating through 2.3-cm fiber; the resulting pulses are plotted as the blue curves in Fig. 3.13. The filtered spectral lobes are shown as the insets (black curves). More specific, the filtered leftmost spectral lobe produces an 87-fs, 117-nJ pulse [blue curve in Fig. 3.13(a)] and the rightmost spectral lobe produces a 102-fs, 121-nJ pulse [blue curve in Fig. 3.13(b)]. Both pulses exhibit >1-MW peak power. The transform-limited pulses [red curves in Fig. 3.13] calculated from the filtered spectra have a duration of 78 fs and 98 fs, respectively, showing that the SESS pulses are nearly transform-limited. These two spectral lobes have a total pulse energy of 238 nJ, which accounts for >60% of the 380-nJ input pulse energy, representing an efficient wavelength conversion process.

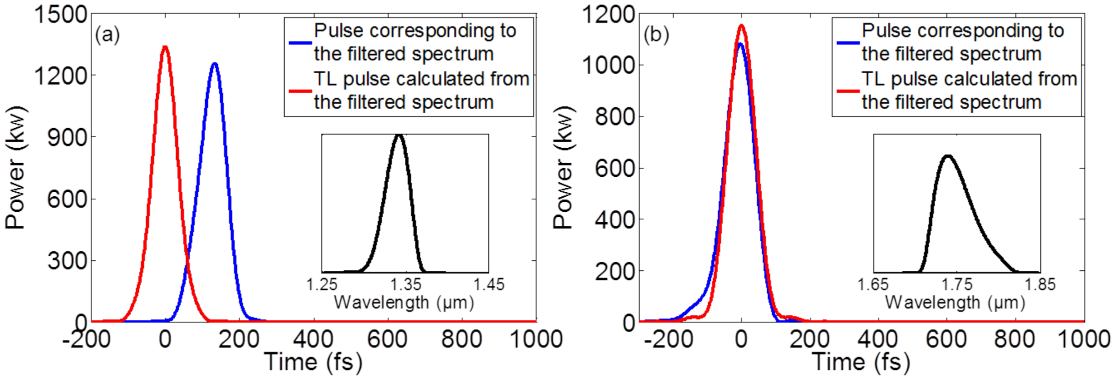

Figure 3.13: Numerically filtered pulses from (a) the leftmost and (b) the rightmost spectral lobe.

3.2.2 SESS in DSF

To verify our assumptions, we tested DSFs exhibiting GVD and MFD similar to the simulation parameters. Limited by the available pulse energy, we compare the spectral evolution at two fiber lengths (14 cm versus 7 cm) that are longer than those discussed in Sec. 3.2.1. Figure 3.14 shows the spectrum at the output of 14-cm DSF for the coupled pulse energy varied from 10 nJ to 100 nJ. As the coupled pulse energy increases from 10 nJ to 35 nJ, the spectrum gradually broadens towards the shorter and the longer wavelength forming several isolated spectral lobes. Further increasing the coupled pulse energy leads to soliton fission, washout of the well-isolated spectral lobes, and supercontinuum generation spanning from 1.1 μm to 1.7 μm.

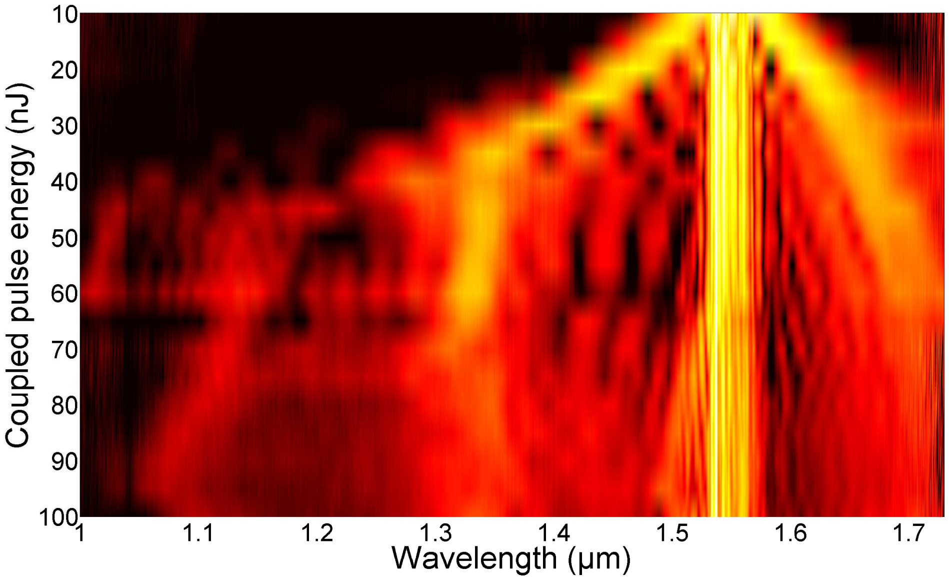

Figure 3.14: Spectral broadening in 14-cm DSF.

Figure 3.15 shows the output spectrum from 7-cm DSF. Obviously, SPM-induced spectral broadening dominates almost the whole process as the coupled pulse energy varied from 10 nJ to 115 nJ.

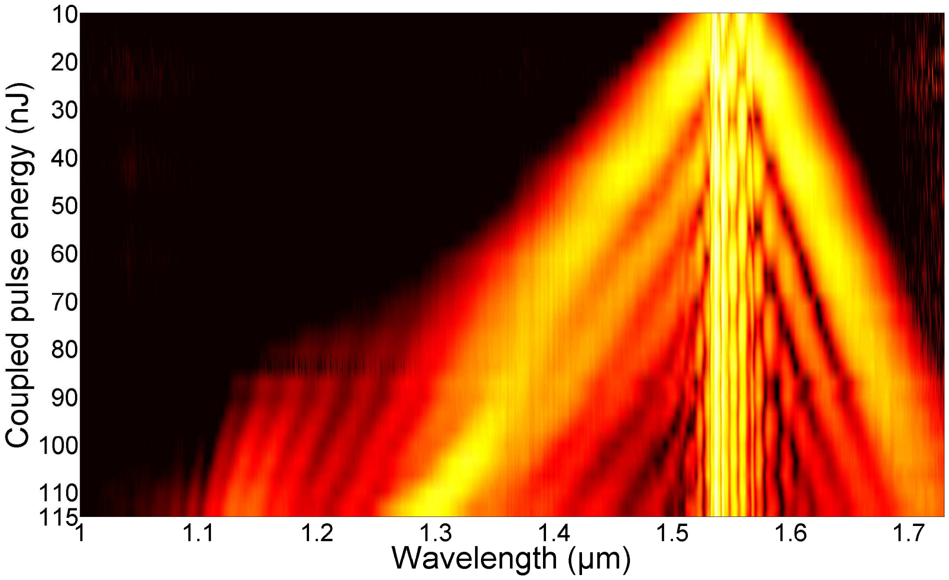

Figure 3.15: Spectral broadening in 7-cm DSF.

The well-isolated spectral lobes indicate that the soliton fission has not occurred yet compared with the result from 14-cm DSF (Fig. 3.14). Besides the spectral lobes spanning from 1.3 μm to 1.7 μm, optical wave breaking happens and contributes to the spectrum generated in the shorter wavelength range of 1.1-1.2 μm.

To investigate the energy scaling in DSF exhibiting negative GVD by shortening the fiber length, we obtain the spectra at different combinations between fiber length and coupled pulse energy shown in Fig. 3.16. The blue curve in Fig. 3.16 plots the broadened spectrum of 28-nJ pulses propagating in 14-cm DSF; the leftmost and the rightmost spectral lobes peak at 1.42 μm and 1.64 μm, respectively. As we reduce the fiber length to 7 cm and increase the coupled pulse energy to 56 nJ, the resulting spectrum (red curve) broadens less compared with the blue curve; the leftmost and the rightmost spectral lobes peak at 1.44 μm and 1.62 μm, respectively. Due to the less pulse compression experienced during the propagation in a shorter fiber, 7-cm DSF requires 65-nJ (more than the double of 28 nJ) pulses to achieve similar spectral broadening (green curve). It is noteworthy that even though the blue curve and the green curve peak at similar wavelength, the shape of their spectral lobes and the energy distribution in the spectra are quite different due to the GDD accumulated and the temporal shape of the evolved pulse. As we further increase the coupled pulse energy to 112 nJ (4 times of 28 nJ), spectral broadening in 7-cm DSF shifts the leftmost spectral lobe to 1.32 μm and the rightmost one to 1.69 μm (purple curve). Clearly the results shown in Fig. 3.16 qualitatively agree with the simulation results presented in Fig. 3.12(a).

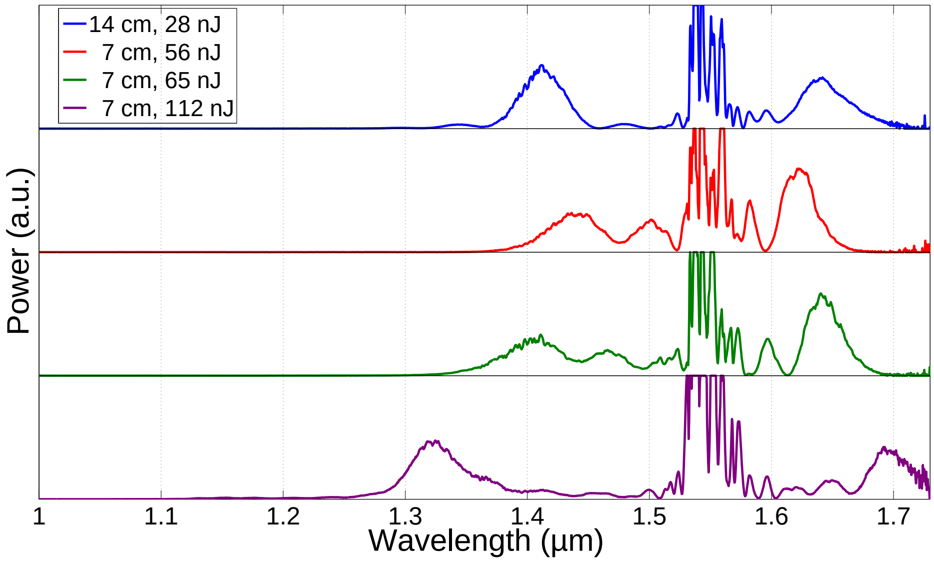

Figure 3.16: Output spectra from DSF of different length and coupled pulse energy.

The experimental results in Fig. 3.16 show once again that energy scaling can be achieved by increasing the input pulse energy and meanwhile shortening the fiber length. Reducing the fiber length to its half allows quadrupled input pulse energy for wider spectral broadening, even in optical fibers with negative GVD, as long as it is operating prior to the soliton fission. With the help of higher-order soliton compression, SPM-dominated spectral broadening in 7-cm DSF occurs effectively, which constitutes a tunable femtosecond source between 1.3 μm and 1.7 μm.

To characterize the pulse energy of this SESS source, we use the same optical filters as in Sec. 2.3.4 and Fig. 3.4 to select the leftmost/rightmost spectral lobes peaking at 1.3 μm, 1.35 μm, 1.4 μm, 1.45 μm, 1.6 μm, and 1.7 μm, respectively. The six representative filtered spectral lobes are plotted in the left column of Fig. 3.17. The corresponding pulse energies are 15.8 nJ, 11.9 nJ, 7.4 nJ, 6.6 nJ, 11.3 nJ, and 15.5 nJ. At 31-MHz repetition rate, this tunable femtosecond source has an average power of 205-490 mW. The corresponding pulse duration given by these six spectra is measured by an intensity autocorrelator and the measured autocorrelation traces are shown as the red solid curves in the right column of Fig. 3.17. The FWHM duration of these autocorrelation traces is 149-234 fs, so the pulse duration is estimated to be 97-152 fs assuming a hyperbolic-secant pulse with a deconvolution factor of 1.54. The black dashed curves in the right column plot the calculated autocorrelation traces of the transform-limited pulses allowed by the filtered spectra, showing that the filtered spectra generate nearly transform-limited pulses.

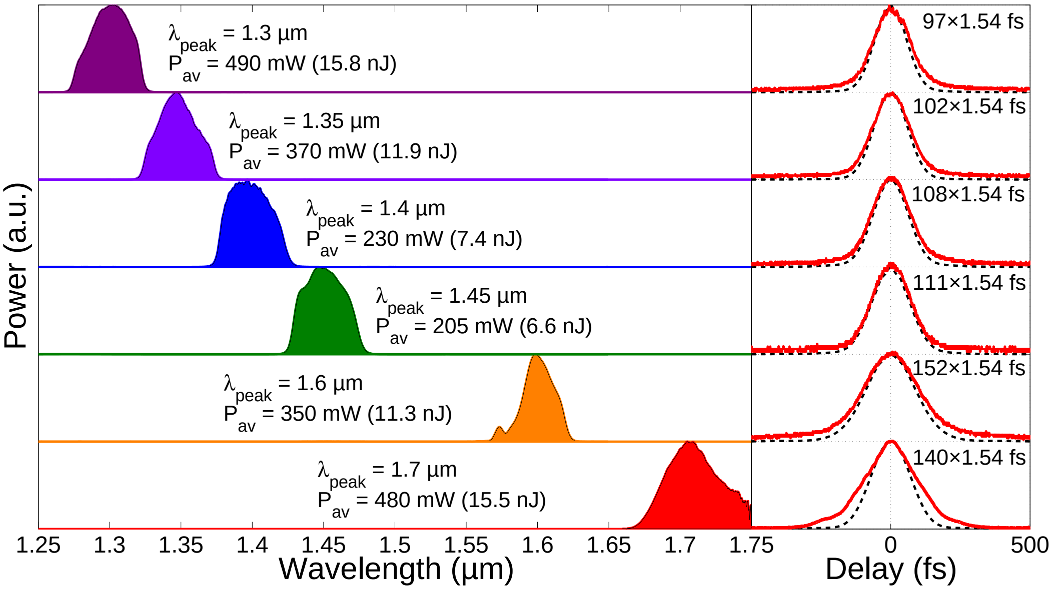

Figure 3.17: SESS between 1.3 μm and 1.7 μm from 7-cm DSF.

3.2.3 SESS source with MW peak power

It is noteworthy that 1.3 μm and 1.7 μm correspond to two important optical transmission windows for biomedical imaging [26, 27, 96]. Femtosecond pulses at these two wavelengths are regarded as the best choice for deep-tissue imaging [28, 29, 30]. Depending on the biological sample and the imaging modality, ultrafast sources generating femtosecond pulses with MW peak power are highly desired [28, 29, 30]. Limited by the available pulse energy of 160 nJ provided by our current EDFL, the SESS source based on 7-cm DSF produces ∼100-fs pulses with ∼16-nJ pulse energy at both 1.3 μm and 1.7 μm. The resulting peak power is at the 0.1-MW level. To show the feasibility of further energy scaling, we replace the EDFL by a home-built OPA system that is pumped by a Ti:sapphire laser operating at 3-kHz repetition rate.

The signal pulse from the OPA is tunable between 1.2 μm and 1.6 μm with ∼40-fs pulse duration. To match the pulse parameters of our EDFL system, we intentionally tune the signal wavelength to 1.55 μm and use a BPF to select a narrowband spectrum that supports ∼300-fs pulses. We couple this narrowband pulse into 1.3-cm DSF. By varying the input pulse energy, we can fine tune the peak wavelength of the leftmost/rightmost spectral lobes.

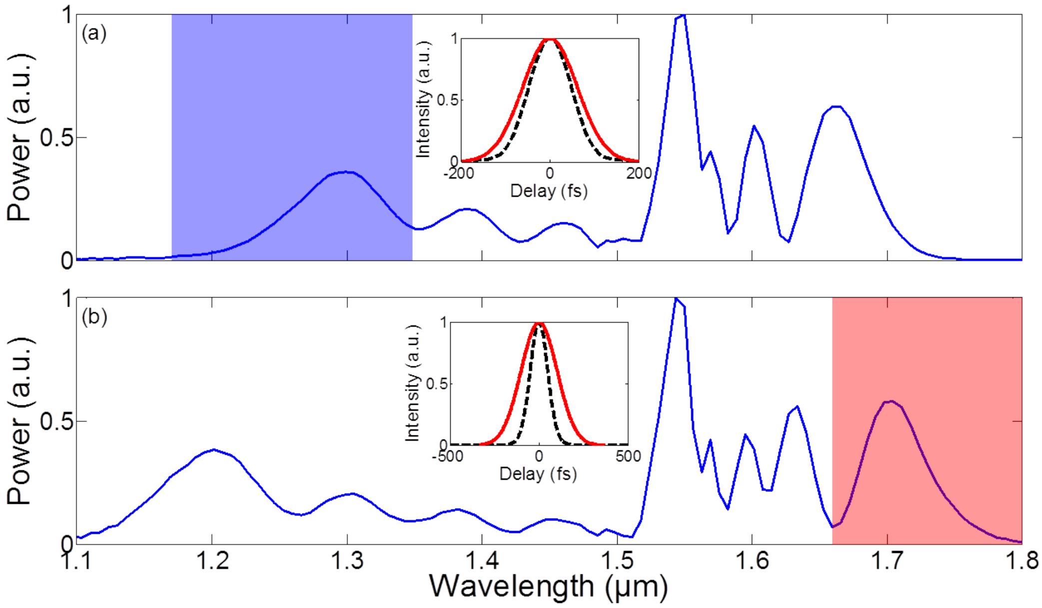

Figure 3.18: SESS source with MW peak power at (a) 1.3 μm and (b)1.7 μm.

At the 760-nJ coupled pulse energy, the leftmost spectral lobe peaks at 1.3 μm [Fig. 3.18(a)]; we use an optical filter to select this spectral lobe and obtain 130-nJ pulse energy. The resulting pulse is measured by an intensity autocorrelator. The measured autocorrelation trace—shown as the red curve in the inset of Fig. 3.18(a)—suggests a 94-fs pulse duration assuming a deconvolution factor of 1.54. The black dashed curve represents the calculated autocorrelation trace for the transform-limited pulse. Given 130-nJ pulse energy and estimated pulse duration of 94 fs, the pulse peak power should exceed 1 MW. To shift the rightmost spectral lobe to 1.7 μm [Fig. 3.18(b)], we increase the coupled pulse energy to 830 nJ. The filtered pulse at 1.7 μm has 110-nJ pulse energy and an estimated pulse duration of 150 fs [red curve in the inset of Fig. 3.18(b)]. The resulting peak power is also at the MW level. It is worth noting that the leftmost spectral lobe in Fig. 3.18(b) peaks at

1.2 μm. Filtering this spectral lobe should also lead to femtosecond pulses with ~100-nJ pulse energy and MW peak power.

3.3 Conclusion of Chapter 3

In this chapter we first introduce two approaches—either by shortening the fiber length or by using fibers with larger MFA—to scale up the available pulse energy generated by SESS. For example, implementing SESS in 4-cm DCF38 results in ultrafast sources widely tunable from 1.35 μm to 1.7 μm with up to >10-nJ pulse energy and pulse duration as short as ~50 fs.

Then we present a detailed numerical and experimental study on SESS operating in optical fibers with negative GVD. Although spectral broadening inside optical fibers with negative GVD involves higher-order soliton compression and soliton fission, our results show that SPM dominates the spectral broadening prior to soliton fission. Before soliton fission occurs, higher-order soliton compression increases the peak power and accelerates the spectral broadening. Implementing SESS in 7-cm DSF leads to a femtosecond source that can be tuned between 1.3 μm and 1.7 μm with up to ~16-nJ pulse energy and ~100-fs pulse duration. At 31-MHz repetition rate, the available average power is almost half Watt, which is quite sufficient for most of the MPM applications. By further increasing the input pulse energy to ~1-μJ (offered by a home-built OPA) and reducing the DSF length to 1.3 cm, we significantly scale up the pulse energy of such a SESS source. More specific, we achieve >100-nJ femtosecond pulses at 1.3 μm and 1.7 μm while the peak power reaches the MW level.

This wavelength widely tunable energetic femtosecond source constitutes a powerful tool to drive MPM. We demonstrate such applications driven by an EDFL-based SESS source in the following two chapters.

Chapter 4

Ultrafast SESS source for HGM imaging in human skin

Biopsy is an important technique for pathology, morphology, and disease diagnostics. In this chapter, we demonstrate HGM as a tool for optical virtual skin biopsy driven by an EDFL-based ultrafast SESS source.

4.1 Optical virtual skin biopsy

Forming the boundary that separates the organism and the environment, human skin covers nearly the whole body and provides many significant functions. It consists of three layers. The outermost layer—epidermis—mainly consists of keratinocytes which are built from epidermal stem cells in the basal membrane between epidermis and dermis. The epidermis can be subdivided into four different stratums from its surface to the bottom, i.e., stratum corneum (SC), stratum granulosum (SG), stratum spinosum (SS), and stratum basale (SB). Each of them is characterized by different cell shapes. Also located in the basal membrane are the melanocytes, which produce the pigment melanin. The melanin is then transported to surrounding keratinocytes to give color to the epidermis. The dermis makes up the bulk of human skin and provides physical protection. The main cellular components of the dermis are fibroblast. Deeply embedded in the dermis are the hair follicles and skin glands, which are derived from the epidermis. The so-called buldge region of the hair follicle is an important stem cell reservoir for melanocytes. The last layer—the subcuits—is a subcutaneous fat layer beneath the dermis. It supplies nutrients to the other two layers and insulates the body.

Human skin is steadily exposed to types of external factors (e.g., solutions, chemicals, and most critically UV-radiation). UV-radiation can lead to the induction of UV-specific mutations, which are known to be involved in the development of skin cancer. Skin cancer can emerge from keratinocytes [e.g., basal cell carcinoma (BCC) and squamous cell carcinoma (SCC)] as well as from melanocytes [e.g., malignant melanoma (MM)]. MM has a high tendency to metastasize and is the most deadly skin cancer (20-30% mortality). In 2012, more than 20k cases were newly diagnosed in Germany, constituting 4% of all new cases of cancer in that year [97]. Taken together BCC, SCC, and MM, skin cancer is one of the most frequent cancer in the white population worldwide. Although therapy of skin cancer (especially for MM) has been dramatically improved (e.g., immune checkpoint therapies), early detection of MM is still the most promising strategy because in the early growth phase (when the tumor is still thin and has not grown beyond the basal membrane), MM is nearly 100% curable just by excision of the tumor. MM can develop from benign nevi (pigmented lesions) or *de novo* in human skin. In the former case, early detection of cellular signs of a tumor in a nevus would be of great importance.

Accurate diagnosis of skin diseases relies on the pathohistological microscopic analysis of the skin biopsies, which normally involves removal of the suspected skin lesion, fixing, embedding, sectioning, staining, etc. Ideally, such highly invasive method should be avoided especially for early skin cancer diagnosis, which has stimulated tremendous research efforts on developing noninvasive virtual biopsy tools that can distinguish benign from malignant lesions. Common noninvasive optical techniques include optical coherence tomography [98, 99, 100], confocal microscopy [101, 102, 103, 104], and MPM [105].

As one of the most important label-free techniques to conduct optical virtual skin biopsy, MPM features submicron optical resolution, intercellular information, and intrinsic sectioning ability. Mainly depending on the interaction between ultrafast pulses and tissues, various mechanisms are available to visualize epidermis and upper dermis, e.g., 2PEF [106, 107, 108, 109, 110, 111, 112, 113], SHG [114, 115, 116, 117, 39, 118, 119], and THG [115, 116, 117, 118, 119]. Common 2PEF contrast agents in human skin rely on the molecular resonance of endogenous fluorophores, e.g., keratin, melanin, or reduced nicotinamide adenine dinucleotide (NADH) [106, 107, 108, 109, 110, 111, 112, 113]. In contrast, optical harmonics originates from tissue structures. Non-centrosymmetric fibrous tissue leads to SHG, which enables the visualization of collagen or elastin fibers [114, 115, 116, 117, 39, 118, 119]. Arising from interfaces and optical inhomogeneity, THG can reveal the cell outline and thus differentiates SC, SG, SS, and SB in epidermis [117, 118, 119]. These modalities are powerful tools of bio-imaging for histopathology, morphology, and disease diagnosis. For example, 2PEF microscopy can alone quantify tumor fluorescence of cancer tissue [120]. 2PEF combined with SHG imaging enables more studies on various issues, e.g., local invasion at tumor-stromal interface [121, 122], BCC [123, 124], orientation and polarization dependence of collagen fibers [125, 126, 127, 128], MM [129], and SCC [130]. THG can not only image tumors [131, 132], but also enable the measuring of nuclear-cytoplasmic (NC) ratio, serving as an index for scoring skin aging [133].

4.1.1 Driving source requirement for HGM

The selection of excitation wavelength is crucial while conducting MPM in the biological tissue because the optical attenuation is highly wavelength dependent. Illumination at the wavelength featuring lower attenuation allows the effective emission of the nonlinear signal without damaging the sample. For example, mainly caused by light scattering and water absorption, the curve of optical attenuation exhibits four transmission windows within the NIR region in favor of deep-tissue imaging in brain [26, 27]. The first transmission window is 650-950 nm, a wavelength range that can be covered by Ti:sapphire lasers. However, the corresponding THG (217-317 nm) falls within UV region and suffers from strong water/protein absorption, low objective transmittance, and low sensitivity of photomultiplier tube (PMT). Though the third transmission window (1600-1870 nm) supports 3PEF of RFP, it exhibits stronger water absorption compared with the second transmission window (1100-1350 nm), and gallium arsenide (GaAs) PMTs have lower sensitivity for the corresponding SHG (800-935 nm) [134]. The same issue is also confronted by the fourth transmission window centered at 2200 nm.

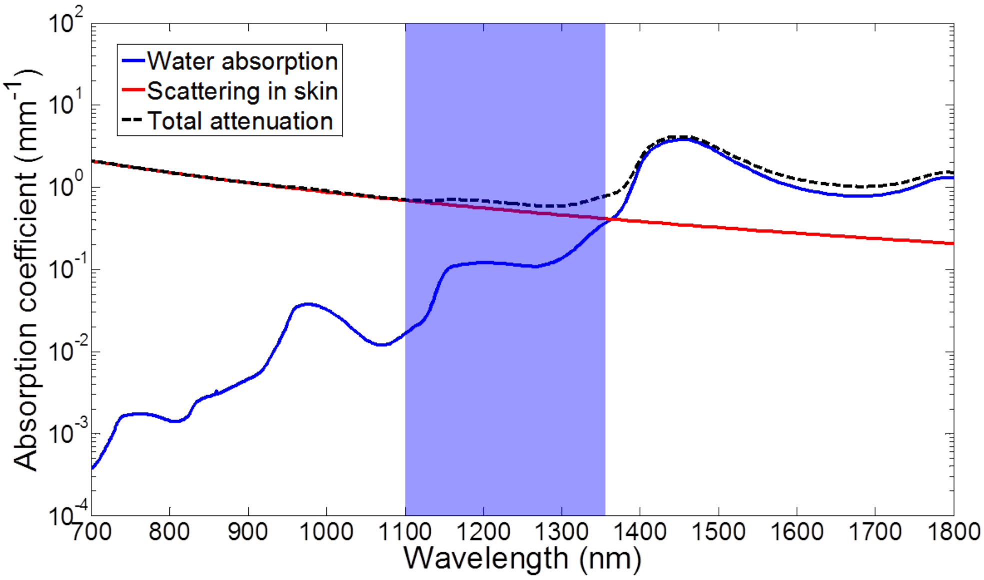

Figure 4.1: Optical attenuation and the second NIR transmission window in the skin tissue.

In Fig. 4.1 we plot the optical attenuation curve considering water absorption [135] and scattering in the skin tissue [136]. The curve has a similar transmission window in the range of 1100-1350 nm as in the brain tissue [26, 27]. Excitation within this wavelength range leads to several advantages for HGM (combining SHG and THG):

1. The excitation light experiences less overall optical attenuation considering both water absorption and light scattering in the tissue [96].
2. Compared with the window at 650-950 nm, the illumination tolerance is increased due to the reduced photon energy [137].
3. It provides better penetrability and benefits deep-tissue imaging.

4. Most of the resulting SHG and THG signals fall within the region of visible light, which can be efficiently detected by gallium arsenide phosphide (GaAsP) PMTs.

5. It allows resonant enhancement of THG from endogenous molecules (e.g., melanin [117, 118], hemoglobin [138], and lipid [139]).

Several ultrafast laser sources have been implemented to produce femtosecond pulses in this wavelength range to drive HGM. For example, passively mode-locked Cr:forsterite lasers can directly emit femtosecond pulses at ∼1250 nm [21, 140, 141, 38, 142]. Broadly tunable femtosecond pulses can be obtained from solid-state synchronously pumped OPOs [20, 143, 117, 144] or OPAs [30, 18, 19]. Despite their success, however, these solid-state lasers demand precise cavity-alignment and environmental control (i.e., water cooling, temperature and humidity feedback loop, vibration isolation etc.), which limits the use of HGM to specialized laboratories.

In contrast, fiber-based femtosecond sources based on ultrafast fiber lasers followed by fiber-optic nonlinear wavelength conversion offer a simple and robust solution as we reviewed in Sec. 1.3. Indeed, they have been demonstrated in the 1.15-1.35 μm wavelength range by several groups. Normally the driving sources are derived from EDFLs emitting 1.55-μm pulses, which can be converted to pulses at 1.2-1.3 μm via DW generation [45, 50, 145, 65, 52]. Due to the use of HNLFs, the 1.2-μm pulses delivers only 1.07-nJ pulse energy [50]. Another fiber-optic nonlinear wavelength conversion mechanism is SSFS, which can redshift the output pulse from YDFLs to the wavelength range of 1.15-1.35 μm [53, 46, 56, 57]. It is noteworthy that the resulting Raman soliton energy is limited by the soliton-area-theorem [67]. To increase the soliton pulse energy, HOM fibers are employed to excite SSFS [68, 69, 70, 71]. Another approach is to employ SSFS in LMA fibers pumped by an EDFL, which generates Raman soliton pulses beyond 2.3 μm followed by frequency doubling to 1.15-1.25 μm [65, 66]. However, strong absorption in fused silica beyond 2.3 μm prevents effective achieving femtosecond pulses with wavelength longer than 1.25 μm.

4.2 HGM driven by an EDFL-based SESS source

Besides the approaches mentioned above, wavelength widely tunable femtosecond pulses in this range can be generated by SESS [72, 73]. For example, SESS implemented in an LMA fiber pumped by a YDFL allows us to derive up to >20-nJ, ∼100-fs pulses tunable in the range of 1030-1215 nm [73]. In Sec. 3.2.2, we also applied SESS to a DSF pumped by an EDFL and obtained pulses tunable from 1.3 μm to 1.7 μm with >15-nJ pulse energy and ∼100-fs pulse duration at 1.3 μm. In this section, we improve the EDFL-based SESS source to obtain ∼10-nJ femtosecond pulses tunable between 1.15 μm and 1.35 μm. This source is then integrated with a scanning microscope for HGM imaging in human skin *ex vivo*.

4.2.1 Schematic setup

Figure 4.2 illustrates the schematic setup for HGM driven by an EDFL-based SESS source. The setup consists of an EDFL pump source, a nonlinear wavelength converter employing SESS, and a scanning microscope.

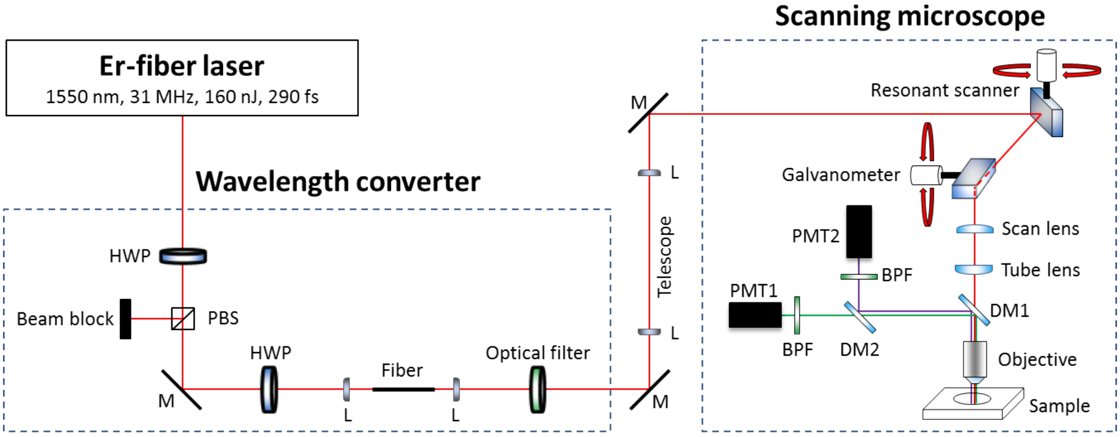

Figure 4.2: HGM driven by an EDFL-based SESS source.

The EDFL is the same one that we used in Sec. 2.3 and Sec. 3.2.2. It operates at 31-MHz repetition rate and produces 160-nJ, 290-fs pulses centered at 1550 nm. To implement SESS, we couple the 1550-nm pulses into 8.5-cm DSF. The coupling module is described in Sec. 2.3, and the DSF is longer than those used in Sec. 3.2.2 for more spectral broadening. We use a HWP and a PBS to vary the pulse energy coupled into the DSF. As the coupled pulse energy is increased from 75 nJ to 100 nJ, the peak wavelength of the leftmost spectral lobe of the broadened spectrum shifts from 1350 nm to 1150 nm. Then we use optical BPFs to select these spectral lobes for HGM.

The left column in Fig. 4.3 shows the spectra filtered by different BPFs with 50-nm bandwidth centered at 1.15 μm, 1.2 μm, 1.25 μm, 1.3 μm, and 1.35 μm, respectively. The resulting SESS tunable femtosecond source has an average power of 224-362 mW, corresponding to pulse energy of 7.2-11.7 nJ, which meets the requirement (>5 nJ before the microscope system) to achieve fine THG contrast [65]. After reaching the thermal equilibrium, the power fluctuation of the filtered spectral lobes from the tunable source between 1.15 μm and 1.35 μm is a couple of percent. Due to the transmittance loss of the microscope, the maximum available average power after the objective is 83-210 mW (parentheses in the left column of Fig. 4.3), corresponding to pulse energy of 2.7-6.8 nJ. The red curves in the right column of Fig. 4.3 show the autocorrelation traces measured after the objective. The FWHM duration of these traces is 142-168 fs. The pulse duration is estimated to be 92-109 fs, assuming a hyperbolic-secant pulse profile with a deconvolution factor of 1.54. The pulses are slightly chirped after passing through the microscope and the objective compared with the calculated transform-limited pulses allowed by the filtered spectra (black dashed curves in the right column of Fig. 4.3). The characterized average power and pulse duration measured at different wavelength after the objective are later used to calibrate the pulse peak power after the objective. It is noteworthy that we use the term "after the objective" instead of "at the sample surface." The objective is water immersive; however, the characterizations are carried out without water immersion.

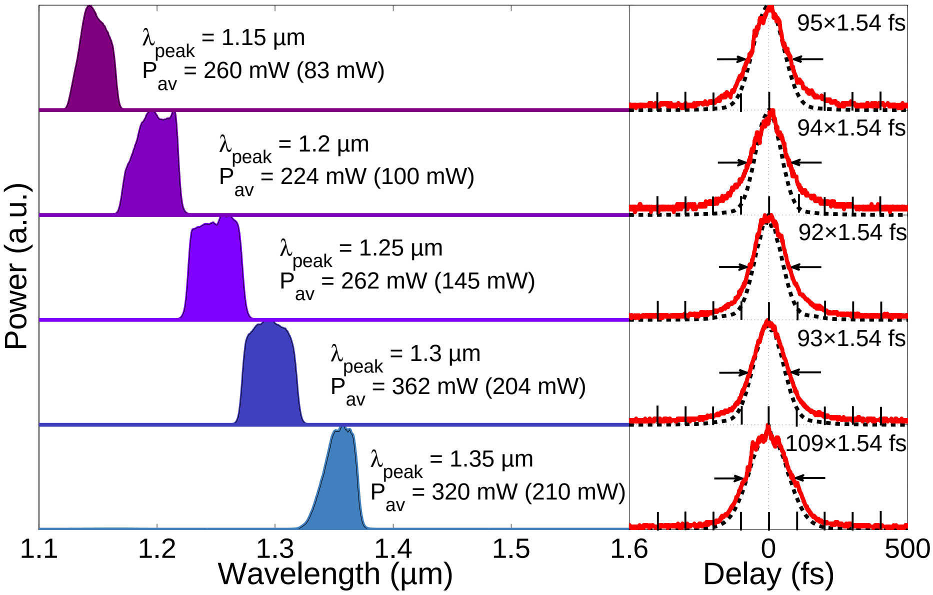

Figure 4.3: Fiber-based SESS source tunable between 1.15 μm and 1.35 μm.

We use a telescope before the excitation beam entering the scanning microscope (MPM-2PKIT, Thorlabs) to match the beam size to the objective (XLPLN25XWMP2, Olympus) clear aperture. The scanning microscope consists of a resonant scanner (8 kHz) and a mirror galvanometer (up to 30 Hz). The 25× water immersive objective has 1.05 NA and 2-mm working distance (WD). The emitted signal is epi-collected by the same objective and reflected by a dichroic mirror (DM1) (Di02-R1064-25 × 36, Semrock). DM2 with different edge wavelength (FF562-Di03-25 × 36 or Di02-R405-25 × 36, Semrock) further separates SHG and THG from different excitation. A motorized stage provides vertical movement with adjustable velocity to observe the sample at the different depth from the surface, which ensures that imaging can be continuously recorded.

Figure 4.4(a) depicts the cathode radiant sensitivity of the PMTs for signal detection, with the voltage-dependent gain shown in Fig. 4.4(b) [146]. For the excitation wavelength in 1.15-1.35 μm, we use PMT1 (H7422P-40, Hamamatsu) with the peak sensitivity at 580 nm [green curve in Fig. 4.4(a)] to detect the corresponding SHG (575-675 nm). The THG (383-450 nm) is detected by PMT2 (H10721-210, Hamamatsu) with the sensitivity peaking at 420 nm [magenta curve in Fig. 4.4(a)]. The control voltage is set between 0.5-0.7 V for linearly approximate small gain to avoid signal saturation. Signal photons are collected by PMTs and converted to electric signal, which is further amplified by transimpedance amplifier with 30200 V/A (TIA60, Thorlabs). A data acquisition card (PCIe-6321, National Instruments) acts as an analog-to-digital converter.

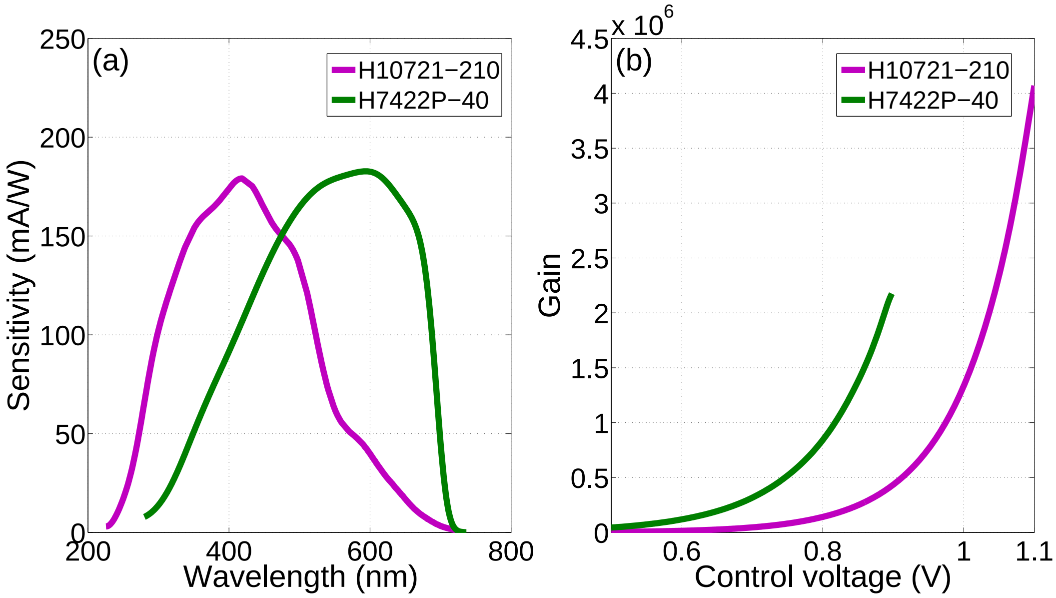

Figure 4.4: (a) Cathode radiant sensitivity and (b) gain of the PMTs.

4.2.2 SHG/THG imaging of human skin

We first demonstrate that the EDFL-based SESS source tuned to 1.25-μm is able to drive HGM imaging in human skin. Then we compare the imaging excited by different wavelength in the range of 1.15-1.35 μm. Figure 4.5 shows four representative HGM images of *ex vivo* human skin tissue from the back part. Each image has a field of view (FOV) of 270 μm × 270 μm. The excitation wavelength is tuned to 1.25 μm—the typical center wavelength of Cr:forsterite lasers. The excitation power after the objective is 50 mW, corresponding to 1.6-nJ pulse energy. The resulting SHG at 625 nm is colored in green, and the THG at 417 nm colored in magenta. We use the same pseudocolor for SHG and THG in the following of this chapter.

The THG signal exhibits a strong contrast from cells in epidermis [Fig. 4.5(a-c)]. Different stratums and cells in epidermis can be differentiated by the THG contrast. For example, SC can be easily recognized by its nucleiless feature, and granular cells have a relatively lower NC ratio compared with spinous cells and basal cells. At 20-μm depth, SC and SG can be simultaneously observed shown in Fig. 4.5(a). At 39-μm depth, the major cells are spinous and basal cells [Fig. 4.5(b)]. SHG originating from collagen fibers starts to appear as the imaging depth increase to 62 μm. These fibers are surrounded by basal cells, showing the uneven region of dermal papilla (DP) at the edge between epidermis and dermis [Fig. 4.5(c)]. For the imaging depth increased to 113 μm, THG signal vanishes and is replaced by SHG from abundant collagen fibers in dermis [Fig. 4.5(d)].

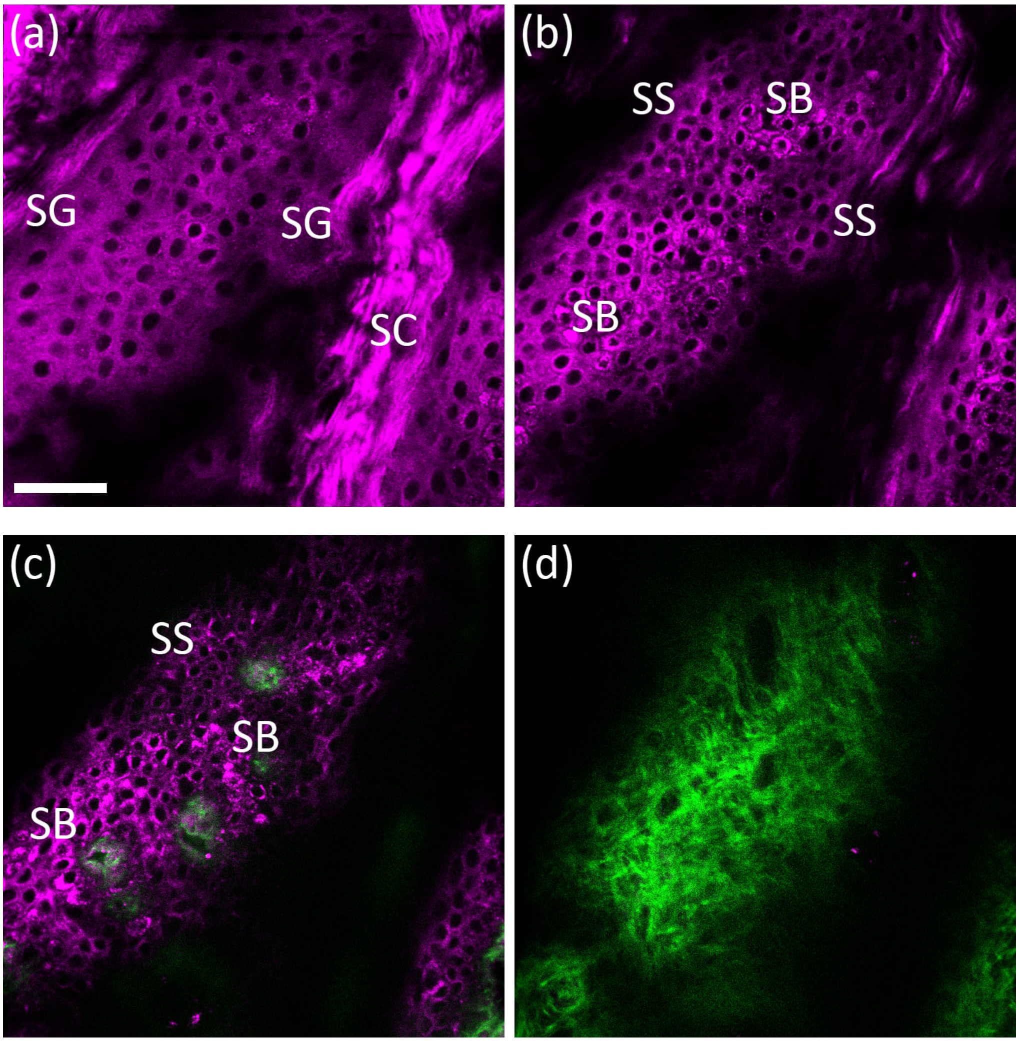

Figure 4.5: HGM imaging of *ex vivo* human skin from the back part at different penetration depth excited by 1.25-μm femtosecond pulses. Scale bar: 50 μm.

Figure 4.6 shows the HGM imaging (FOV: 270 μm × 270 μm) similar to Fig. 4.5, but the skin sample is from the inguinal part. The excitation power after the objective is also 50 mW. Both the red blood cells and lipids can be observed in the capillaries surrounded by collagen fibers [Fig. 4.6(c) and 4.6(d)]. They can be easily distinguished by the size.

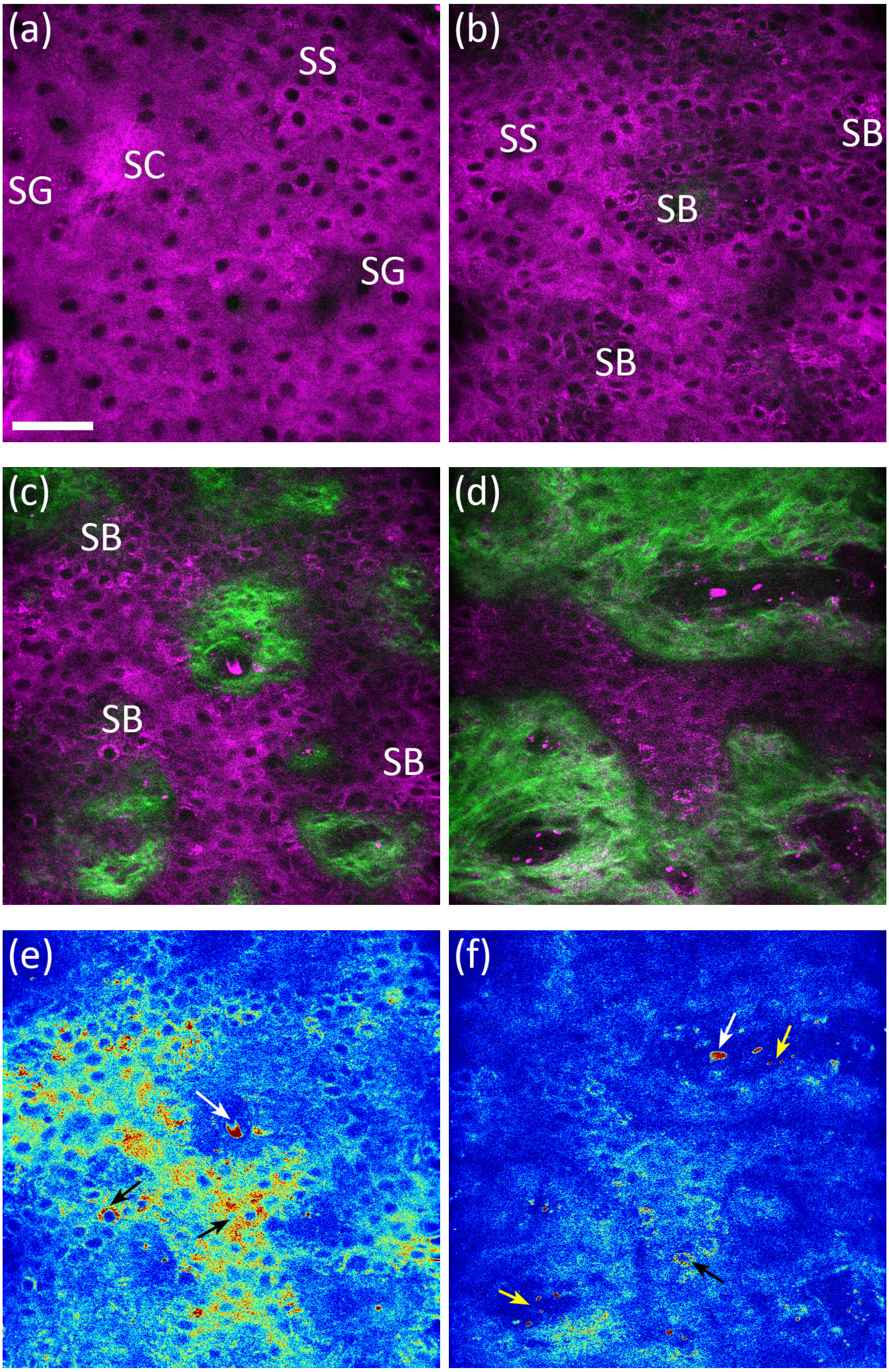

Figure 4.6: HGM imaging of *ex vivo* human skin from the inguinal part at different penetration depth excited by 1.25-μm femtosecond pulses. Scale bar: 50 μm.

THG signals are also related to the endogenous molecules (e.g., melanin [117, 118], hemoglobin [138], and lipid [139]), and can be resonantly enhanced by excitation in the 1.15-1.35 μm wavelength range. To emphasize the molecule-induced resonance enhancement, we reserve only the THG contrast in Fig. 4.6(e) and 4.6(f), and change the colormap from "magenta" to "Jet." Consequently, the melanin-induced resonant enhancement in SB can be used to distinguish melanocytes from keratinocytes by the THG contrast. Strong THG colored in red indicates the melanocytes and melanin distribution among the surrounding keratinocytes indicated by black arrows in Fig. 4.6(e) and 4.6(f), as well as red blood cells (white arrows) and lipids (yellow arrows).

The HGM imaging excited by 1.25-μm EDFL-based SESS source shows similar penetrability and subcellular resolution to differentiate cells and tissues in human skin, comparable to those achieved from Cr:forsterite lasers [117, 118].

4.3 Effect of excitation wavelength on HGM

Excitation wavelength selection is an important issue while conducting MPM in biological tissues, since the emitted nonlinear signal is highly dependent on and sensitive to the peak intensity of the pulse. Excitation at wavelength suffered from strong optical attenuation can not generate the signal efficiently, and also increase the risk of damaging the sample. Unlike MPEF, the excitation wavelength of HGM is not limited to certain absorption bands of fluorophores, so one can choose the desired excitation wavelength at will to avoid strong optical attenuation, which also lowers the risk of photodamage.

To compare the performance of different excitation wavelengths, we observed the skin sample irradiated by 5 different wavelengths peaking at 1.15 μm, 1.2 μm, 1.25 μm, 1.3 μm, and 1.35 μm. The region of interest (ROI) is scanned back and forth within the penetration depth up to 300 μm. Considering both the microscope transmittance and the pulse duration, we use a neutral density wheel to adjust the illumination power at these wavelengths to maintain the same pulse peak power after the objective. The excitation power of 1.15-μm, 1.2-μm, 1.25-μm, and 1.3-μm pulses is 60 mW after the objective. For 1.35-μm pulses, the applied power is 70 mW.

Figure 4.7 shows the HGM imaging (FOV: 500 μm × 500 μm) of *ex vivo* human skin from the back part excited by different wavelengths at four representative penetration depths. Figure 4.7(a-e) shows the SS and SB at 50-μm depth in epidermis, Fig. 4.7(f-j) the collagen fibers at 90-μm depth, Fig. 4.7(k-o) the collagen fibers and arrector pili muscles at 120-μm depth, and Fig. 4.7(p-t) the arrector pili muscles at 170-μm depth. The images at the same penetration depth are presented in the sequence starting from the shorter excitation wavelength, namely: 1.15 μm, 1.2 μm, 1.25 μm, 1.3 μm, and 1.35 μm.

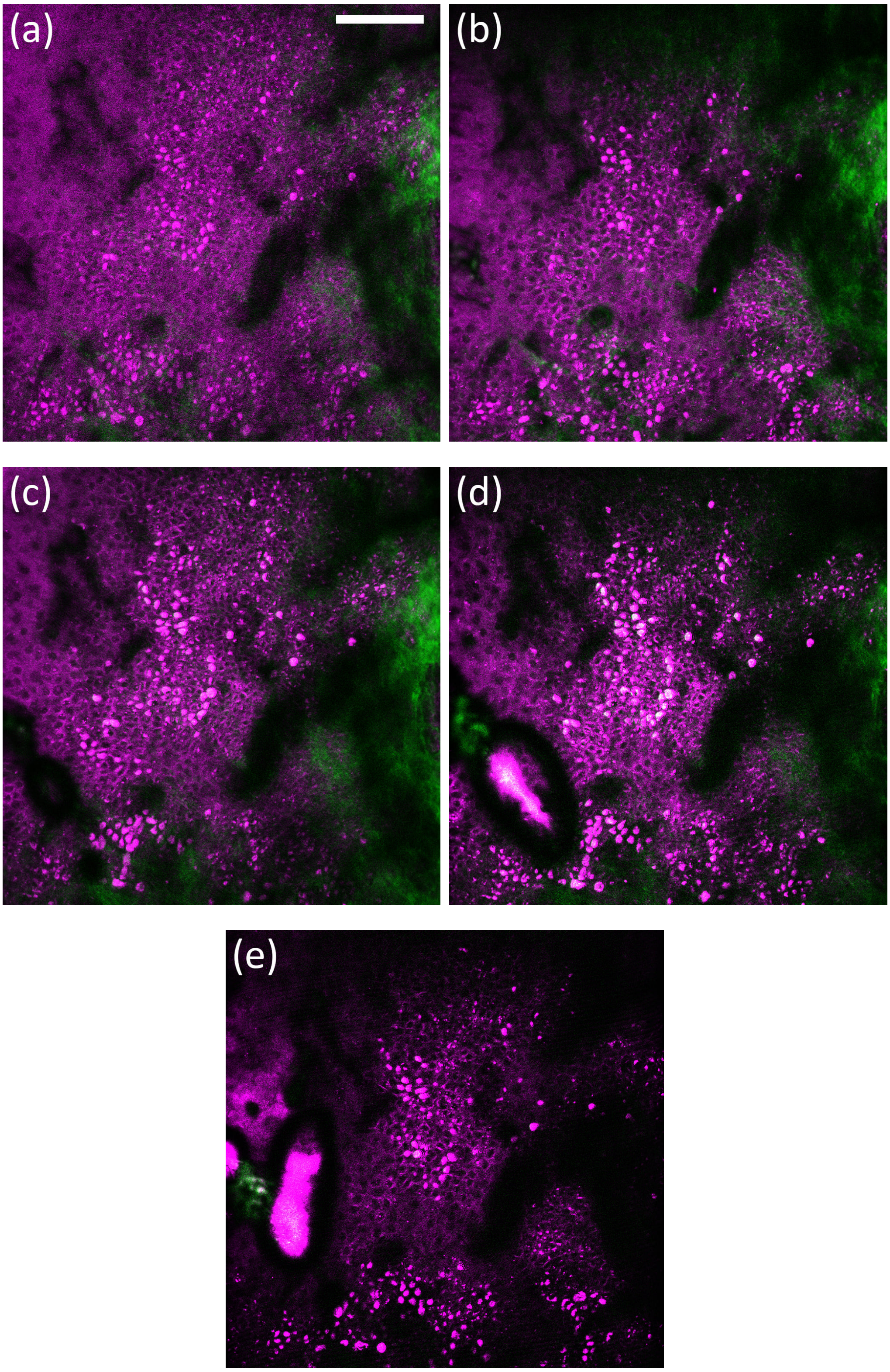

Figure 4.7: HGM imaging of *ex vivo* human skin from the back part excited by 5 different wavelengths at 50-μm depth. Scale bar: 100 μm.

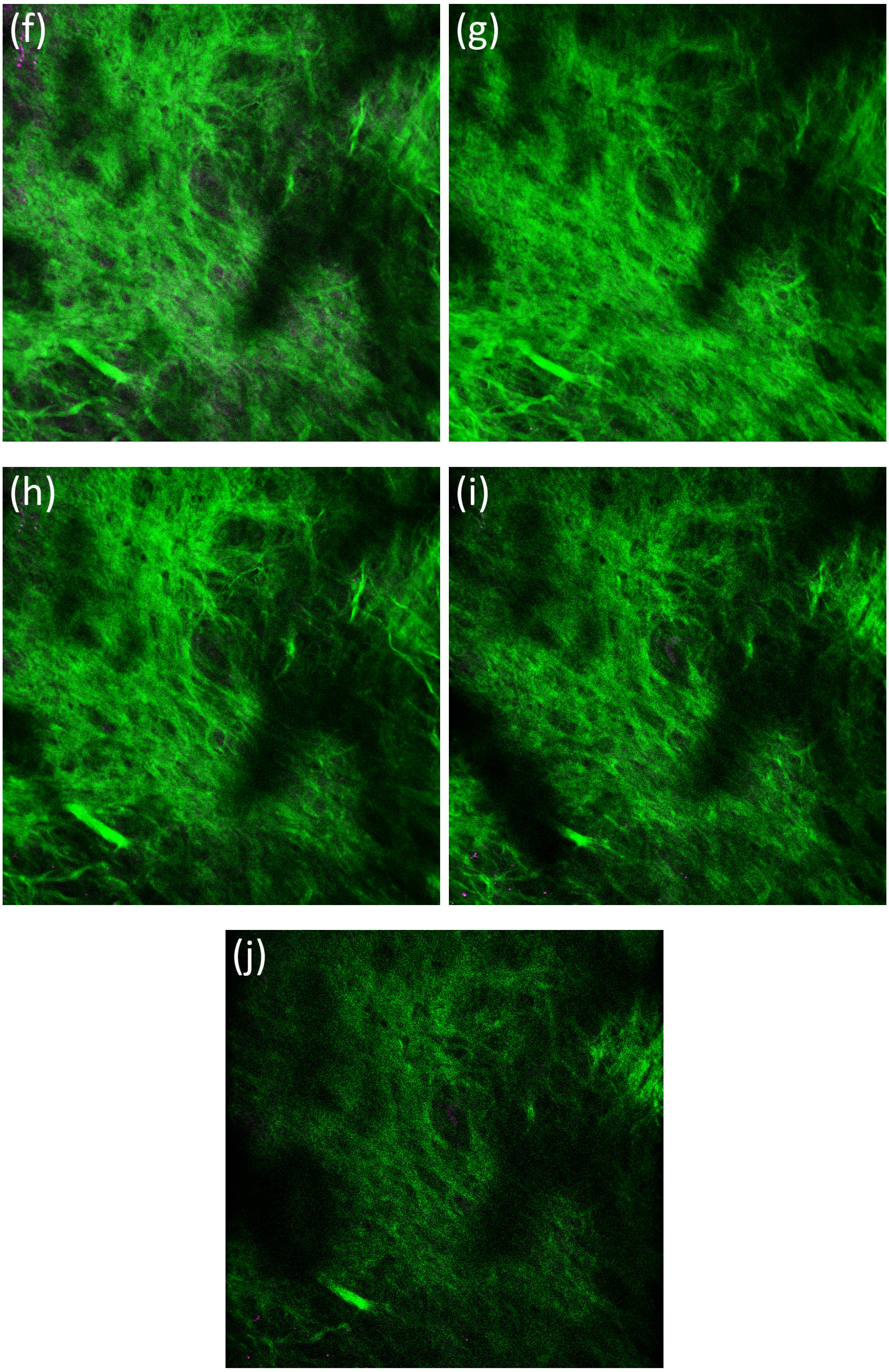

Figure 4.7: HGM imaging of *ex vivo* human skin from the back part excited by 5 different wavelengths at 90-μm depth.

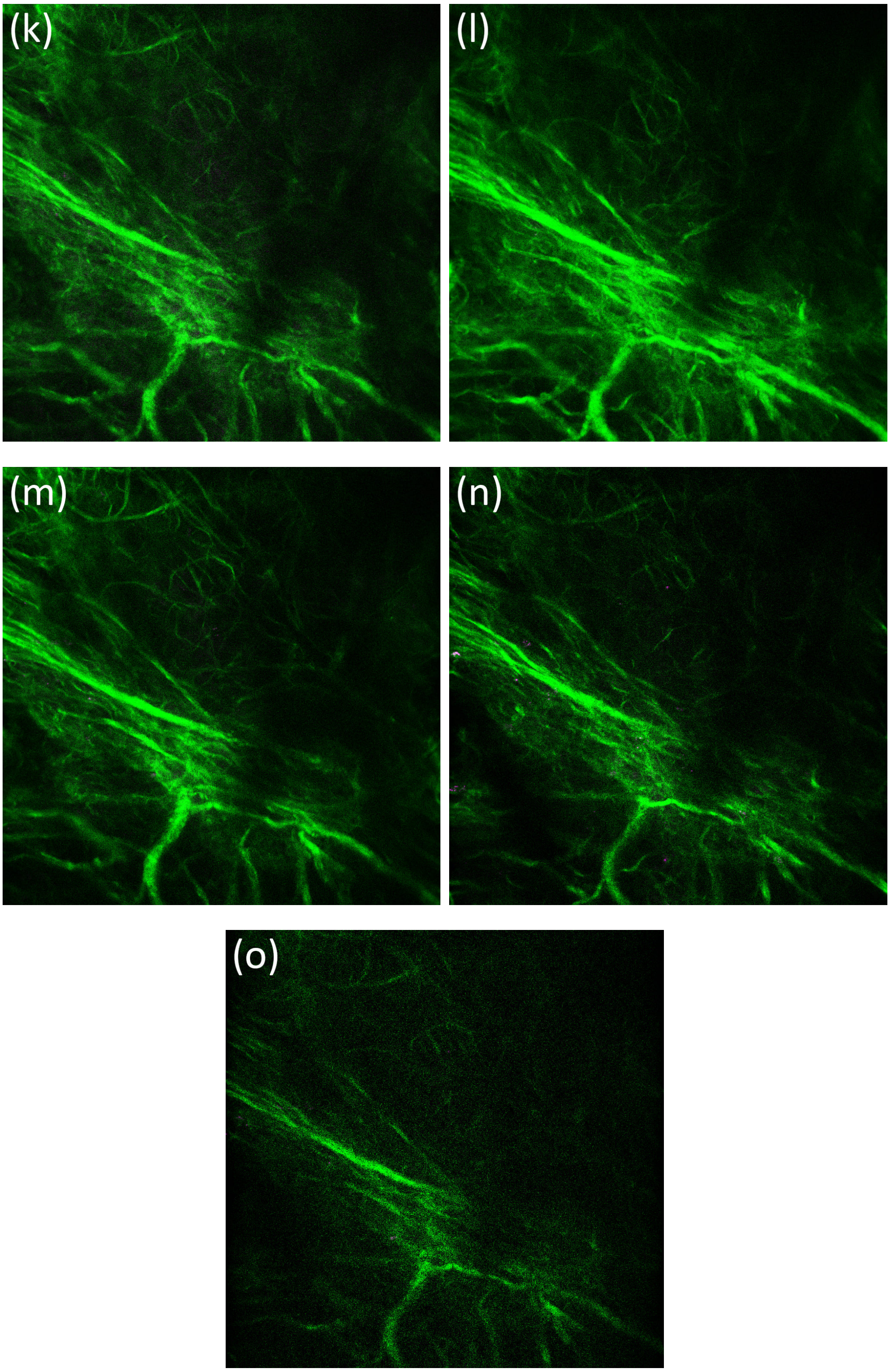

Figure 4.7: HGM imaging of *ex vivo* human skin from the back part excited by 5 different wavelengths at 120-μm depth.

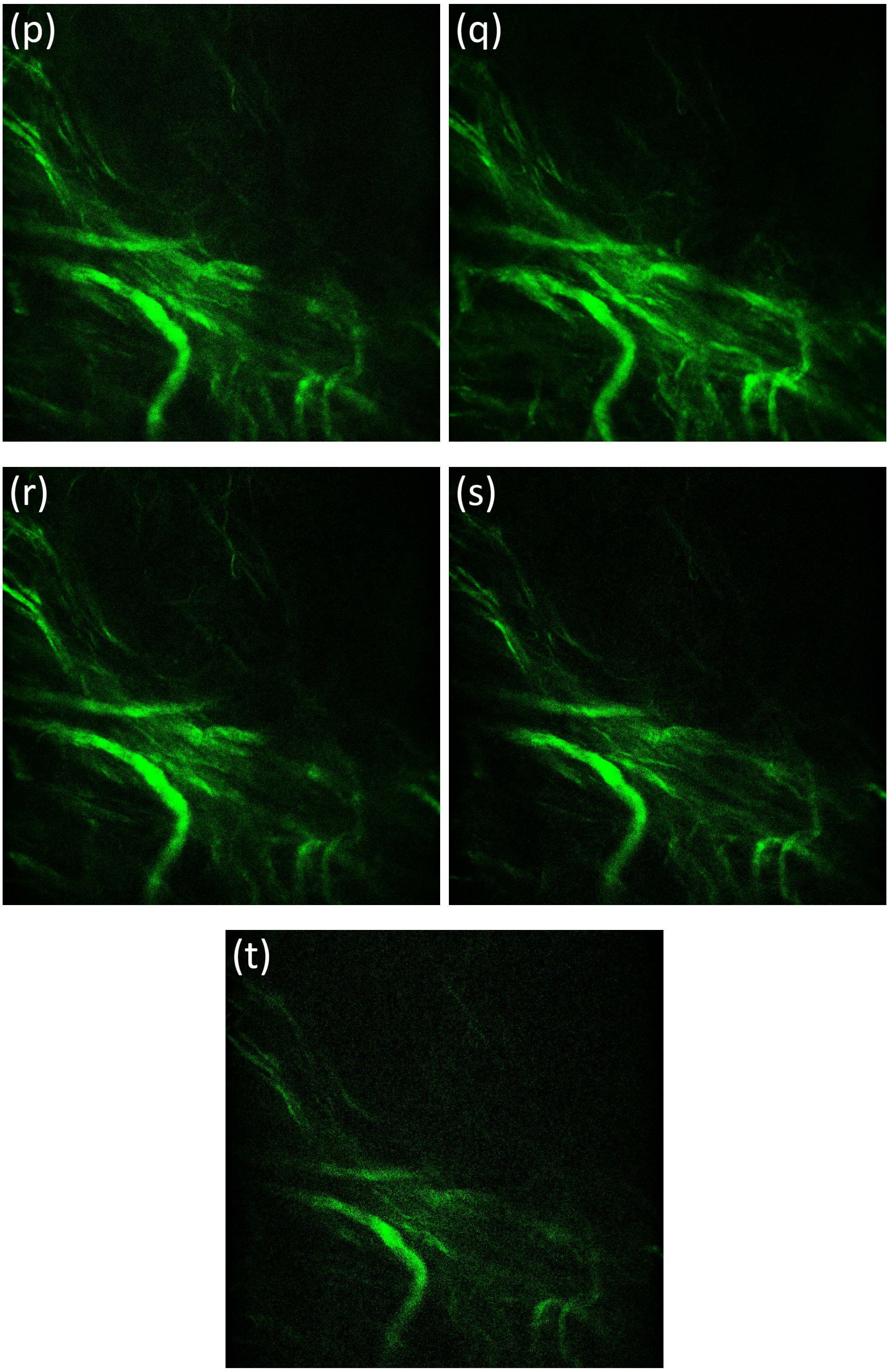

Figure 4.7: HGM imaging of *ex vivo* human skin from the back part excited by 5 different wavelengths at 170-μm depth.

At first glance, the resulting HGM images excited by different wavelengths seem similar. However, the image details reveal significant difference. Besides the strong THG contrast from epidermal cells in Fig. 4.7(a-e) as predicted, air bubbles appear at the lower left corner of Fig. 4.7(d) and 4.7(e) for 1.3-μm and 1.35-μm excitation, indicating strong water absorption as the excitation wavelength becomes close to a local peak absorption at 1.45 μm [135]. We attribute the generation of air bubbles to water vaporization at the local volume. Since the refractive index difference between air and water or air and skin is larger [147], the air-water or air-skin interface can result in strong THG, and thus suppresses the THG contrast of the cells. These air bubbles also degrade the NA of the water immersive objective in the local area, resulting in weak SHG in deeper layers [Fig. 4.7(i) and 4.7(j)], compared with Fig. 4.7(f-h). Although the outline of the thick arrector pili muscles is still clear in Fig. 4.7(n) and Fig. 4.7(o), the contrast is worsened especially compared with Fig. 4.7(k-m). In addition, the fine structure of collagen fibers excited by 1.35-μm femtosecond pulses [Fig. 4.7(j)] is apparently vaguer than others achieved by pulses of shorter excitation wavelength.

To quantify the effect of excitation wavelength, we plot the signal intensity distribution along the penetration depth in Fig. 4.8. The signal intensity is defined as the pixel intensity summation of the image at each depth. Although the intensity peak of THG [Fig. 4.8(a)]/SHG [Fig. 4.8(b)] excited by different wavelength is all at 20-μm/90-μm depth, their relative intensities are substantially different. The signal intensity is much lower for those excited by 1.3-μm and 1.35-μm femtosecond pulses caused by the increased water absorption. Besides the conventional 1.25-μm excitation (which is traditionally offered by Cr:forsterite lasers or OPOs), 1.15-μm and 1.2-μm excitations enable similar imaging quality given the same peak power after the objective.

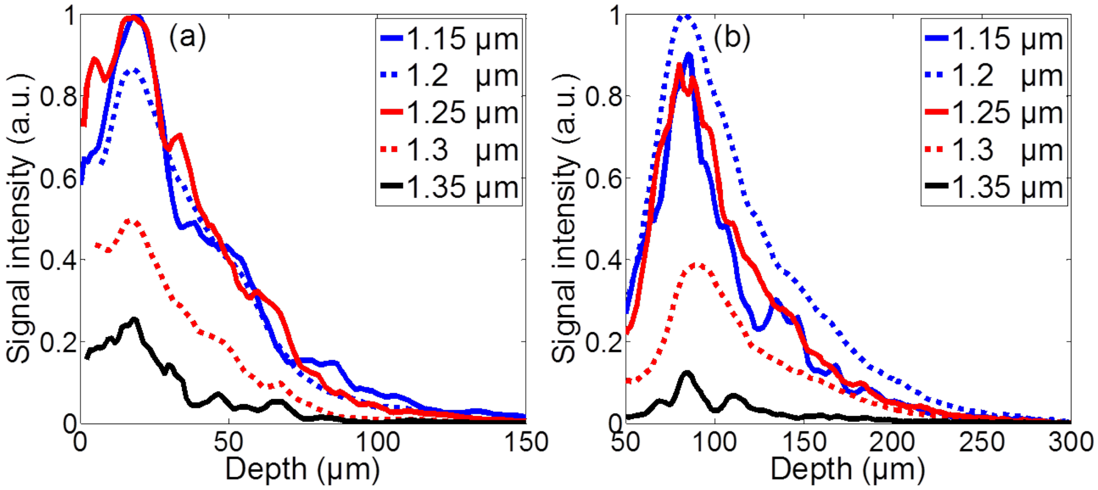

Figure 4.8: Signal intensity distribution along the penetration depth depending on different excitation. (a) THG. (b) SHG.

Indeed, femtosecond pulses in the range of 1.15-1.25 μm can be also generated by a YDFL-based SESS source [72, 73]. However, optical fibers usually exhibit higher positive GVD at this pump wavelength (∼1 μm), which leads to stretched pulses and reduced spectral broadening. Additionally, the self-focusing threshold is ∼4 MW at the YDFL wavelength (∼9 MW for EDFLs) [148]. Therefore SESS based on EDFLs exhibit better energy scalability.

A local minimum of water absorption around 1.1 μm is also attractive to HGM. However, shorter wavelength signifies higher photon energy and increases the risk of photodamage. For long-term observation, power tolerance study (e.g., experimental investigation in [149, 137]) is inevitable. Another issue is whether the resulting THG signal in the UV range is harmful to cell or not. UVA (320-400 nm) accounts for 95% of the UV radiation reaching the Earth surface. It has higher penetrability than UVB (290-320 nm). Although UVA does not directly harm the skin surface, it may damage keratinocytes and contribute to the initiation of skin cancer development [150].

In our current implementation, femtosecond pulses in the range of 1.15-1.35 μm are obtained by optically filtering the leftmost spectral lobe of an SPM-broadened spectrum. If the rightmost spectral lobe is selected by suitable BPFs, we can obtain femtosecond pulses tunable between 1.6 μm and 1.7 μm, which falls into another transmission window for bio-imaging (1.6-1.87 μm). However, excitation for HGM in this wavelength range exhibits stronger water absorption, and gallium arsenide PMTs have lower sensitivity to the corresponding SHG signal (800-935 nm) [134].

4.4 Conclusion of Chapter 4

In this chapter, we demonstrate a HGM microscope driven by an EDFL-based SESS source for optical virtual skin biopsy. Employing SESS in 8.5-cm DSF pumped by an EDFL results in spectrum continuously tunable between 1.15 μm and 1.35 μm—covering one of the most important transmission windows for bio-imaging—with up to >10-nJ pulse energy and ∼100-fs pulse duration.

The HGM imaging can differentiate stratums (e.g., SC, SG, SS, and SB) and tissues (e.g., DP and collagen fibers) in epidermis and upper dermis of human skin. We also compare the HGM imaging of human skin tissue *ex vivo* by different excitation in the range of 1.15-1.35 μm with the same pulse peak power after the objective. Besides 1.25 μm (typical center wavelength of Cr:forsterite lasers), our result suggests a ∼100-nm wide sub-window between 1.15 μm and 1.25 μm also suitable for conducting HGM in human skin.

Chapter 5

Multimodal MPM platform enabled by a two-color ultrafast source

In this chapter, we demonstrate an EDFL-based two-color ultrafast source to drive multimodal MPM. Besides wavelength tunable femtosecond pulses in 1150-1350 nm for HGM, frequency doubling of the EDFL output leads to pulses at the conventional Ti:sapphire laser wavelength, which covers the 2PA band of many important fluorophores. This versatile two-color femtosecond source constitutes an ideal solution to many applications, e.g., multimodal label-free skin imaging and protein crystal detection.

5.1 Multi-color ultrafast source for MPM

In general, a single-color ultrafast source allows one to drive either 2PEF/SHG or SHG/THG modalities at the same time. For example, ultrafast Ti:sapphire lasers generating pulses between 700 nm and 900 nm are commonly implemented to excite 2PEF of intrinsic chromophores, such as keratin, melanin, NADH, retinol, folic acid, and lipofuscin [106, 33, 34, 107, 108, 109, 110, 111, 112, 113]. Excitation within this wavelength regime (700-900 nm), the accompanying SHG (350-450 nm) serves as another modality to visualize collagen and elastin fibers with non-centrosymmetric structures. However, the corresponding THG (233-300 nm) is ultraviolet, which suffers from strong optical attenuation and lacks for high-sensitivity detectors. Although ultrafast pulses at the wavelength range of 1150-1350 nm are ideal source to drive HGM (including both SHG and THG modalities), they are not suitable for 2PEF of most common intrinsic fluorescent emitters.

Apparently, a two-color ultrafast source that can provide femtosecond pulses in both the wavelength range of 1150-1350 nm and 700-900 nm is required to implement multimodal MPM that incorporates 2PEF, SHG, and THG. In principle, a Ti:sapphire laser plus an OPO can meet such wavelength requirements. In this scenario, a small portion of the Ti:sapphire laser output is employed to drive 2PEF imaging and the rest of the output pumps the OPO to provide femtosecond pulses at longer wavelength for driving SHG and THG microscopy. This type of two-color sources has been applied to implement multimodal MPM platforms for imaging different biological samples, e.g., mouse liver tissues [117], human cornea [151], mouse brain tissues [152], and mouse skin [153].

In this Chapter, we develop an EDFL-based two-color ultrafast source. In Sec. 4.2.1 we have demonstrated that femtosecond pulses in 1150-1350 nm are achievable by an EDFL-based SESS source. To generate pulses at the Ti:sapphire laser wavelength, we employ frequency doubling in nonlinear materials [2]. When applied to femtosecond pulses generated by EDFLs (center wavelength in 1530-1610 nm [40]), the resulting SHG pulses fall in the range of 760-805 nm, constituting a substitute of Ti:sapphire lasers [154, 155, 63, 156, 157].

5.1.1 EDFL-based two-color ultrafast source

Figure 5.1 illustrates our multimodal MPM platform. Compared with the setup depicted in Sec. 4.2.1, we integrate another nonlinear wavelength converter—frequency doubling in a magnesium-doped periodically poled lithium niobate (MgO:PPLN) crystal—and an additional PMT for 2PEF detection. The system now consists of an EDFL pump source, two nonlinear wavelength converters (i.e., frequency doubling and SESS), and a scanning microscope. A HWP and a PBS split the EDFL output into two beams to obtain two-color pulses via nonlinear wavelength conversion.

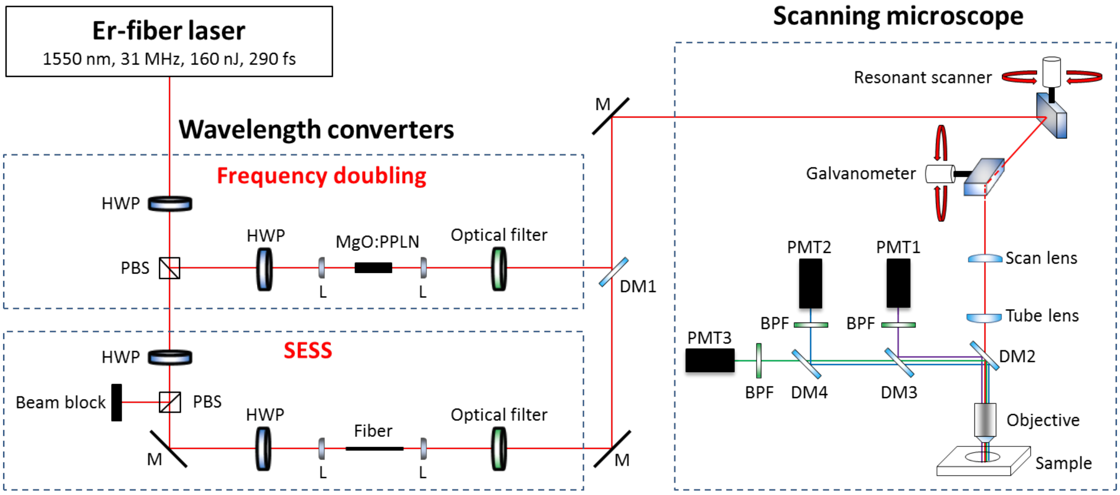

Figure 5.1: Schematic setup of the multimodal microscope driven by an EDFL-based two-color source.

We use a 0.3-mm long MgO:PPLN crystal (MSHG1550-0.5-0.3, Covesion) for frequency doubling. Figure 5.2(a) shows the spectrum of the EDFL. The frequency-doubled pulses are centered at 775 nm [inset of Fig. 5.2(b)] with 208-mW average power (6.7-nJ pulse energy). Given 760-mW input power, the frequency doubling has a conversion efficiency of 27%, which can be further improved by using longer crystals at the expense of phase-matching bandwidth. The measured FWHM duration is 292 fs [red curve in Fig. 5.2(b)], and the pulse duration is estimated to be 190 fs assuming a hyperbolic-secant pulse with a deconvolution factor of 1.54.

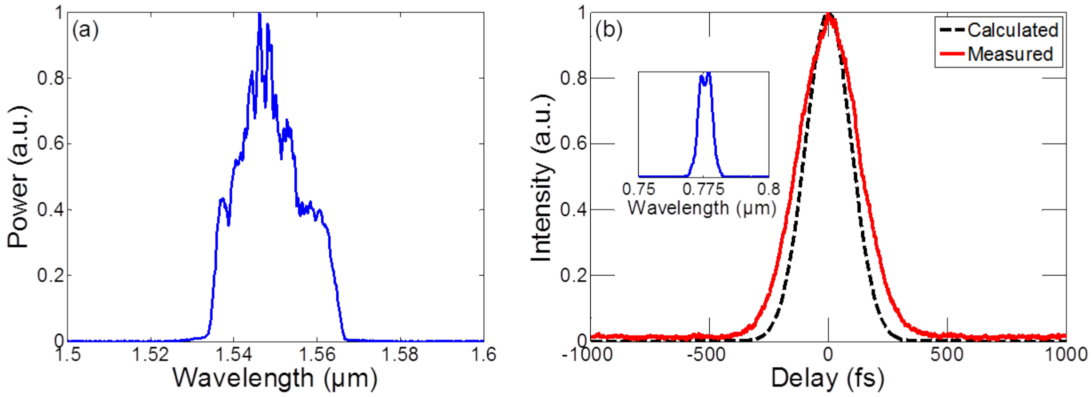

Figure 5.2: (a) Filtered spectrum centered at 775 nm. (b) Autocorrelation traces calculated from the transform-limited pulses allowed by the filtered spectrum (black dashed curve) and measured after the MgO:PPLN crystal (red curve).

To generate pulses at 1250 nm for SHG/THG microscopy, we employ SESS in 9-cm DSF that has been used in Sec. 2.3, Sec. 3.2.2 and Sec. 4.2.1. Figure 5.3(a) shows the broadened spectrum that spans more than 500 nm for 85-nJ pulses coupled into the DSF. The spectral lobe at 1150 nm can be attributed to optical wave breaking [158]. We use a 1300-nm SPF (#89-676, Edmund Optics) and a 1200-nm LPF (#89-662, Edmund Optics) to select the spectral lobe peaking at 1250 nm [inset of Fig. 5.3(b)]. The filtered power amounts to 365 mW, corresponding to 11.7-nJ pulse energy and a conversion efficiency of 14%. The red curve in Fig. 5.3(b) shows the measured intensity autocorrelation trace of the filtered pulses at 1250 nm. The FWHM duration is 72 fs, thus the pulse duration is estimated to be 47 fs assuming a hyperbolic-secant pulse with a deconvolution factor of 1.54. Also plotted in the same figure is the calculated autocorrelation trace (black dashed curve) of the transform-limited pulse allowed by the filtered spectrum. The transform-limited pulse has a duration of 41 fs, showing that the filtered pulses are nearly transform-limited.

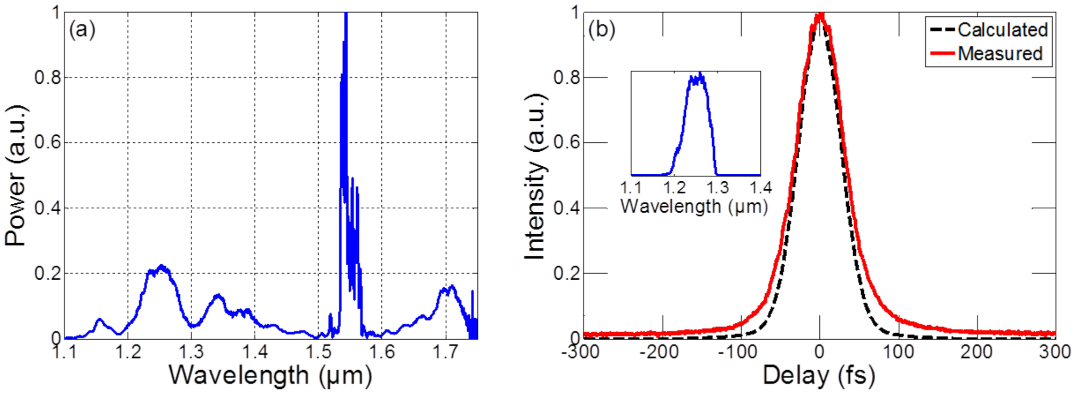

Figure 5.3: (a) Spectral broadening from 9-cm DSF. (b) Measured autocorrelation trace of the filtered pulses at 1250 nm (red curve) and calculated autocorrelation trace of the transform-limited pulse allowed by the filtered spectrum (black dashed curve). Inset: filtered spectrum centered at 1250 nm.

These two beams are combined by DM1 (Di02-R1064-25×36, Semrock) as the excitation before entering the scanning microscope (MPM-2PKIT, Thorlabs). The 25× objective (XLPLN25XWMP2, Olympus) is water immersive with 1.05 NA and 2-mm WD. The transmittance is >70% at 1250 nm and >80% between 400 nm and 1000 nm. The emitted signal is epi-collected by the same objective and reflected by DM2 (FF665-Di02-25×36, Semrock). Table 5.1 shows the two-photon excitation and emission peak wavelengths of common endogenous chromophores [105]. The emission peak ranges from 420 nm to 575 nm. As a result, we can use DM3 (FF435-Di01-25×36, Semrock) and DM4 (FF562-Di03-25×36, Semrock) to separate the resulting SHG, THG, and most of the 2PEF into three PMTs. SHG and 2PEF are detected by two identical PMTs (H7422P-40, Hamamatsu), and THG by a different PMT (H10721-210, Hamamatsu). The sensitivity of these two kinds of PMT peaks at 580 nm and 420 nm, respectively. Their cathode radiant sensitivity and voltage-dependent gain are shown in Fig. 4.4.

Table 5.1: Two-photon excitation and emission of common endogenous chromophores.

Chromophore	Excitation wavelength (nm)	Emission wavelength (nm)
Retinol	700-830	450
NADH	690-730	450-470
Vitamin D	<700	450
Flavins	700-730	430
Melanin	720-860	450, 520, 575
Keratin	720-780	480-500
Elastin	700-740	420-460
Collagen	700-740	420-460
FAD	800-850	535

5.2 Multimodal label-free skin biopsy

In this section, we demonstrate multimodal label-free MPM imaging in human skin enabled by an EDFL-based two-color source, which generates energetic femtosecond pulses at 775 nm and 1250 nm. Thus we are able to conduct SHG/THG microscopy excited by 1250-nm femtosecond pulses and 2PEF microscopy excited by 775-nm femtosecond pulses, simultaneously. During the experiment we use two *ex vivo* human skin tissues: the trunk part is shown in Fig. 5.4 and the head part shown in Fig. 5.5 and Fig. 5.6. A comparison between THG and 2PEF imaging in epidermis shows that both these two modalities can reveal different stratums. We use the following pseudo-colors to present the imaging results in this section: SHG is colored in red hot, THG in cyan hot, and 2PEF in yellow hot.

Figure 5.4 shows the SHG/THG imaging of human skin in epidermis from the trunk part excited by 1250-nm femtosecond pulses *ex vivo*. The maximum excitation power after the objective is 80 mW, corresponding to ~2.6-nJ pulse energy. The FOV is 270 μm × 270 μm. As we increase the imaging depth, different stratums in epidermis can be visualized. The imaging results in Fig. 5.4(a) obtained at 25-µm depth indicate three different structures close to the skin surface: SC, stratum lucidum (SL), and SG. SC can be found at the top left, middle left, and right of Fig. 5.4(a), while SL is at the top of Fig. 5.4(a). SL is a thin stratum composed of only a few (3-5) layers of keratinocytes, and another thin structure is SG. Their cells look flat and have the lowest NC ratio in epidermis. SC and SL are both nucleiless, but SC is much thicker than SL. At 30-µm depth, SC can still be found at the top left corner, while SL vanishes, and the main structures here are SG and SS [Fig. 5.4(b)]. Spinous cells can be commonly found in epidermis [Fig. 5.4(b-f)]. Collagen fibers revealed by SHG start to appear as the imaging depth reaches 55 µm [Fig. 5.4(d)]. The fibrous structure surrounded by basal cells is DP, which is located at the junction of epidermis and dermis [Fig. 5.4(d-f)].

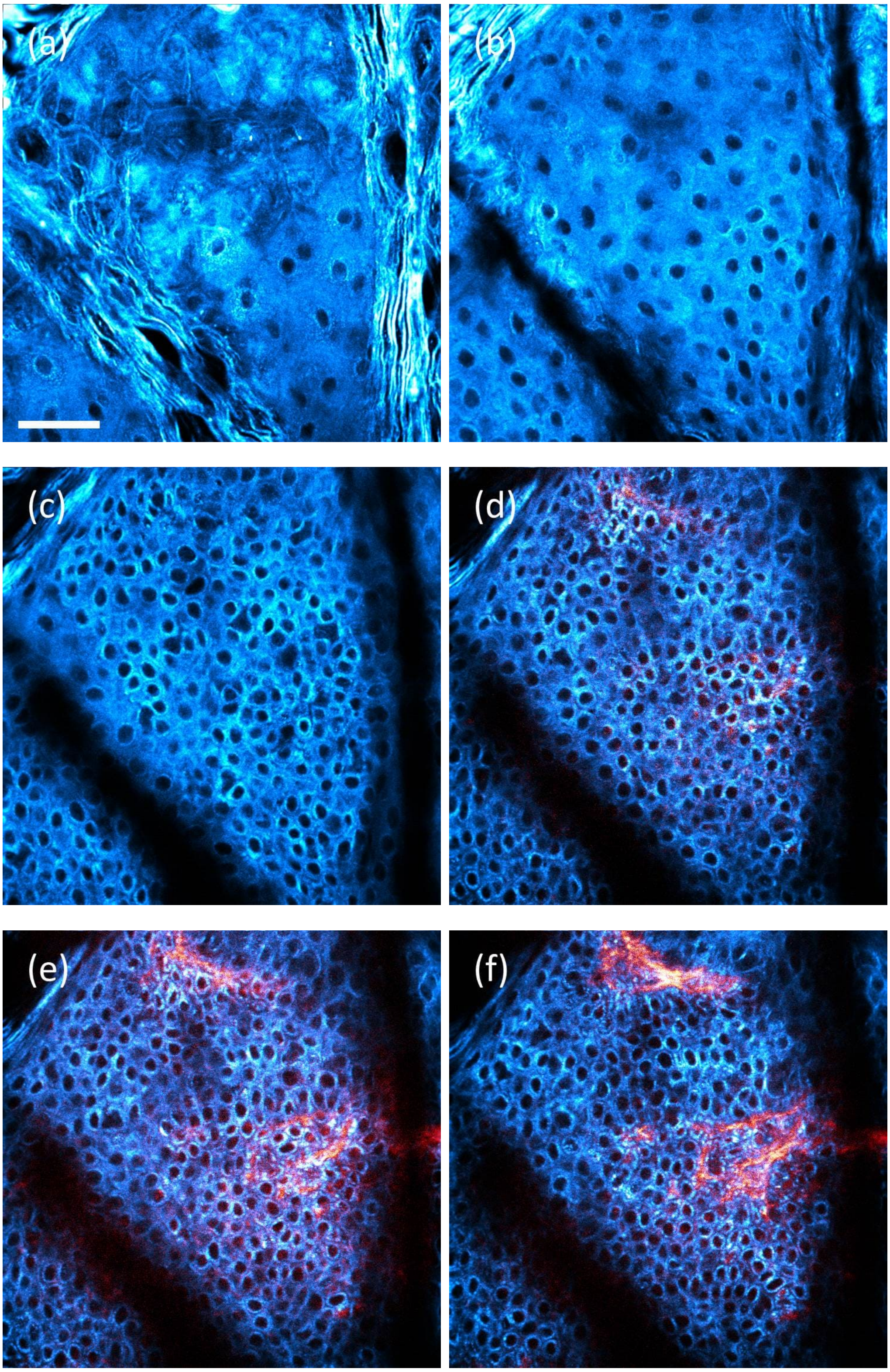

Figure 5.4: SHG/THG imaging of *ex vivo* human skin from the trunk part excited by 1250-nm femtosecond pulses at different penetration depth. (a) 25 μm. (b) 30 μm. (c) 45 μm. (d) 55 μm. (e) 60 μm. (f) 65 μm. Scale bar: 50 μm.

Fibroblasts that support epidermis are the main components in dermis. The fiber network mainly consists of collagen and elastin. Figure 5.5 shows the SHG imaging revealing this structure beneath epidermis in human skin from the head part *ex vivo*. The excitation power after the objective is also 80 mW, corresponding to ~2.6-nJ pulse energy. The FOV is 500 μm × 500 μm. The fiber network gradually changes along the imaging depth from 130 μm to 170 μm. It features fine and curvy fibers at 130-µm depth [Fig. 5.5(a)], in comparison with the thick straight ones at 170-µm depth [Fig. 5.5(c)].

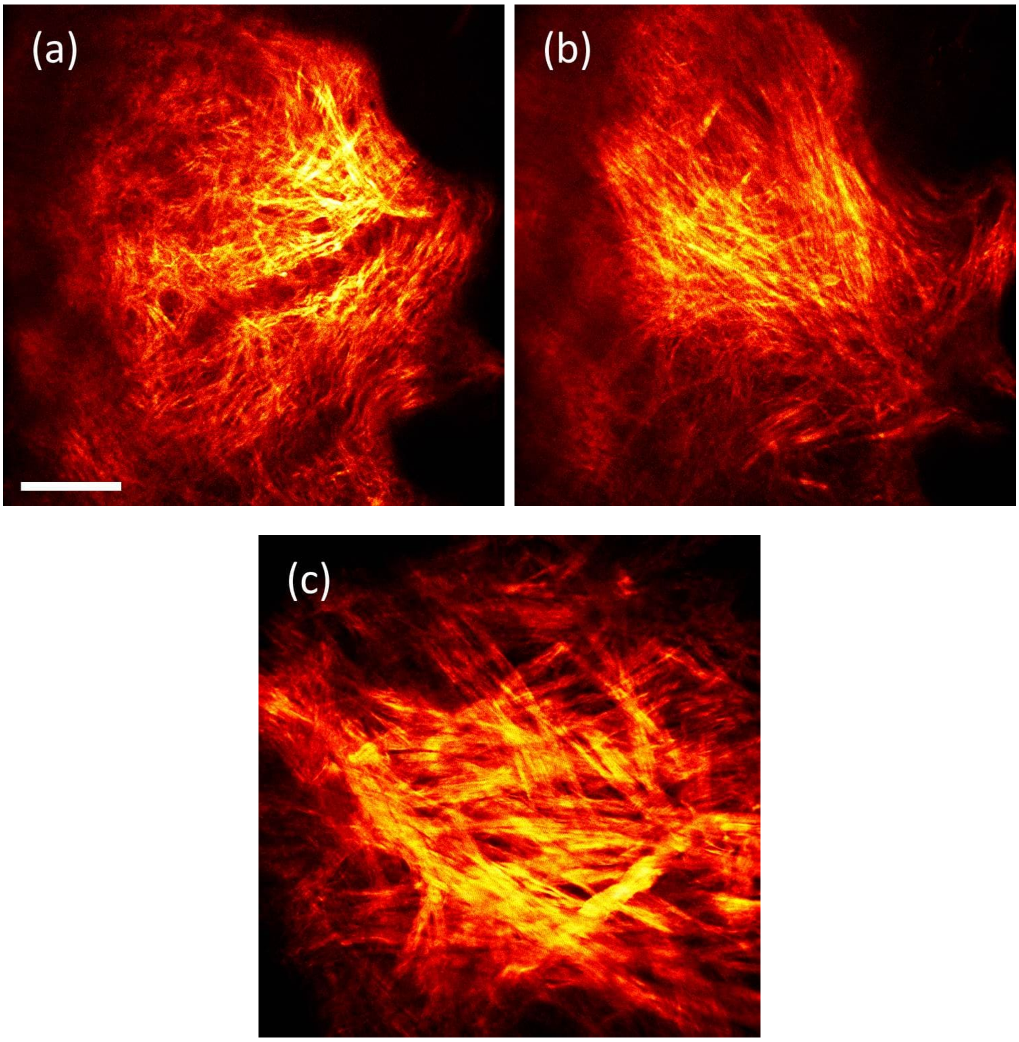

Figure 5.5: SHG imaging of the fiber network in dermis of *ex vivo* human skin from the head part excited by 1250-nm femtosecond pulses at different penetration depth. (a) 130 μm. (b) 150 μm. (c) 170 μm.

(This page is intentionally kept blank.)

Figure 5.6 shows the 2PEF imaging of human skin from the head part excited by 775-nm femtosecond pulses *ex vivo*. The maximal excitation power after the objective is 30 mW, corresponding to $\sim$ 1-nJ pulse energy. The FOV is 270 μm × 270 μm.

The imaging contrast of 2PEF is provided by intrinsic chromophores in the cytoplasm, which can be used to distinguish different stratums in the same FOV. For example, nucleiless SC appears in the right part of Fig. 5.6(a) at 30-μm depth, whereas SG occupies the middle and the left area. Granular cells are named due to their cytoplasm containing keratohyalin granules. Their shape also looks flatter compared with the subsequent SS. SS constitutes most of the epidermis besides SC. Spinous cells in the upper SS also exhibit granular features within their cytoplasm [Fig. 5.6(b) and Fig. 5.6(c)]. The NC-ratio of spinous cells gradually rises as the imaging depth increases from 40 μm to 65 μm [Fig. 5.6(b-e)]. Basal cells with the highest NC-ratio are shown at the top left corner of Fig. 5.6(e) and 5.6(f). Under 775-nm excitation, keratin, melanin, NADH, and collagen all can contribute to autofluorescence [111]. We observed this fluorescence crosstalk between epidermal cells and collagen fibers at the DP shown in Fig. 5.6(f).

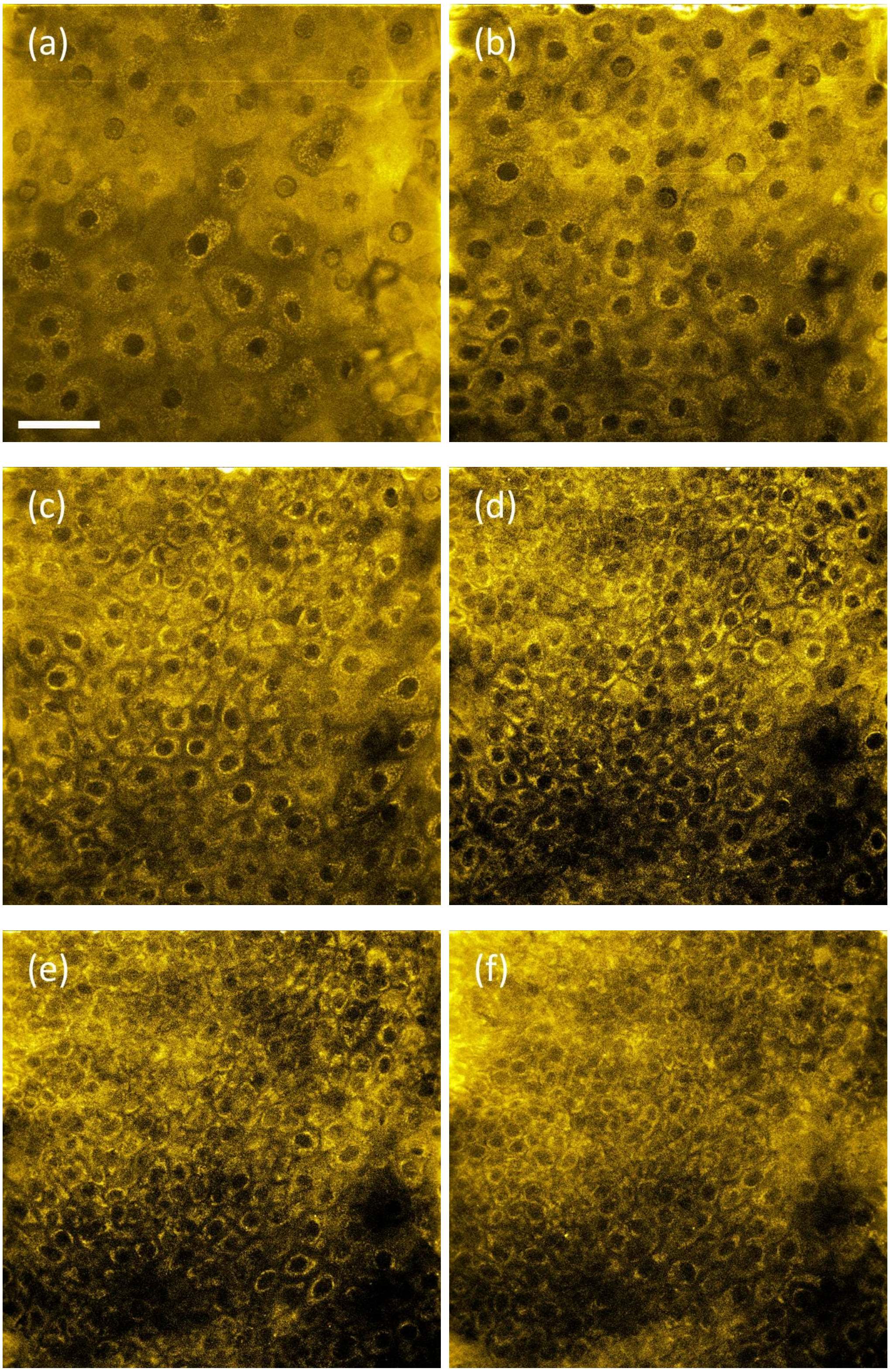

Figure 5.6: 2PEF imaging of *ex vivo* human skin from the head part excited by 775-nm femtosecond pulses at different penetration depth. (a) 30 μm. (b) 40 μm. (c) 50 μm. (d) 60 μm. (e) 65 μm. (f) 70 μm. Scale bar: 50 μm.

Figure 5.7 shows the imaging of *ex vivo* human skin from the head part visualized by different modalities. The contrast agent in Fig. 5.7(a-c) is mainly THG excited by 1250-nm femtosecond pulses, and the one in Fig. 5.7(d-f) originates from 2PEF excited by 775-nm femtosecond pulses. Figure 5.7(a) and (d) are SG at 30-μm depth. Figure 5.7(b) and (e) are SS at 50-μm depth. Figure 5.7(c) and (f) are DP at 70-μm depth. The fluorescence crosstalk between epidermal cells and collagen fibers are still observed in Fig. 5.7(f), but can be easily distinguished by SHG and THG in Fig. 5.7(c). Both THG and 2PEF modalities are able to differentiate stratums in epidermis. However, these epidermal cells look different even at the same imaging depth, since the 2PEF contrast comes from intrinsic chromophores in the cytoplasm and the THG contrast originates from optical inhomogeneity of the cell membrane.

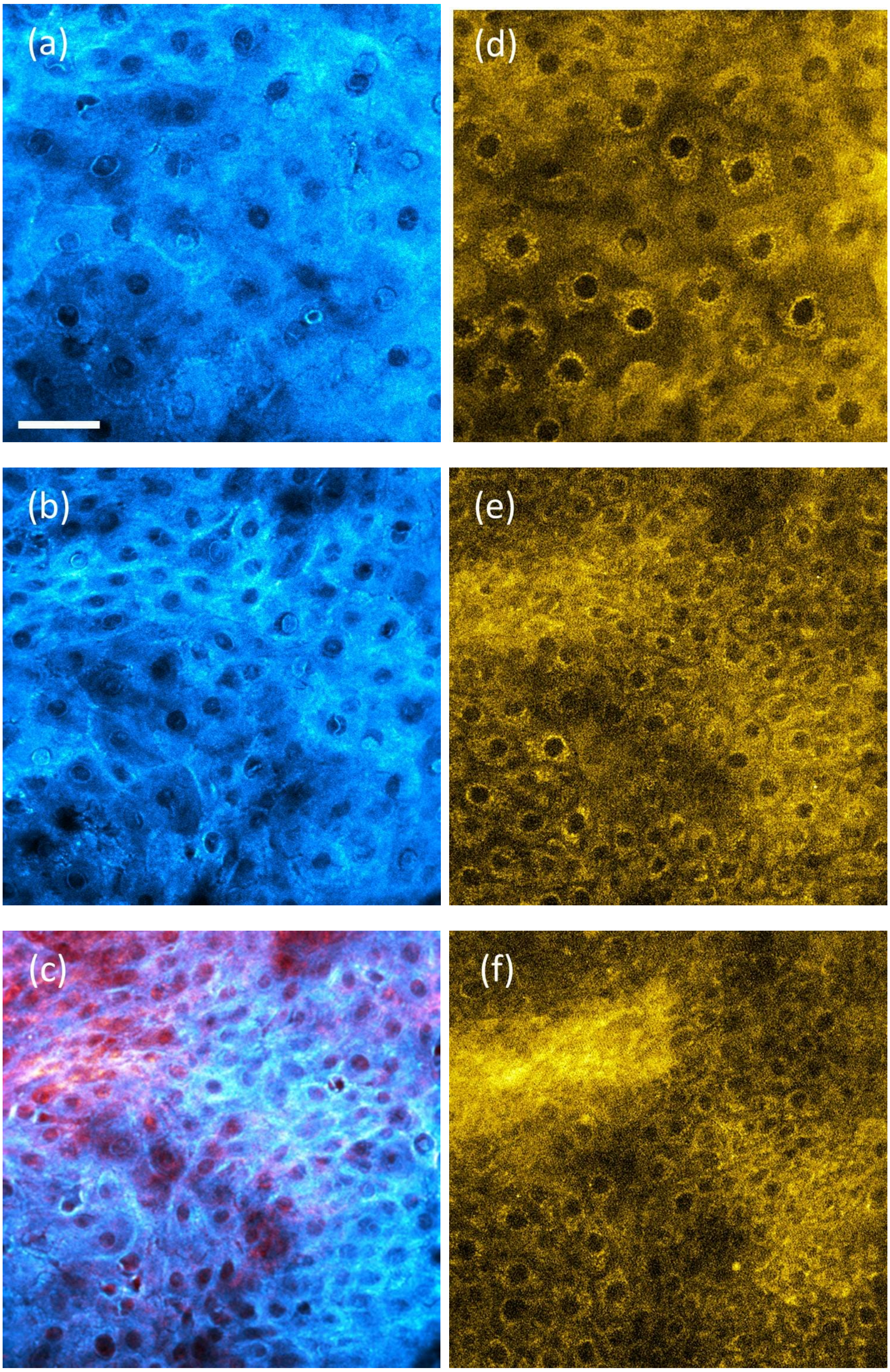

Figure 5.7: *Ex vivo* human skin from the head part visualized by different modalities. (a-c) HGM imaging excited by 1250-nm femtosecond pulses. (d-f) 2PEF imaging excited by 775-nm femtosecond pulses. Scale bar: 50 μm.

5.3 Protein crystal detection

X-ray diffraction crystallography is a widely used technique to study and determine the three-dimensional molecular structure of proteins [159, 160]. The diffraction pattern can indicate the space group of protein crystals and provide vital information for the design of new drugs leading to new therapies.

In recent years, many synchrotron facilities have been developed, and femtosecond nano-crystallography has become an optimized route in structural research particularly in the study of membrane proteins that have limited abilities to form large crystals. In the meantime, the size of protein crystals required for diffraction data collection illuminated by these highly brilliant X-ray sources is continuously decreasing. Ideally, nanometer-sized crystals can be utilized to provide diffraction patterns. Thus, accurate detection of protein crystals and differentation from salts *in situ* are essential for nano-crystallography prior to the X-ray diffraction to avoid false-positive signals.

5.3.1 Imaging protein crystals

In general, during the protein crystallization the sample usually contains not only pure protein crystals, but also accompanying random clusters of protein and salt crystals. The latter two components might contribute to false-positive signals and thus affect the resulting X-ray diffraction pattern, resulting in an inaccurate determination of the sample structure. Thus, how to distinguish these components becomes an important issue for the structure analysis while implementing X-ray diffraction, and stimulates the development of various techniques to detect protein crystals based on different mechanisms, e.g., bright-field detection under the normal optical microscope, fluorescence detection, and SHG detection.

SHG is only allowed in materials that do not possess centrosymmetry as explained in Sec. 1.1.1. An estimated 84% of the protein crystals in the Protein Data Bank (PDB) are non-centrosymmetric [161, 162, 163], therefore they can be visualized by SHG modality. However, some of them generate only weak SHG signal. Also, there might exist false-positive signal resulted from salt crystals also with non-centrosymmetry. To distinguish salt from protein crystals under this circumstance, one can employ fluorescence imaging. For example, proteins contain aromatic amino acids (AAAs) are able to emit autofluorescence by the UV illumination, whereas salts exhibit no such feature. Figure 5.8 shows the absorption and emission spectra of common AAAs, including Tryptophan (Try), Tyrosine (Tyr), and Phenylalanine (Phe). Tryptophan and Tyrosine have much higher absorbance compared with Phenylalanine. Their absorption wavelength peaks between 258 nm and 280 nm corresponding to the emission wavelength peaking between 280 nm and 354 nm. Conventionally, fluorescence imaging utilizes a 280-nm light source to excite Tryptophan in most proteins and detects the UV fluorescence emission at $\sim$350 nm.

As a result, the three major components (protein crystals, protein random clusters, and salt crystals) during the protein crystallization can be distinguished

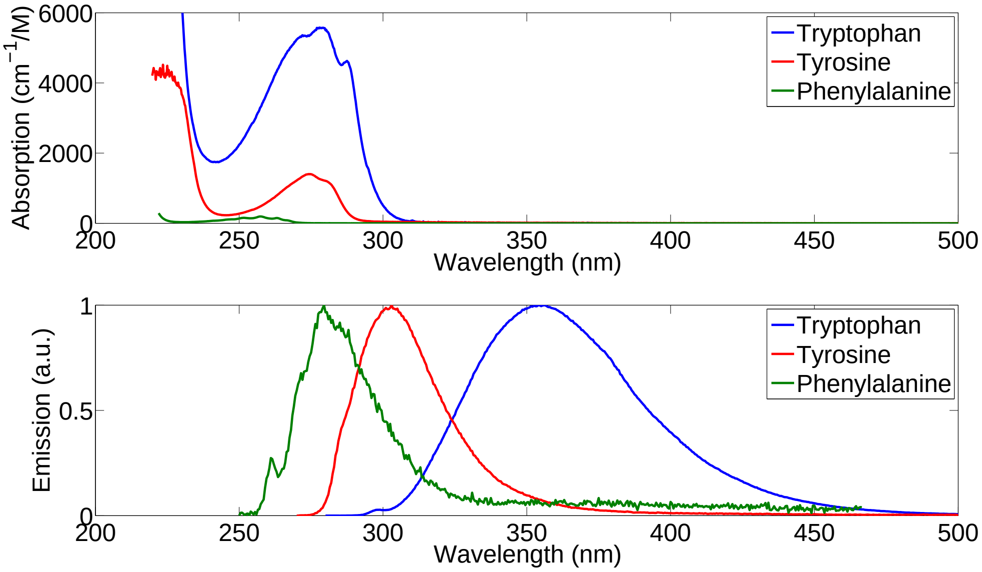

Figure 5.8: Absorption and emission spectra of common AAAs.

by SHG and UV fluorescence modalities without additional bio-markers. We summarize the flow process in Fig. 5.9. First, SHG detection allows the exclusion of random protein clusters. Followed by the UV fluorescence detection we can further distinguish protein from salt crystals.

The absorption band of AAAs is in the range of UVC (100-280 nm), which exhibits poor objective transmittance. In addition, one-photon UV excitation fluorescence presents practical challenges with respect to the background suppression (due to the overlap of the absorption and emission spectra), and can induce photochemical damage [164]. To cope with this issue, an alternative is to excite the autofluorescence via multi-photon absorption, e.g., 2PA at 516-560 nm or 3PA at 774-840 nm.

Many instruments are designed and implemented to identify protein crystals, which usually consist of a multiphoton microscope driven by an ultrafast laser incorporating two modalities—SHG and 2PEF. Since SHG relates to only the virtual state energy transition, one can choose the excitation wavelength at will. For 2PEF, the excitation wavelength must be corresponding to the real state energy transition in the targeting chromophore. Although ∼530-nm excitation allows 2PEF of protein, the resulting SHG (265 nm) is in the UVC range, which is hard to be detected due to its low transmittance and lack of efficient detectors. Thus, a second excitation beam with longer wavelength is usually employed, so the resulting SHG can fall into the visible range. Ultrafast lasers (e.g., Nd:YAG lasers and YDFLs) generating pulses at 1064 nm serve as such two-color driving sources for this purpose [165, 166]. The fundamental 1064-nm illumination supports not only SHG imaging. After frequency doubling in a nonlinear crystal, the 532-nm illumination can be used for 2PEF modality.

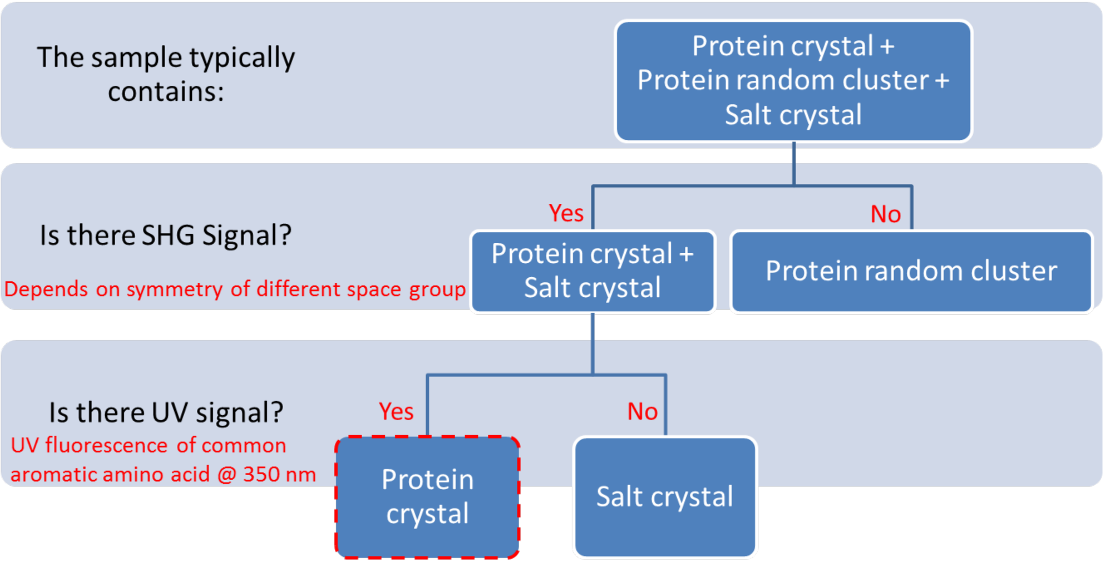

Figure 5.9: Identification of protein crystals by SHG and UV autofluorescence.

In principle, a driving source at ∼800 nm can also fulfill the requirement provided by a Ti:sapphire laser or by our versatile EDFL-based source shown in Sec. 5.1.1. The 775-nm beam can alone excite SHG and 3PEF for protein crystal detection. Besides these modalities, THG imaging driven by a wavelength tunable SESS source is also available as a complementary technique to investigate the sample.

5.3.2 EDFL-based ultrafast source for protein crystal detection

In this section we demonstrate protein crystal detection enabled by an EDFL-based source. The system depicted in Fig. 5.10 is similar to the setup in Fig. 5.1. The two-color ultrafast source is based on an EDFL pumped nonlinear wavelength converters (frequency doubling and SESS). Compared with Sec. 5.1.1, we employ 1550-nm femtosecond pulses with higher input power (1160 mW) focusing into the 0.3-mm long MgO:PPLN crystal (MSHG1550-0.5-0.3, Covesion), which results in frequency doubled pulses at 775 nm with 360-mW average power, corresponding to 11.6 nJ pulse energy and a slightly increased conversion efficiency of 31%. By implementing SESS in 9-cm DSF we obtain femtosecond pulses peaking at 1300 nm with 290-mW average power (corresponding to 9.4-nJ pulse energy) filtered by a BPF with 50-nm spectral width.

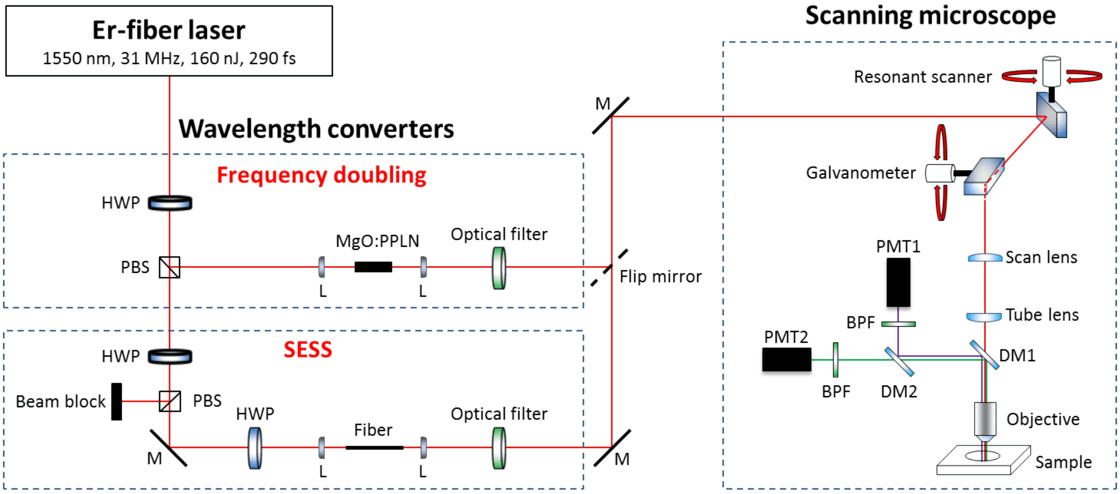

Figure 5.10: Schematic setup of the multimodal microscope for protein crystal detection.

A flip mirror is used to select 775-nm or 1300-nm excitation according to SHG/3PEF or SHG/THG detection. DM1 (F665-Di02-25 × 36, Semrock) allows the transmission of 775-nm and 1300-nm excitation, and reflects the emitted signals epi-collected by the 25× objective (XLPLN25XWMP2, Olympus). We use different set of DM2 and BPFs according to the modalities. Under 1300-nm excitation for SHG/THG detection, we use DM (FF562-Di03-25 × 36, Semrock) and BPFs (#84-786, #86-949, Edmund Optics). Under 775-nm excitation for SHG/3PEF detection, we use DM (Di01-R355-25 × 36, Semrock) and BPFs (FF-387/11-25, FF01-355/40-25, Semrock).

Figure 5.11: PDMS chip for crystal growth and storage.

We use polydimethylsiloxane (PDMS) microfluidic chips to grow and store the protein crystals. Precipitant solutions are usually used to grow and make the crystalization of protein easier. For example, thaumatin can be grown in sodium tartrate ($C_4H_4O_6Na_2$) solution. However, this inevitably leads to a mixture of protein and salt in the final product. Figure 5.11 shows the PDMS chip observed under the conventional white-light microscope. The wells labeled with numbers from F31 to F34 are full of the mixture of protein (thaumatin) and salt (sodium tartrate) crystals. For the succeeding X-ray diffraction experiment, it is crucial to distinguish these two components to avoid the possible false-true signals.

We use our multimodal microscope to investigate this PDMS chip. Excited by 1300-nm femtosecond pulses, the SHG/THG imaging is shown in Fig. 5.12. The FOV is 500 μm × 500 μm. Both crystals can emit SHG [Fig. 5.12(a)]. Also, the difference of SHG contrast indicates that these two kinds of crystal possess different degree of non-centrosymmetry. The THG imaging originated from interfaces depicts the outline of the crystals and also the labeled numbers from F32 to F34 on the chip [Fig. 5.12(b)].

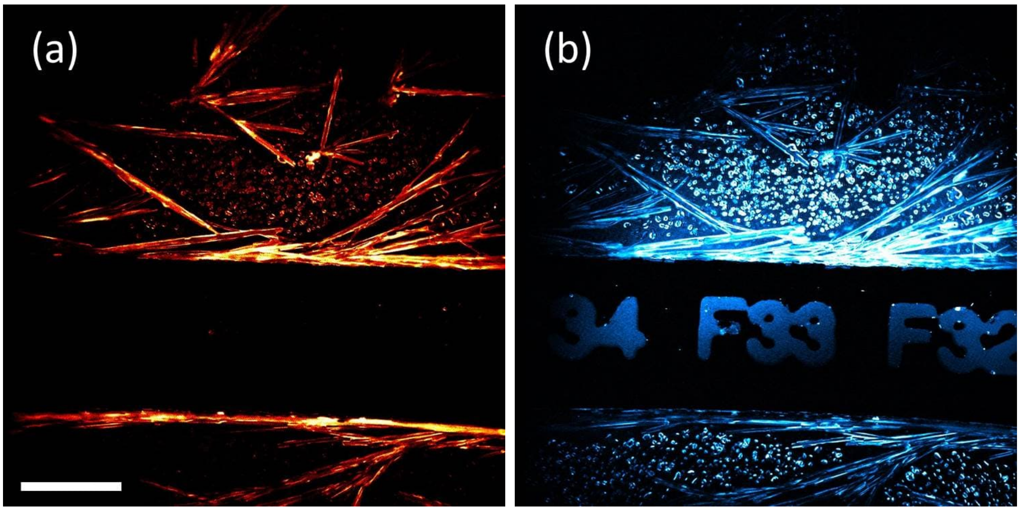

Figure 5.12: PDMS chip visualized by (a) SHG and (b) THG. Scale bar: 100 μm.

To demonstrate that protein and salt crystals can be distinguished by SHG/3PEF detection, we change the illumination wavelength to 775 nm. Figure 5.13 shows the resulting SHG/3PEF imaging. The FOV is 270 μm × 270 μm. The SHG imaging in Fig. 5.13(a) and 5.13(c) presents two kinds of crystals—the one with needle-like shape emitting strong SHG and the one with small size emitting weak SHG. A preliminary speculation suggests that the needle-like crystal is sodium tartrate because its space group is P $2_1 2_1 2_1$, which is less centrosymmetric than thaumatin (space group: P $4_1 2_1 2$), and thus leads to stronger SHG. To confirm this assumption, we compare these two crystals visualized by 3PEF in Fig. 5.13(b) and 5.13(d). As expected, the part emitting strong SHG shows almost no 3PEF compared with the smaller crystals. The outline of sodium tartrate can still be visualized by 3PEF, indicating some aggregation of thaumatin on the surface of sodium tartrate.

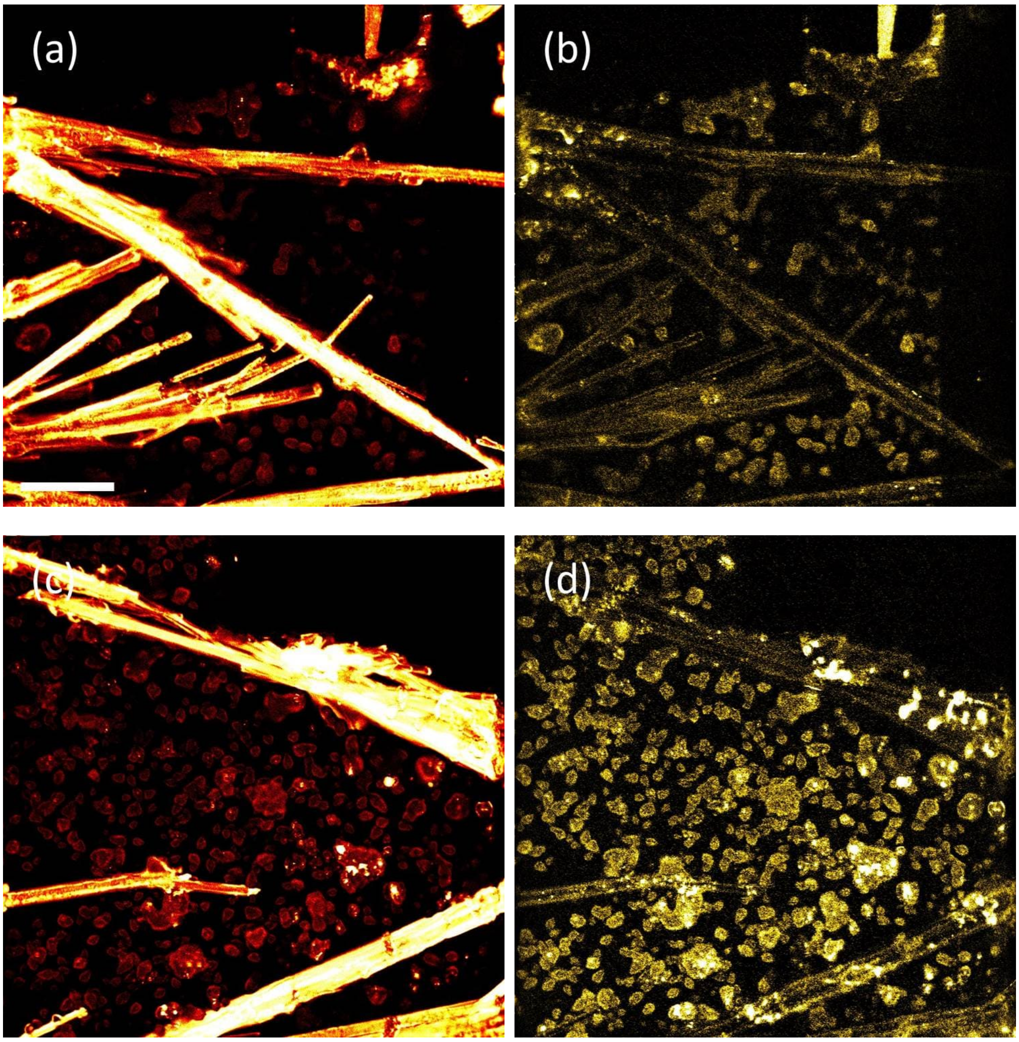

Figure 5.13: SHG/3PEF imaging of the mixture of protein and salt crystals. Scale bar: 50 μm.

Besides thaumatin and sodium tartrate, the multimodal microscope is also able to detect many other different crystals. Figure 5.14 shows the multimodal imaging (THG, SHG, and 3PEF) of protein crystal lysozyme (space group: P $4_3 2_1 2$) with different size. The size of the crystal ranges from more than 100 μm to less than 10 μm.

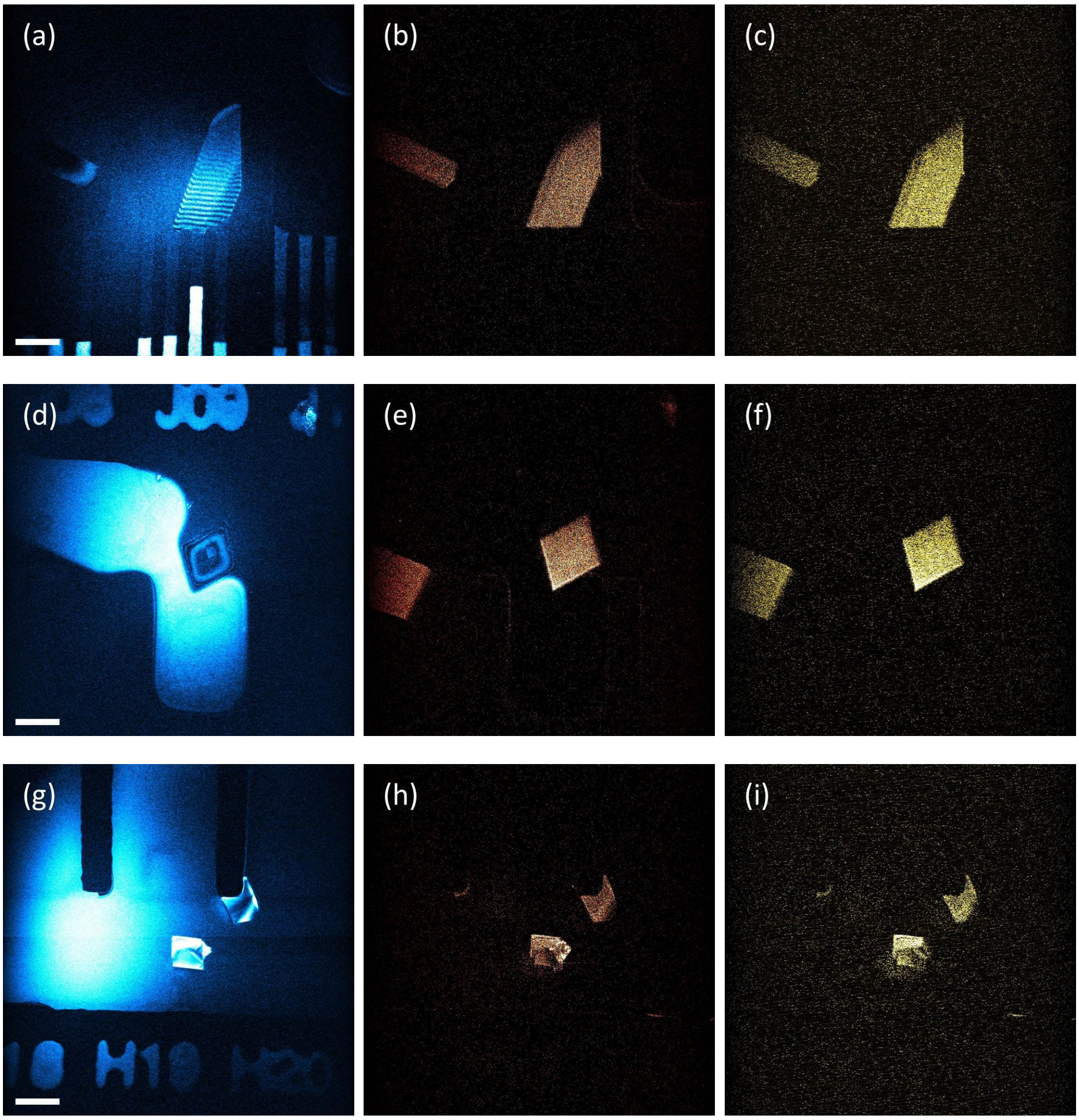

Figure 5.14: Multimodal imaging of protein crystal lysozyme with different size. Scale bar: 100 μm.

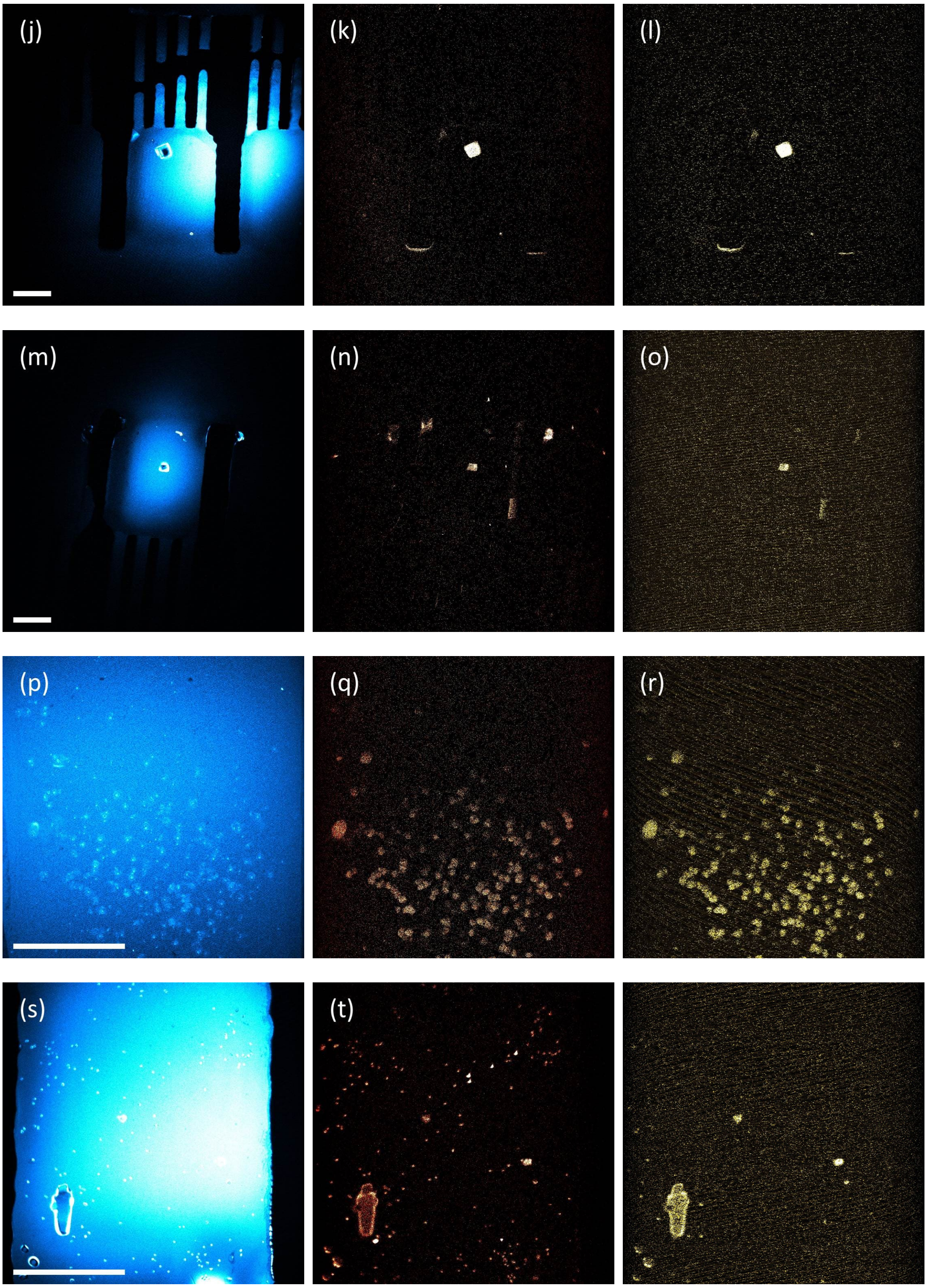

Figure 5.14: Multimodal imaging of protein crystal lysozyme with different size. Scale bar: 100 μm.

Figure 5.15 shows the multimodal imaging (THG, SHG, and 3PEF) of different protein crystals, including proteinase K (space group: P $4_3 2_1 2$) [Fig. 5.15(a-c)], glucose isomerase (space group: I 2 2 2) [Fig. 5.15(d-f)], and bovine serum albumin (BSA) (space group: C 1 2 1) [Fig. 5.15(g-i)].

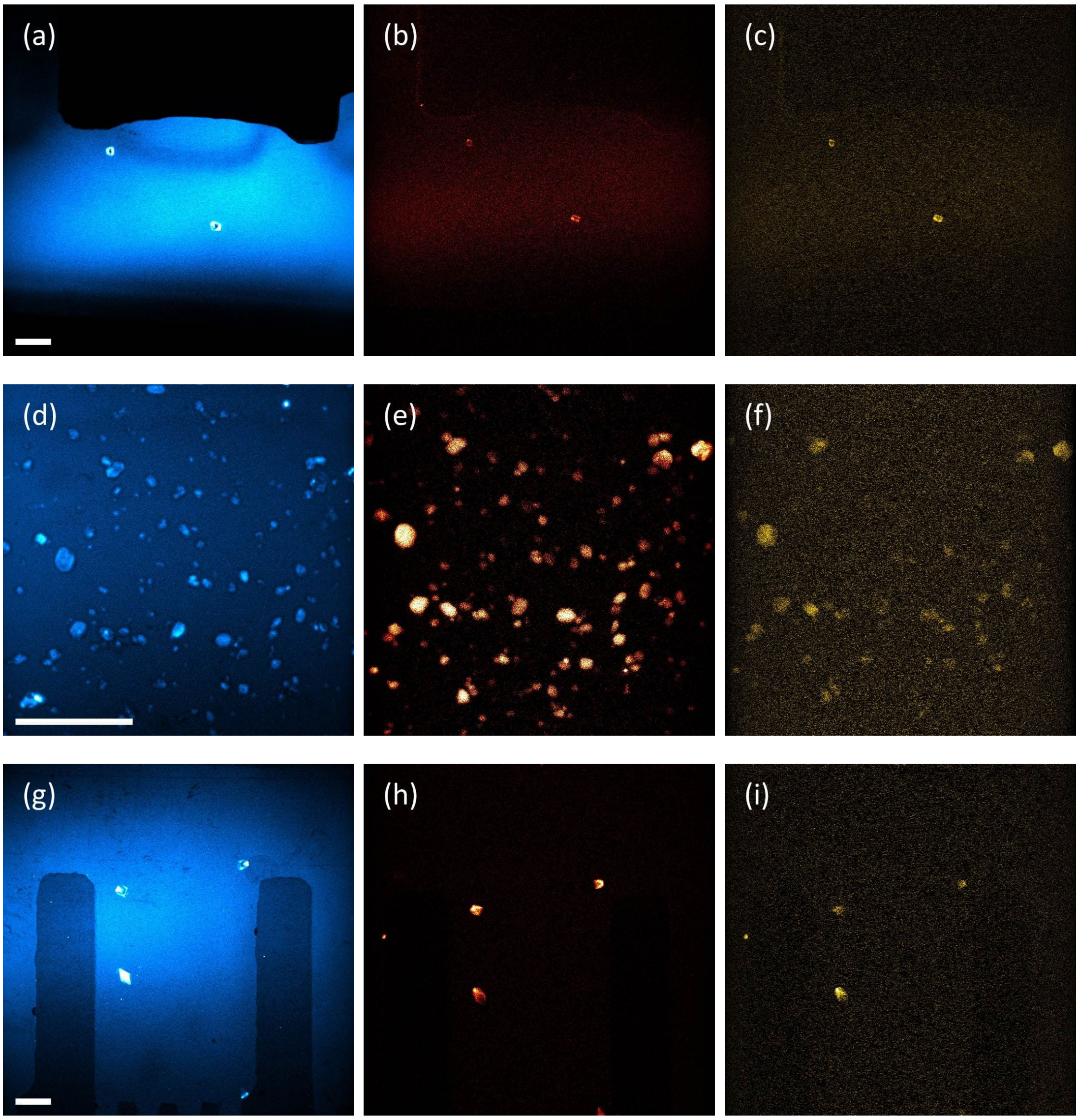

Figure 5.15: Multimodal imaging of different protein crystals proteinase K, glucose isomerase, and BSA. Scale bar: 50 μm.

We use BPFs with wavelength centered at the half of the excitation wavelength for SHG detection. To avoid the possible false-positive SHG due to fluorescence crosstalk, once can employ the polarization-dependent feature of SHG. Figure. 5.16 shows the SHG/THG imaging of protein crystal glucose isomerase excited by 1300-nm femtosecond pulses. The THG imaging shows the crystals aggregating inside the tunnel and well of the PDMS chip [Fig. 5.16(a)]. We use an HWP to adjust the polarization of the excitation beam. The resulting SHG imaging shown in Fig. 5.16(b-k) are excited, while the HWP is tuned from 0^o to 90^o with 10^o polarization difference each time. Due to the random crystal orientation, the polarization leading to strong SHG for one crystal might not be suitable for another one. For example, the two crystals at the top right corner of the FOV.

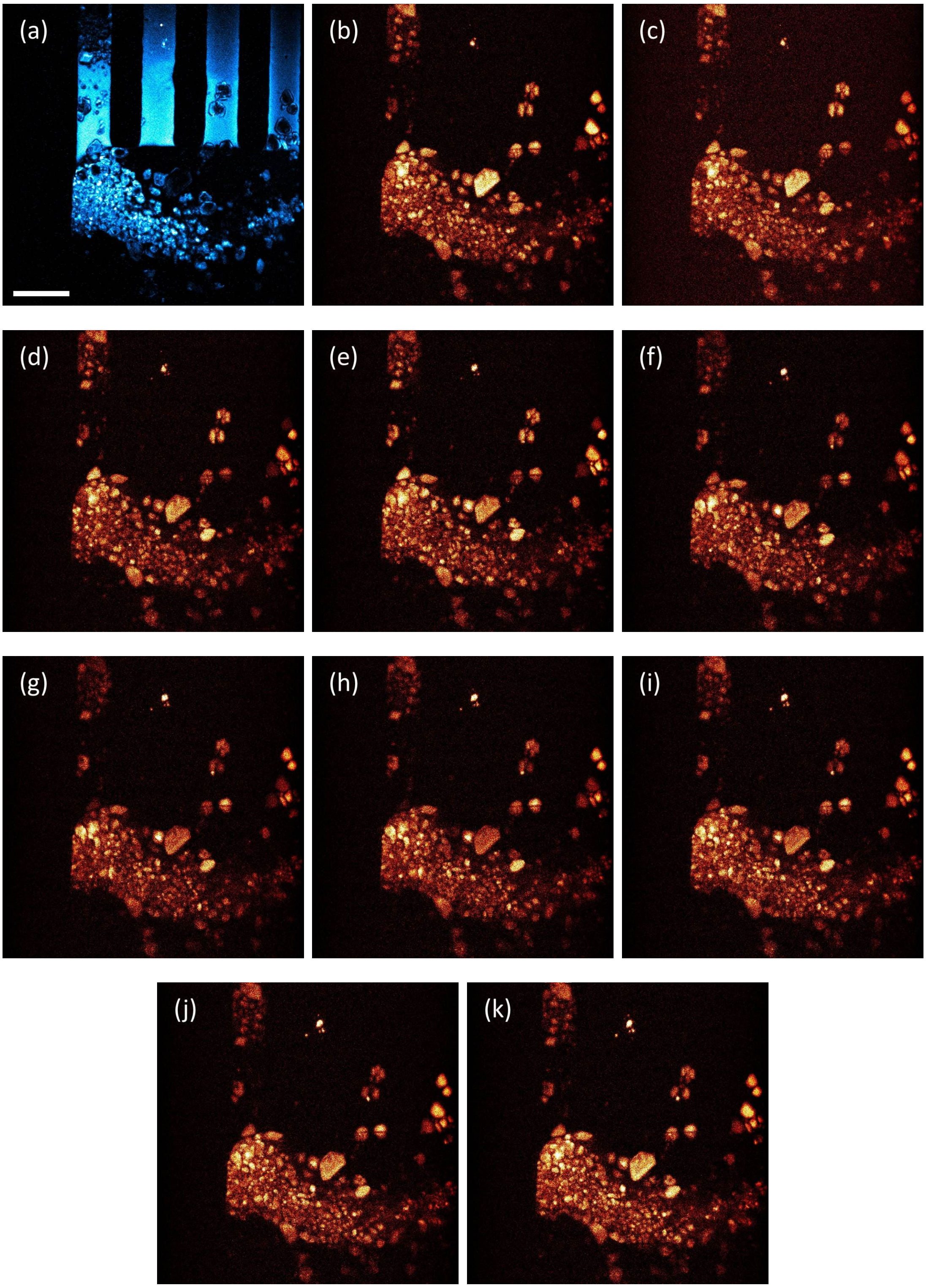

Figure 5.16: SHG/THG imaging of protein crystal glucose isomerase excited by 1300-nm femtosecond pulses with different polarization. Scale bar: 50 μm.

Figure 5.17 shows the multimodal imaging (THG, SHG, and 3PEF) of different salt crystals, including NaCl (space group: F m-3m) [Fig. 5.17(a-c)], $Li_2SO_4 \cdot H_2O$ (space group: P 2_1) [Fig. 5.17(d-f)], and Na_2SO_4 [Fig. 5.17(g-i)]. Obviously, the 3PEF channel shows no signal compared with protein crystals. It is noteworthy that the SHG signal appears even from crystals with highly centrosymmetry, e.g., NaCl in Fig. 5.17(b) and Na_2SO_4 in Fig. 5.17(h). This does not contradict that SHG is only allowed in structures with non-centrosymmetry because the SHG can originate from edges and interfaces, where the symmetry is broken [167]. The surface SHG [Fig. 5.17(b) and Fig. 5.17(h)] can also depict the sample outline and almost overlaps with the THG imaging [Fig. 5.17(a) and Fig. 5.17(g)] in comparison with the bulk SHG in $Li_2SO_4 \cdot H_2O$ [Fig. 5.17(e)].

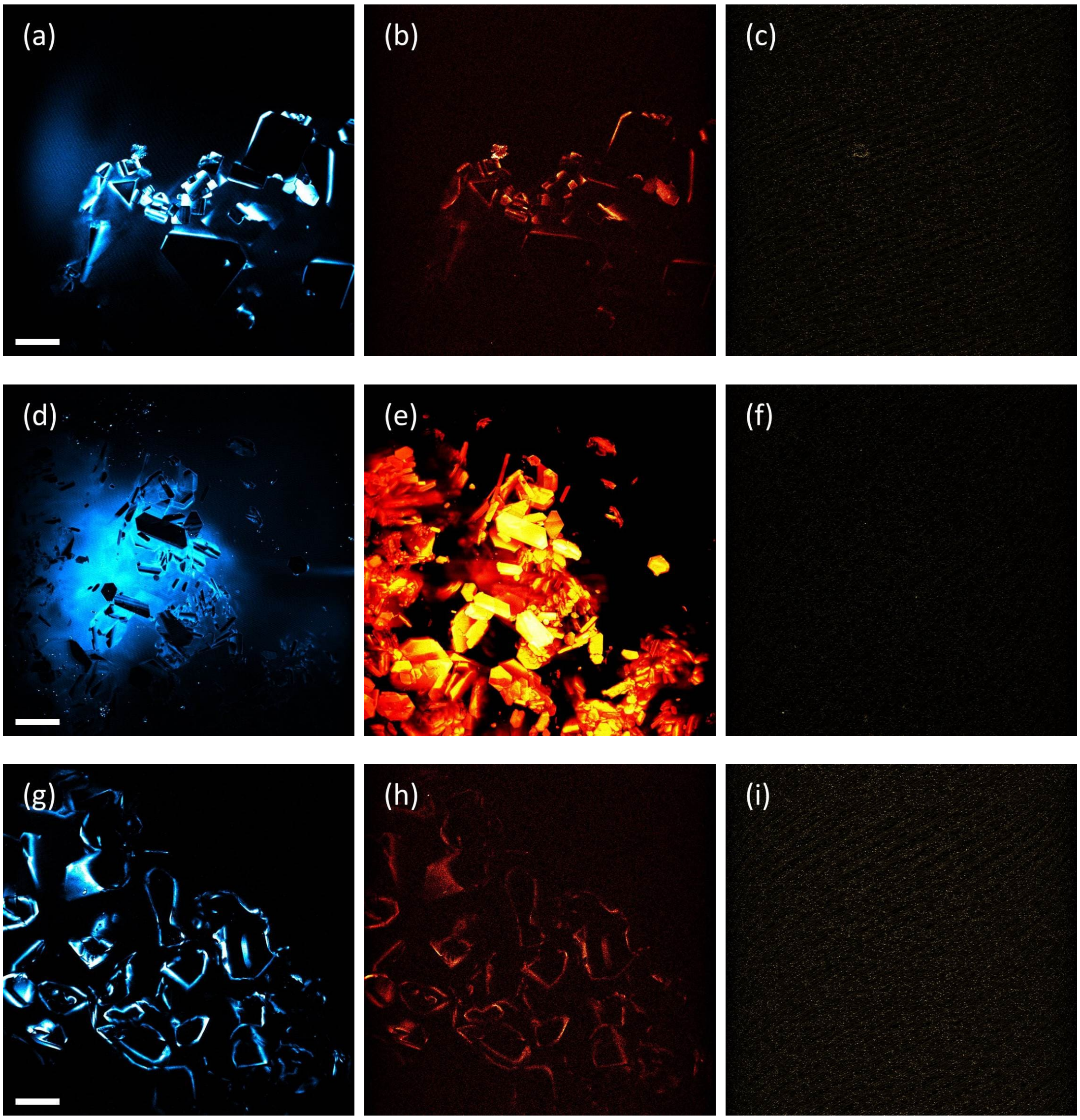

Figure 5.17: Multimodal imaging of different salt crystals NaCl, $Li_2SO_4 \cdot H_2O$, and Na_2SO_4. Scale bar: 100 μm.

5.4 Conclusion of Chapter 5

In this chapter we demonstrate an EDFL-based two-color ultrafast source to drive multimodal MPM. Besides the tunable source generated by SESS, frequency doubling in a MgO:PPLN crystal allows us to generate femtosecond pulses at 775 nm within the conventional Ti:sapphire laser wavelength range, which can drive MPEF microscopy of many endogenous fluorophores. We apply this two-color source to two applications—multimodal label-free human skin imaging and protein crystal detection. Different modalities (SHG, THG, 2PEF, and 3PEF) are available, and up to 3-channel (SHG, THG, and 2PEF) detection is possible. Though demonstrated here only for human skin and protein crystal imaging, this platform can be flexibly used for various multiphoton imaging applications using other bio-markers [35, 169].

As we have demonstrated in Sec. 3.2.2 and Sec. 4.2.1, our SESS source can generate femtosecond pulses with the center wavelength tunable in 1150-1700 nm. Using a proper fanout PPLN crystal for frequency doubling, we can obtain femtosecond pulses in the wavelength range of 575-850 nm covering the two-photon excitation wavelength for many other important fluorophores [33, 34] and fluorescent proteins [35]. For example, the rightmost spectral lobe peaking at 1700 nm of the broadened spectrum from 9-cm DSF also contains much pulse energy (>10 nJ) [Fig. 5.2(a)]. Filtering this part followed by frequency doubling can produce femtosecond pulses at 850 nm, suitable for 2PEF of flavin adenine dinucleotide (FAD) [33]. Similar to NADH, FAD plays an important role in cell metabolism. Functional contrast of both indicators can be distinguished by fluorescence-lifetime imaging microscopy (FLIM) [168], and the fluorescence intensity of FAD/NADH serving as the optical redox ratio can be used to differentiate precancerous cells [168].

Such a multimodal microscope driven by an EDFL-based source constitutes a low-cost, miniaturized, flexible solution to biological study and exhibits high potential for clinical applications compared with conventional solid-state lasers.

Chapter 6

Conclusion and outlook

MPM is one of the most important applications of ultrafast lasers. Depending on the interaction between ultrafast pulses and tissues, various modalities (e.g., MPEF and HGM) are available for bio-imaging. The performance of MPM highly relies on the driving source generating energetic femtosecond pulses with flexibly tunable wavelength in the range of NIR. For example, Ti:sapphire lasers have been long serving as the workhorse to drive MPM. However, high complexity, high cost, and the bulky size of such a solid-state solution has spurred the intensive development of other alternatives. In this thesis, we demonstrate a new fiber-optic technology—SESS—to derive wavelength widely tunable femtosecond pulses based on an EDFL to drive MPM.

In Chapter 2, we first numerically modeled ultrafast pulses propagating inside an optical fiber and studied the SPM-dominated spectral broadening. To experimentally demonstrate a SESS source, we constructed a 31-MHz high-power EDFL system that generates 290-fs pulses centered at 1.55 μm with 160-nJ pulse energy (corresponding to ∼5-W average power). We then employed this laser source to evaluate SESS in six types of optical fibers (e.g., standard SMFs, DSFs, DCFs, and HNLFs) that exhibit different dispersions at the pump wavelength.

In Chapter 3, we explored the energy scalability of SESS. In general, the resulting pulse energy of SESS can be scaled up either by shortening the fiber length or by using fibers with larger MFA. We also investigated the feasibility of SESS implemented in fibers with negative GVD and found that SPM dominates the spectral broadening prior to soliton fission. The associated higher-order soliton compression can increase the pulse peak power, thus benefits the spectral broadening. Employing SESS in 7-cm DSF pumped by an EDFL resulted in ∼16-nJ femtosecond pulses at 1.3 μm and 1.7 μm simultaneously. To further demonstrate the superior energy scalability of SESS, we pumped 1.3-cm DSF by a home-built OPA and achieved >100-nJ femtosecond pulses at 1.3 μm and 1.7 μm. The resulting pulse peak power corresponds to MW level and constitutes a solution to deep-tissue 3PEF imaging.

We applied the EDFL-based SESS source to drive HGM for optical virtual skin biopsy in Chapter 4. The SESS source generates femtosecond pulses with up to >10-nJ pulse energy tunable between 1.15 μm and 1.35 μm covering the biological transmission window. We integrated this ultrafast source with a scanning microscope and conducted HGM in human skin *ex vivo*. The resulting SHG/THG imaging is able to differentiate stratums and tissues in epidermis and upper dermis. We compared the performance of different excitation in the range of 1.15-1.35 μm with the same peak power after the objective. The experimental results suggest that excitation between 1.15 μm and 1.25 μm is suitable for HGM in human skin.

By frequency doubling a small portion of the EDFL output in a MgO:PPLN crystal, we obtained femtosecond pulses at 775 nm within the conventional Ti:sapphire laser wavelength range, which support MPEF of many endogenous fluorophores. Combing with SESS, the two-color source is able to drive multimodal MPM (i.e., SHG, THG, 2PEF, and 3PEF). In Chapter 5, we demonstrated two examples—label-free human skin imaging (SHG, THG, and 2PEF) and protein crystal detection (SHG, THG, and 3PEF).

In conclusion, we presented an EDFL-based ultrafast source for MPM. By implementing SESS in optical fibers pumped by an EDFL at 1.55 μm we can generate energetic, nearly transform-limited femtosecond pulses continuously tunable between 1.15 μm and 1.7 μm. SESS exhibits excellent energy scalability. With a low-repetition-rate, μJ-level EDFL pump source, >100-nJ widely tunable femtosecond pulses with MW peak power is feasible in a fiber format, constituting a compact, robust, and cost-effective solution compared with solid-state lasers. Besides MPEF and HGM application demonstrated in this dissertation, the two-color scheme can also be applied to CRS microscopy with a fixed pump beam at 775 nm and a tunable Stokes beam enabled by SESS to induce different molecular vibrations. Not restricted only to MPM, similar scheme can be used to the generate mid-infrared pulses by difference frequency generation for the application of spectroscopy, metrology, and pump-probe experiment. We believe that such a powerful fiber-based SESS source will open many new applications.

Appendix A

Nomenclature

Table A.1: Definitation of notations used in the dissertation.

Notation	**Definition**
1PEF	one-photon excitation fluorescence
2PA	two-photon absorption
2PEF	two-photon excitation fluorescence
3PA	three-photon absorption
3PEF	three-photon excitation fluorescence
BCC	basal cell carcinoma
BPF	bandpass filter
CARS	coherent anti-Stokes Raman scattering
CPA	chirped-pulse amplification
CR	Cherenkov radiation
CRS	coherent Raman scattering
DCF	dispersion-compensating fiber
DFG	difference frequency generation
DM	dichroic mirror
DP	dermal papilla
DSF	dispersion-shifted fiber
DW	dispersive wave
EDF	erbium-doped fiber
EDFA	erbium-doped fiber amplifier
EDFL	erbium-doped fiber laser
Er	erbium
EYDF	erbium ytterbium co-doped fiber
FWHM	full-width at half-maximum

Continued on next page

Table A.1: Definitions of notations used in this dissertation

Notation	Definition
FWM	four-wave mixing
GDD	group-delay dispersion
GFP	green fluorescent protein
GNLSE	generalized nonlinear Schrödinger equation
GVD	group-velocity dispersion
HG	harmonic generation
HGM	harmonic generation microscopy
HNLF	highly nonlinear fiber
HWP	half-wave plate
ISO	isolator
LMA	large mode-area
LPF	longpass filter
LSM	laser scanning microscope
MFA	mode-field area
MFD	mode-field diameter
MM	malignant melanoma
MOPA	master oscillator power amplifier
MPEF	multi-photon excitation fluorescence
MPM	multi-photon microscopy
NADH	reduced nicotinamide adenine dinucleotide
NA	numerical aperture
NC	nuclear-cytoplasmic
NIR	near-infrared
NLOM	nonlinear optical microscopy
OPA	optical parametric amplifier
OPO	optical parametric oscillator
PBS	polarization beam splitter
PCF	photonic-crystal fiber
PER	polarization extinction ratio
PM	polarization-maintaining
PMT	photomultiplier tube
QWP	quarter-wave plate
RFP	red fluorescent protein
SAM	saturable absorber mirror

Continued on next page

Table A.1: Definitions of notations used in this dissertation

Notation	**Definition**
SB	stratum basale
SC	stratum corneum
SCC	squamous cell carcinoma
SESS	self-phase modulation enabled spectral selection
SG	stratum granulosum
SHG	second-harmonic generation
SL	stratum lucidum
SMF	single-mode fiber
SONICC	second-order nonlinear imaging of chiral crystals
SPF	shortpass filter
SPM	self-phase modulation
SRS	stimulated Raman scattering
SS	stratum spinosum
SS	self-steepening
SSFS	soliton self-frequency shift
THG	third-harmonic generation
TOD	third-order dispersion
UV	ultraviolet
WD	working distance
WDM	wavelength-division multiplexing
Yb	ytterbium
YDFA	ytterbium-doped fiber amplifier
YDFL	ytterbium-doped fiber laser
ZDW	zero-dispersion wavelength

Appendix B

Space Group of Common Crystals

Table B.1: Space group of common protein crystals.

Protein	Space group
Lysozyme	P $4_3 2_1 2$
Proteinase K	P $4_3 2_1 2$
Thaumatin	P $4_1 2_1 2$
Thermolysin	P $6_1 2\ 2$
Glucose isomerase	I 2 2 2
Bovine serum albumin (BSA)	C 1 2 1
Insulin	I $2_1 3$

Table B.2: Space group of common salt crystals.

Protein	Space group
NaCl	F m-3m
$Ca(CH_3COO)_2 \cdot H_2O$	P-1
$NaKC_4H_4O_6 \cdot H_2O$	P $2_12_12_1$
$Li_2SO_4 \cdot H_2O$	P 2_1
$CaCl_2 \cdot 2H_2O$	P n n m
KCl	F m-3m
$Na_3C_6H_5O_7 \cdot 2H_2O$	P 2/m
KH_2PO_4	I -42d
NH_4Cl	P m-3m
$MgCl_2$	R -3m
Na_2HPO_4	P 2_1/m
NaH_2PO_4	P 2_1/c
$NaNO_3$	R -3c
$(NH_4)_2SO_4$	P n m a
$NH_4H_2PO_4$	I -42d

Bibliography

[1] R. W. Boyd. *Nonlinear optics.* Academic press, 1992.

[2] P. A. Franken, A. E. Hill, C. W. Peters, and G. Weinreich. Generation of optical harmonics. *Phys. Rev. Lett.*, 7(4):118–119, 1961.

[3] R. Hellwarth and P. Christensen. Nonlinear optical microscopic examination of structure in polycrystalline ZnSe. *Opti. Commun.*, 12(3):318–322, 1974.

[4] I. Freund, M. Deutsch, and A. Sprecher. Connective tissue polarity. Optical second-harmonic microscopy, crossed-beam summation, and small-angle scattering in rat-tail tendon. *Biophys. J.*, 50(4):693–712, 1986.

[5] G. Peleg, A. Lewis, M. Linial, and L. M. Loew. Nonlinear optical measurement of membrane potential around single molecules at selected cellular sites. *Proc. Natl. Acad. Sci. U.S.A.*, 96(12):6700–6704, 1999.

[6] L. Moreaux, O. Sandre, and J. Mertz. Membrane imaging by second-harmonic generation microscopy. *J. Opt. Soc. Am. B*, 17(10):1685–1697, 2000.

[7] A. C. Millard, L. Jin, A. Lewis, and L. M. Loew. Direct measurement of the voltage sensitivity of second-harmonic generation from a membrane dye in patch-clamped cells. *Opt. Lett.*, 28(14):1221–1223, 2003.

[8] D. A. Dombeck, M. Blanchard-Desce, and W. W. Webb. Optical recording of action potentials with second-harmonic generation microscopy. *J. Neurosci.*, 24(4):999–1003, 2004.

[9] Y. Guo, P. P. Ho, H. Savage, D. Harris, S. Schantz, F. Liu, N. Zhadin, and R. R. Alfano. Second-harmonic tomography of tissues. *Opt. Lett.*, 22(17):1323–1325, 1997.

[10] D. A. Dombeck, K. A. Kasischke, H. D. Vishwasrao, M. Ingelsson, B. T. Hyman, and W. W. Webb. Uniform polarity microtubule assemblies imaged in native brain tissue by second-harmonic generation microscopy. *Proc. Natl. Acad. Sci. U.S.A.*, 100(12):7081–7086, 2003.

[11] A. Zoumi, A. Yeh, and B. J. Tromberg. Imaging cells and extracellular matrix *in vivo* by using second-harmonic generation and two-photon excited fluorescence. *Proc. Natl. Acad. Sci. U.S.A.*, 99(17):11014–11019, 2002.

[12] W. Mohler, A. C. Millard, and P. J. Campagnola. Second harmonic generation imaging of endogenous structural proteins. *Methods*, 29(1):97–109, 2003.

[13] W. R. Zipfel, R. M. Williams, R. Christie, A. Y. Nikitin, B. T. Hyman, and W. W. Webb. Live tissue intrinsic emission microscopy using multiphoton-excited native fluorescence and second harmonic generation. *Proc. Natl. Acad. Sci. U.S.A.*, 100(12):7075–7080, 2003.

[14] P. J. Campagnola, A. C. Millard, M. Terasaki, P. E. Hoppe, C. J. Malone, and W. A. Mohler. Three-dimensional high-resolution second-harmonic generation imaging of endogenous structural proteins in biological tissues. *Biophys. J.*, 82(1):493–508, 2002.

[15] T. Y. F. Tsang. Optical third-harmonic generation at interfaces. *Phys. Rev. A*, 52(5):4116–4125, 1995.

[16] Y. Guo, P. P. Ho, A. Tirksliunas, F. Liu, and R. R. Alfano. Optical harmonic generation from animal tissues by the use of picosecond and femtosecond laser pulses. *Appl. Opt.*, 35(34):6810–6813, 1996.

[17] Y. Barad, H. Eisenberg, M. Horowitz, and Y. Silberberg. Nonlinear scanning laser microscopy by third harmonic generation. *Appl. Phys. Lett.*, 70(8):922–924, 1997.

[18] M. Müller, J. Squier, K. R. Wilson, and G. J. Brakenhoff. 3D microscopy of transparent objects using third-harmonic generation. *J. Microsc.*, 191(3):266–274, 1998.

[19] J. A. Squier, M. Müller, G. J. Brakenhoff, and K. R. Wilson. Third harmonic generation microscopy. *Opt. Express*, 3(9):315, 1998.

[20] D. Yelin and Y. Silberberg. Laser scanning third-harmonic-generation microscopy in biology. *Opt. Express*, 5(8):169–175, 1999.

[21] S.-W. Chu, I-H. Chen, T.-M. Liu, Ping Chin Chen, C.-K. Sun, and B.-L. Lin. Multimodal nonlinear spectral microscopy based on a femtosecond Cr:forsterite laser. *Opt. Lett.*, 26(23):1909, 2001.

[22] C.-K. Sun, S.-W. Chu, S.-P. Tai, S. Keller, K. Mishra, and S. P. DenBaars. Scanning second-harmonic/third-harmonic generation microscopy of gallium nitride. *Appl. Phys. Lett.*, 77(15):2331–2333, 2000.

[23] M. Göppert-Mayer. Über Elementarakte mit zwei Quantensprüngen. *Ann. Phys.*, 9:273–294, 1931.

[24] W. Kaiser and C. G. B. Garrett. Two-photon excitation in CaF_2:Eu^{2+}. *Phys. Rev. Lett.*, 6(7):229–231, 1961.

[25] W. Denk, J. H. Strickler, and W. W. Webb. Two-photon laser scanning fluorescence microscopy. *Science*, 4951(248):73–76, 1990.

[26] L. A. Sordillo, Y. Pu, S. Pratavieira, Y. Budansky, and R. R. Alfano. Deep optical imaging of tissue using the second and third near-infrared spectral windows. *J. Biomed. Opt.*, 19(5):056004, 2014.

[27] Lingyan Shi, L. A. Sordillo, A. Rodr?guez-Contreras, and R. Alfano. Transmission in near-infrared optical windows for deep brain imaging. *J. Biophotonics*, 9(1-2):38–43, 2016.

[28] N. G. Horton, K. Wang, D. Kobat, C. G. Clark, F. W. Wise, C. B. Schaffer, and Chris Xu. *In vivo* three-photon microscopy of subcortical structures within an intact mouse brain. *Nat. Photon.*, 7(3):205–209, mar 2013.

[29] K. Wang, N. G. Horton, K. Charan, and C. Xu. Advanced fiber soliton sources for nonlinear deep tissue imaging in biophotonics. *IEEE J. Sel. Top. in Quantum Electron.*, 20(2):50–60, mar 2014.

[30] D. G. Ouzounov, Tianyu Wang, Mengran Wang, D. D. Feng, N. G. Horton, J. C. Cruz-Hernández, Y.-T. Cheng, J. Reimer, A. S. Tolias, N. Nishimura, and C. Xu. *In vivo* three-photon imaging of activity of GCaMP6-labeled neurons deep in intact mouse brain. *Nat. Methods*, 14(4):388–390, 2017.

[31] L.-C. Cheng, N. G. Horton, K. Wang, S.-J. Chen, and C. Xu. Measurements of multiphoton action cross sections for multiphoton microscopy. *Biomed. Opt. Express*, 10(5):3427–3433, 2014.

[32] P. F. Moulton. Spectroscopic and laser characteristics of Ti:Al_2O_3. *J. Opt. Soc. Am. B*, 1(3):125–133, 1986.

[33] S. Huang, A. A. Heikal, and W. W. Webb. Two-photon fluorescence spectroscopy and microscopy of NAD(P)H and flavoprotein. *Biophys. J.*, 82(5):2811–2825, 2002.

[34] W. R. Zipfel, R. M. Williams, R. Christie, A. Y. Nikitin, B. T. Hyman, and W. W. Webb. Live tissue intrinsic emission microscopy using multiphoton-excited native fluorescence and second harmonic generation. *Proc. Natl. Acad. Sci. U.S.A.*, 100(12):7075–7080, 2003.

[35] M. Drobizhev, N. S. Makarov, S. E. Tillo, T. E. Hughes, and A. Rebane. Two-photon absorption properties of fluorescent proteins. *Nat. Methods*, 8(5):393–399, 2011.

[36] V. Petricevic, S. K. Gayen, Alfano R. R., Kiyoshi Yamagishi, H. Anzai, and Y. Yamaguchi. Laser action in chromium-doped forsterite. *Appl. Phys. Lett.*, 13(52):1040–1042, 1988.

[37] A. Agnesi, E. Piccinini, and G. C. Reali. Influence of thermal effects in Kerr-lens mode-locked femtosecond Cr^{4+}:forsterite lasers. *Opt. Commun.*, 135(1–3):77–82, 1997.

[38] C.-K. Sun, C.-C. Chen, S.-W. Chu, T.-H. Tsai, Y.-C. Chen, and B.-L. Lin. Multiharmonic-generation biopsy of skin. *Opt. Lett.*, 28(24):2488–2490, 2003.

[39] T. Yasui, Y. Takahashi, M. Ito, S. Fukushima, and T. Araki. *Ex vivo* and *in vivo* second-harmonic-generation imaging of dermal collagen fiber in skin: comparison of imaging characteristics between mode-locked Cr:forsterite and Ti:sapphire lasers. *Appl. Opt.*, 48:D88–D95, 2009.

[40] K. Tamura, Y. Kimura, and M. Nakazawa. Femtosecond pulse generation over 82 nm wavelength span from passively mode locked erbium-doped fiber laser. *Electron. Lett.*, 31(13):1062–1063, 1995.

[41] A. C. Millard, P. W. Wiseman, D. N. Fittinghoff, K. R. Wilson, J. A. Squier, and M. Müller. Third-harmonic generation microscopy by use of a compact, femtosecond fiber laser source. *Appl. Opt.*, 38(36):7393–7397, 1999.

[42] M. Yildirim, N. Durr, and A. Ben-Yakar. Tripling the maximum imaging depth with third-harmonic generation microscopy. *J. Biomed. Opt.*, 20(9):096013, 2015.

[43] T. Gottschall, T. Meyer, M. Schmitt, J. Popp, J. Limpert, and A. Tünnermann. Four-wave-mixing-based optical parametric oscillator delivering energetic, tunable, chirped femtosecond pulses for non-linear biomedical applications. *Opt. Express*, 23(18):23968, 2015.

[44] M. Brinkmann, S. Dobner, and C. Fallnich. Light source for narrow and broadband coherent Raman scattering microspectroscopy. *Opt. Lett.*, 23(40):5447–5450, 2015.

[45] F. Tauser, F. Adler, and A. Leitenstorfer. Widely tunable sub-30-fs pulses from a compact erbium-doped fiber source. *Opt. Lett.*, 29(5):516–518, 2004.

[46] J. Takayanagi, T. Sugiura, M. Yoshida, and N. Nishizawa. 1.0-1.7-μm wavelength-tunable ultrashort-pulse generation using femtosecond Yb-doped fiber laser and photonic crystal fiber. *IEEE Photon. Technol. Lett.*, 18(21):2284–2286, 2006.

[47] H.-W. Chen, Z. Haider, J. Lim, S. Xu, Z. Yang, F. X. K artner, and Guoqing Chang. 3 GHz, Yb-fiber laser-based, few-cycle ultrafast source at the Ti:sapphire laser wavelength. *Opt. Lett.*, 22(38):4927–4930, 2013.

[48] H Tu, J. Laegsgaard, R Zhang, S Tong, Y Liu, and S. A. Boppart. Bright broadband coherent fiber sources emitting strongly blue-shifted resonant dispersive wave pulses. *Opt. Express*, 21(20):23188–23196, 2013.

[49] M.-C. Chan, C.-H. Lien, J.-Y. Lu, and B.-H. Lyu. High power NIR fiber-optic femtosecond Cherenkov radiation and its application on nonlinear light microscopy. *Opt. Express*, 22(8):9498, 2014.

[50] Hsien Yi Wang, Shiuan Wen Huang, Dean Ru Li, Bor Shyh Lin, and M.-C. Chan. Nonlinear light microscopy by a 1.2-μm fiber-laser-based femtosecond dispersive wave source. *IEEE Photon. J.*, 7(3), 2015.

[51] K.-C. Li, Lynn L. H. Huang, J.-H. Liang, and M.-C. Chan. Simple approach to three-color two-photon microscopy by a fiber-optic wavelength convertor. *Biomed. Opt. Express*, 7(11):4803, 2016.

[52] Hao Luo, Li Zhan, Zhiqiang Wang, Liang Zhang, Cheng Feng, and Xuehao Shen. All-fiber generation of sub-30 fs pulses at 1.3-μm via Cherenkov radiation with entire dispersion management. *J. Light.Technol.*, 35(11):2325–2330, 2017.

[53] H. Lim, J. Buckley, A. Chong, and F. W. Wise. Fibre-based source of femtosecond pulses tunable from 1.0 to 1.3 μm. *Electron. Lett.*, 24(40):1523–1525, 2004.

[54] K. Wang and C. Xu. Tunable high-energy soliton pulse generation from a large-mode-area fiber and its application to third harmonic generation microscopy. *Appl. Phys. Lett.*, 99(7):2009–2012, 2011.

[55] Xiao Hui Fang, M. Lie Hu, Bo Wen Liu, L. Chai, Ching Yue Wang, Hui Feng Wei, Wei Jun Tong, J. Luo, C.-K. Sun, A. A. Voronin, and A. M. Zheltikov. An all-photonic-crystal-fiber wavelength-tunable source of high-energy sub-100 fs pulses. *Opt. Commun.*, 289:123–126, 2013.

[56] M.-C. Chan and M.-T. Tsai. Simultaneous 0.8, 1.0, and 1.3 μm multispectral and common-path broadband source for optical coherence tomography. *Opt. Lett.*, 4(39):865–868, 2014.

[57] S. R. Domingue and R. A. Bartels. Three-photon excitation source at 1250 nm generated in a dual zero dispersion wavelength nonlinear fiber. *Opt. Express*, 22(25):30777, 2014.

[58] J. Lim, H.-W. Chen, S. Xu, Z. Yang, Guoqing Chang, and F. X. K artner. 3 GHz, watt-level femtosecond Raman soliton source. *Opt. Lett.*, 7(39):2060–2063, 2014.

[59] H. Kawagoe, S. Ishida, M. Aramaki, Y. Sakakibara, E. Omoda, H. Kataura, and N. Nishizawa. Development of a high power supercontinuum source in the 1.7 μm wavelength region for highly penetrative ultrahigh-resolution optical coherence tomography. *Biomed. Opt. Express*, 3(5):932–943, 2014.

[60] Yuhong Yao, G. P. Agrawal, and W. H. Knox. Yb:fiber laser-based, spectrally coherent and efficient generation of femtosecond 13-μm pulses from a fiber with two zero-dispersion wavelengths. *Opt. Lett.*, 40(15):3631, 2015.

[61] J. W. Nicholson, A. Desantolo, W. Kaenders, and A. Zach. Self-frequency-shifted solitons in a polarization-maintaining, very-large-mode area, Er-doped fiber amplifier. *Opt. Express*, 24(20):23396, 2016.

[62] P. Cadroas, L. Abdeladim, L. Kotov, M. Likhachev, D. Lipatov, D. Gaponov, A. Hideur, M. Tang, J. Livet, W. Supatto, E. Beaurepaire, and S. Février. All-fiber femtosecond laser providing 9 nJ, 50 MHz pulses at 1650 nm for three-photon microscopy. *J. Opt.*, 19(6):65506, 2017.

[63] Jay R Unruh, E S Price, Roque G Molla, Lisa Stehno-Bittel, Carey K Johnson, and Rongqing Hui. Two-photon microscopy with wavelength switchable fiber laser excitation. *Optics express*, 14(21):9825–9831, 2006.

[64] K. Wang, T.-M. Liu, J. Wu, N. G. Horton, C. P. Lin, and C. Xu. Three-color femtosecond source for simultaneous excitation of three fluorescent proteins in two-photon fluorescence microscopy. *Biomed. Opti. Express*, 3(9):1972–1977, sep 2012.

[65] J.-Y. Huang, L.-Z. Guo, J.-Z. Wang, T.-C. Li, H.-J. Lee, P.-K. Chiu, L.-H. Peng, and T.-M. Liu. Fiber-based 1150-nm femtosecond laser source for the minimally invasive harmonic generation microscopy. *J. Biomed. Opt.*, 22(3):36008, 2017.

[66] B. Li, Mengran Wang, K. Charan, M.-J. Li, and C. Xu. Investigation of the long wavelength limit of soliton self-frequency shift in a silica fiber. *Opt. Express*, 26(15):19637, 2018.

[67] G. P. Agrawal. *Nonlinear fiber optics.* Academic press, 2007.

[68] J. V. Howe, J. H. Lee, Shian Zhou, and F. Wise. Demonstration of soliton self-frequency shift below 1300nm in higher-order mode, solid silica-based fiber. *Opt. Lett.*, 32(4):340–342, 2007.

[69] M. E.V. Pedersen, J. Cheng, K. Charan, K. Wang, C. Xu, L. Grüner-Nielsen, and D. Jakobsen. Higher-order-mode fiber optimized for energetic soliton propagation. *Opt. Lett.*, 37(16):3459, 2012.

[70] L. Rishoj, G. Prabhakar, J. Demas, and S. Ramachandran. 30 nJ, ˜50 fs all-fiber source at 1300 nm using soliton shifting in LMA HOM fiber. *Conference on Lasers and Electro-Optics*, (c):STh3O.3, 2016.

[71] L. Rishøj, B. Tai, P. Kristensen, and S. Ramachandran. Characterization of intermodal group index matched soliton interactions leading to MW peak powers at 1300 nm. *Conference on Lasers and Electro-Optics*, (c):22–23, 2017.

[72] W. Liu, Zhigang Zhang, F. X. Kärtner, and Guoqing Chang. Self-phase modulation enabled, wavelength- tunable ultrafast fiber laser sources: an energy scalable approach. *Opt. Express*, 14(24):15328–15340, 2016.

[73] W. Liu, S.-H. Chia, H.-Y. Chung, R. Greinert, F. X. Kärtner, and Guoqing Chang. Energetic ultrafast fiber laser sources tunable in 1030–1215 nm for deep tissue multi-photon microscopy. *Opt. Express*, 25(6):6822, 2017.

[74] Fuzeng Niu, Jiayin Li, W. Yang, Zhigang Zhang, and Aimin Wang. Fiber-Based High-Energy Femtosecond Pulses Tunable From 920 to 1030 nm for two-photon microscopy. *IEEE Photon. Technol. Lett.*, 30(16):1479–1482, 2018.

[75] R. H. Stolen and C. Lin. Self-phase-modulation in silica optical fibers. *Phys. Rev. A*, 17(4):1448–1453, 1978.

[76] P. Mamyshev. All optical data regeneration based on self-phase modulation effect. *ECOC*, 98:475–476, 1998.

[77] T. Her, G. Raybon, and C. Headley. Optimization of pulse regeneration at 40 Gb/s based on spectral filtering of self-phase modulation in fiber. *Phton. Technol. Lett.*, 16:200, 2004.

[78] L. B. Fu, M. Rochette, V. G. Ta'eed, D. J. Moss, and B. J. Eggleton. Investigation of self-phase modulation based optical regeneration in single mode As_2Se_3 chalcogenide glass fiber. *Opt. Express*, 13(19):7637–7644, 2005.

[79] R. Lehneis, Steinmetz A., J. Limpert, and A. Tünnerman. All-fiber pulse shortening of passively Q-switched microchip laser pulses down to sub-200 fs. *Opt. Lett.*, 39(20):5806–5808, 2014.

[80] W. Fu, L. G. Wright, and F. W. Wise. High-power femtosecond pulses without a modelocked laser. *Optica*, 4(7):831–834, 2017.

[81] J. Buldt, M. Müller, R. Klas, T. Eidam, J. Limpert, and A. Tünnermann. Temporal contrast enhancement of energetic laser pulses by filtered self-phase-modulation-broadened spectra. *Opt. Lett.*, 42(19):3761–3764, 2017.

[82] K. Regelskis, J. Želudevičius, K. Viskontas, and G. Račiukaitis. Ytterbium-doped fiber ultrashort pulse generator based on self-phase modulation and alternating spectral filtering. *Opt. Lett.*, 40(22):5255–5258, 2015.

[83] Z. Liu, M. Ziegler, L. G. Wright, and F. W. Wise. Megawatt peak power from a Mamyshev oscillator. *Optica*, 4(6):649–654, 2017.

[84] S. W. Hell, K. Bahlmann, M. Schrader, H. M. Soini, A. Malak, I. Gryczynski, and J. R. Lakowicz. Three-photon excitation in fluorescence microscopy. *J. Biomed. Opt.*, 1(1):71–74, 1996.

[85] J. M. Dudley, G. Genty, and S. Coen. Supercontinuum generation in photonic crystal fiber. *Rev. Mod. Phys.*, 78(4):1135–1184, 2006.

[86] D. Strickland and G. Mourou. Compression of amplified chirped optical pulses. *Opt. Commun.*, 3(56):219–221, 1985.

[87] Grzegorz Sobon, Pawel R. Kaczmarek, Dorota Sliwinska, Jaroslaw Sotor, and Krzysztof M. Abramski. High-Power Fiber-Based Femtosecond CPA System at 1560 nm. *IEEE Journal on Selected Topics in Quantum Electronics*, 20(5), 2014.

[88] Hongjie Wang, Leonid V. Kotov, Dmitry A. Gaponov, Amélie Cabasse, Mikhail V. Yashkov, Denis S. Lipatov, Mikhail E. Likhachev, Jean Louis Oudar, Gilles Martel, Sébastien Février, and Ammar Hideur. Dissipative Soliton Generation and Amplification in Erbium-Doped Fibers Operating at 1.55 μm. *IEEE Journal on Selected Topics in Quantum Electronics*, 20(5), 2014.

[89] Ihor Pavlov, Emrah Ilbey, Ebru Dülgergil, Alper Bayri, and F Ömer Ilday. High-power high-repetition-rate single-mode Er-Yb-doped fiber laser system. *Optics Express*, 20(9):9471–9475, 2012.

[90] Wen Dai, Youjian Song, Bo Xu, Amos Martinez, Shinji Yamashita, Minglie Hu, and Chyingyue Wang. High-power sub-picosecond all-fiber laser source at 1.56 μm. *Chinese Optics Letters*, 11(12):111402–, 2014.

[91] P. Elahi, H. Kalaycıoğlu, H. Li, Ö. Akçaalan, and F.Ö. Ilday. 175 fs-long pulses from a high-power single-mode Er-doped fiber laser at 1550 nm. *Optics Communications*, 403(July):381–384, 2017.

[92] Franck Morin, Frédéric Druon, Marc Hanna, and Patrick Georges. Microjoule femtosecond fiber laser at 1.6 μm for corneal surgery applications. 34(13):1991–1993, 2009.

[93] Grzegorz Sobon, Pawel Kaczmarek, Aleksander Gluszek, Jaroslaw Sotor, and Krzysztof M. Abramski. μj-level, kHz-repetition rate femtosecond fiber-CPA system at 1555 nm. *Optics Communications*, 347:8–12, 2015.

[94] Xiang Peng, Kyungbum Kim, Michael Mielke, Stephen Jennings, Gordon Masor, Dave Stohl, Arturo Chavez-Pirson, Dan T. Nguyen, Dan Rhonehouse, Jie Zong, Dmitriy Churin, and N. Peyghambarian. Monolithic fiber chirped pulse amplification system for millijoule femtosecond pulse generation at 1.55 μm. *Optics Express*, 22(3):2459, 2014.

[95] C. Xu, W. Zipfel, J. B. Shear, R. M. Williams, and W. W. Webb. Multiphoton fluorescence excitation: new spectral windows for biological nonlinear microscopy. *Proc. Natl. Acad. Sci. U.S.A.*, 93(20):10763–10768, 1996.

[96] R. R. Anderson and J. A. Parrish. The optics of human skin. *J. Invest. Dermatol.*, 77(1):13–19, 1981.

[97] German Centre for Cancer Registry Data. *Cancer in Germany 2011/2012*. Robert Koch Institute, 2016.

[98] J. G. Fujimoto, M. E. Brezinski, G. J. Tearney, S. A. Boppart, B. Bouma, M. R. Hee, J. F. Southern, and E. A. Swanson. Optical biopsy and imaging using optical coherence tomography. *Nat. Med.*, 1(9):970–972, 1995.

[99] G. J. Tearney, M. E. Brezinski, J. F. Southern, B. E. Bouma, S. A. Boppart, and J. G. Fujimoto. Optical biopsy in human pancreatobiliary tissue using optical coherence tomography. *Dig. Dis. Sci.*, 43(6):1193–1199, 1998.

[100] T. Gambichler, P. Regeniter, F. G. Bechara, A. Orlikov, R. Vasa, G. Moussa, M. Stücker, P. Altmeyer, and K. Hoffmann. Characterization of benign and malignant melanocytic skin lesions using optical coherence tomography *in vivo*. *J. Am. Acad. Dermatol.*, 57(4):629–637, 2007.

[101] M. Rajadhyaksha, M. Grossman, D. Esterowitz, R. H. Webb, and R. R. Anderson. *In vivo* confocal scanning laser microscopy of human skin: Melanin provides strong contrast. *J. Invest. Dermatol.*, 104(6):946–952, 1995.

[102] P. J. Caspers, G. W. Lucassen, and Gerwin J. Puppels. Combined *in vivo* confocal Raman spectroscopy and confocal microscopy of human skin. *Biophys. J.*, 85(1):572–580, 2003.

[103] G. Pellacani, A. Maria Cesinaro, and S. Seidenari. Reflectance-mode confocal microscopy of pigmented skin lesions–improvement in melanoma diagnostic specificity. *J. Am. Acad. Dermatol.*, 53(6):979–985, 2005.

[104] M. Ulrich, A. Maltusch, F. Rius-Diaz, J. Röwert-Huber, S. González, W. Sterry, E. Stockfleth, and S. Astner. Clinical applicability of *in vivo* reflectance confocal microscopy for the diagnosis of actinic keratosis. *Dermatol. Surg.*, 34(5):610–619, 2008.

[105] K. M. Hanson and C. J. Bardeen. Application of nonlinear optical microscopy for imaging skin. *Photochem. Photobiol.*, 85(1):33–44, 2009.

[106] B. R. Masters, P. T. So, and E. Gratton. Multiphoton excitation fluorescence microscopy and spectroscopy of *in vivo* human skin. *Biophys. J.*, 72(6):2405–2412, 1997.

[107] K. König and I. Riemann. High-resolution multiphoton tomography of human skin with subcellular spatial resolution and picosecond time resolution. *J. Biomed. Opt.*, 8(3):432, 2003.

[108] K. König, A. Ehlers, F. Stracke, and I. Riemann. *In vivo* drug screening in human skin using femtosecond laser multiphoton tomography. *Skin Pharmacol. Physiol.*, 19(2):78–88, 2006.

[109] K. König, A. Ehlers, I. Riemann, S. Schenkl, R. Bückle, and M. Kaatz. Clinical two-photon microscopy. *Microsc. Res. Tech.*, 70(5):398–402, 2007.

[110] J. Paoli, M. Smedh, A. M. Wennberg, and M. B. Ericson. Multiphoton laser scanning microscopy on non-melanoma skin cancer: Morphologic features for future non-invasive diagnostics. *J. Invest. Dermatol.*, 128(5):1248–1255, 2008.

[111] H. G. Breunig, H. Studier, and K. König. Multiphoton excitation characteristics of cellular fluorophores of human skin *in vivo*. *Opt. Express*, 18(8):7857, 2010.

[112] Hassan Ait El Madani, E. Tancréde-Bohin, A. Bensussan, A. Colonna, A. Dupuy, M. Bagot, and A.-M. Pena. *In vivo* multiphoton imaging of human skin: assessment of topical corticosteroid-induced epidermis atrophy and depigmentation. *J. Biomed. Opt.*, 17(2):026009, 2012.

[113] M. Balu, A. Mazhar, C. K. Hayakawa, R. Mittal, T. B. Krasieva, K. König, V. Venugopalan, and B. J. Tromberg. *In vivo* multiphoton NADH fluorescence reveals depth-dependent keratinocyte metabolism in human skin. *Biophys. J.*, 104(1):258–267, 2013.

[114] E. Brown, T. McKee, E. DiTomaso, A. Pluen, B. Seed, Y. Boucher, and R. K. Jain. Dynamic imaging of collagen and its modulation in tumors *in vivo* using second-harmonic generation. *Nat. Med.*, 9(6):796–800, 2003.

[115] C.-K. Sun, C.-C. Chen, S.-W. Chu, T.-H. Tsai, Y.-C. Chen, and B.-L. Lin. Multiharmonic-generation biopsy of skin. *Opt. Lett.*, 28(24):2488–2490, Dec 2003.

[116] S.-P. Tai, T.-H. Tsai, W.-J. Lee, D.-B. Shieh, Y.-H. Liao, H.-Y. Huang, K. Y.-J. Zhang, H.-L. Liu, and C.-K. Sun. Optical biopsy of fixed human skin with backward-collected optical harmonics signals. *Opt. Express*, 13(20):8231–8242, Oct 2005.

[117] S.-Y. Chen, H.-Y. Wu, and C.-K. Sun. *In vivo* harmonic generation biopsy of human skin. *J. Biomed. Opt.*, 14(6):060505, 2009.

[118] S.-Y. Chen, Chen S.-U., Wu H.-Y., W.-J. Lee, Y.-H. Liao, and C.-K. Sun. *In vivo* virtual biopsy of human skin by using noninvasive higher harmonic generation microscopy. *IEEE J. Sel. Top. in Quantum Electron.*, 16(3):478–492, 2010.

[119] M.-R. Tsai, S.-Y. Chen, D.-B. Shieh, P.-J. Lou, and C.-K. Sun. *In vivo* optical virtual biopsy of human oral mucosa with harmonic generation microscopy. *Biomed. Opt. Express*, 2(8):2317, 2011.

[120] R. P. Judy, J. J. Keating, E. M. DeJesus, J. X. Jiang, O. T. Okusanya, S. Nie, D. E. Holt, S. P. Arlauckas, P. S. Low, E. J. Delikatny, and S. Singhal. Quantification of tumor fluorescence during intraoperative optical cancer imaging. *Sci. Rep.*, 5:16208, 2015.

[121] P. P. Provenzano, K. W. Eliceiri, J. M. Campbell, D. R. Inman, J. G. White, and P. J. Keely. Collagen reorganization at the tumor-stromal interface facilitates local invasion. *BMC Med.*, 4(1):38, 2006.

[122] J. R. W. Conway, N. O. Carragher, and P. Timpson. Developments in preclinical cancer imaging: innovating the discovery of therapeutics. *Nat. Rev. Cancer*, 14(5):314–328, 2014.

[123] S.-J. Lin, S.-H. Jee, C.-J. Kuo, R.-J. Wu, W.-C. Lin, J.-S. Chen, Y.-H. Liao, C.-J. Hsu, T.-F. Tsai, Y.-F. Chen, and C.-Y. Dong. Discrimination of basal cell carcinoma from normal dermal stroma by quantitative multiphoton imaging. *OpT. Lett.*, 31(18):2756, 2006.

[124] R. Cicchi, D. Massi, S. Sestini, P. Carli, V. De Giorgi, T. Lotti, and F. S. Pavone. Multidimensional non-linear laser imaging of Basal Cell Carcinoma. *Opt. Express*, 15(16):10135–10148, 2007.

[125] T. Hompland, A. Erikson, M. Lindgren, T. Lindmo, and C. de Lange Davies. Second-harmonic generation in collagen as a potential cancer diagnostic parameter. *J. Biomed. Opt.*, 13(5):054050, 2008.

[126] O. Nadiarnykh, R. B. LaComb, M. A. Brewer, and P. J. Campagnola. Alterations of the extracellular matrix in ovarian cancer studied by Second Harmonic Generation imaging microscopy. *BMC Cancer*, 10:94, 2010.

[127] P. Campagnola. Second harmonic generation imaging microscopy: Applications to diseases diagnostics. *Anal. Chem.*, 83(9):3224–3231, 2012.

[128] Xiyi Chen, O. Nadiarynkh, S. Plotnikov, and P. J Campagnola. Second harmonic generation microscopy for quantitative analysis of collagen fibrillar structure. *Nat. Protoc.*, 7(4):654–669, 2012.

[129] C. Thrasivoulou, G. Virich, T. Krenacs, I. Korom, and D. L. Becker. Optical delineation of human malignant melanoma using second harmonic imaging of collagen. *Biomed. Opt. express*, 2(5):1282–1295, 2011.

[130] Jian Xu, Deyong Kang, Yaping Zeng, Shuangmu Zhuo, Xiaoqin Zhu, Liwei Jiang, Jianxin Chen, and Jiangbo Lin. Multiphoton microscopy for label-free identification of intramural metastasis in human esophageal squamous cell carcinoma. *Biomed. Opt. Express*, 8(7):537–542, 2017.

[131] B. Weigelin, G.-J. Bakker, and P. Friedl. Intravital third harmonic generation microscopy of collective melanoma cell invasion. *IntraVital*, 1(1):32–43, 2012.

[132] N. V. Kuzmin, P. Wesseling, P. C. de Witt Hamer, D. P. Noske, G. D. Galgano, H. D. Mansvelder, J. C. Baayen, and M. L. Groot. Third harmonic generation imaging for fast, label-free pathology of human brain tumors. *Biomed. Opt. Express*, 7(5):1889, 2016.

[133] Y.-H. Liao, S.-Y. Chen, S.-Y. Chou, P.-H. Wang, M.-R. Tsai, and C.-K. Sun. Determination of chronological aging parameters in epidermal keratinocytes by *in vivo* harmonic generation microscopy. *Biomed. Opt. Express*, 4(1):77–88, 2013.

[134] Yuxin Wang, K. Wang, Wenhui Wen, P. Qiu, and K. Wang. Comparison of Signal Detection of GaAsP and GaAs PMTs for Multiphoton Microscopy at the 1700-nm window. *IEEE Photon. J.*, 8(3), 2016.

[135] Linhong Kou, Daniel Labrie, and Petr Chylek. Refractive indices of water and ice in the 065- to 25-μm spectral range. *Appl. Opt.*, 32(19):3531–3540, 1993.

[136] M. J. Mendenhall, A. S. Nunez, and R. K. Martin. Human skin detection in the visible and near infrared. *Appl. Opt.*, 54(35):10559–10570, 2015.

[137] C.-S. Hsieh, S.-U. Chen, Y.-W. Lee, and C.-K. Sun. Higher harmonic generation microscopy of *in vitro* cultured mammal oocytes and embryos. *Opt. Express*, 16(15):11574–11588, 2008.

[138] R. D. Schaller, J. C. Johnson, and R. J. Saykally. Nonlinear chemical imaging microscopy: Near-field third harmonic generation imaging of human red blood cells. *Anal. Chem.*, 72(21):5361–5364, 2000.

[139] D. Débarre, W. Supatto, A.-M. Pena, A. Fabre, T. Tordjmann, L. Combettes, M.-C. Schanne-Klein, and E. Beaurepaire. Imaging lipid bodies in cells and tissues using third-harmonic generation microscopy. *Nat. Methods*, 3(1):47–53, 2006.

[140] S.-W. Chu, I.-S. Chen, T.-M. Liu, C.-K. Sun, S.-P. Lee, B.-L. Lin, P.-C. Cheng, M.-X. Kuo, D.-J. Lin, and H.-L. Liu. Nonlinear bio-photonic crystal effects revealed with multi-modal nonlinear microscopy. *J. Microsc.*, 208(3):190–200, 2002.

[141] S.-W. Chu, S.-Y. Chen, T.-H. Tsai, T.-M. Liu, C.-Y. Lin, H.-J. Tsai, and C.-K. Sun. *In vivo* developmental biology study using noninvasive multi-harmonic generation microscopy. *Opt. Express*, 11(23):3093–3099, 2003.

[142] C.-K. Sun, S.-W. Chu, S.-Y. Chen, T.-H. Tsai, T.-M. Liu, C.-Y. Lin, and H.-J. Tsai. Higher harmonic generation microscopy for developmental biology. *J. Struct. Biol.*, 147(1):19–30, 2004.

[143] L. Canioni, S. Rivet, L. Sarger, R. Barille, P. Vacher, and P. Voisin. Imaging of Ca^2+ intracellular dynamics with a third-harmonic generation microscope. *Opt. Lett.*, 26(8):515, 2001.

[144] D. Kobat, M. E. Durst, N. Nishimura, A. W. Wong, C. B. Schaffer, and C. Xu. Deep tissue multiphoton microscopy using longer wavelength excitation. *Opt. Express*, 17(16):13354, 2009.

[145] M.-T. Tsai, D.-R. Li, and M.-C. Chan. Non-invasive image-guided laser microsurgery by a dual-wavelength fiber laser and an integrated fiber-optic multi-modal system. *Opt. Lett.*, 41(20):4847–4850, 2016.

[146] http://www.hamamatsu.com/us/en/index.html.

[147] Huafeng Ding, Jun Q. Lu, W. A. Wooden, P. J. Kragel, and Xin Hua Hu. Refractive indices of human skin tissues at eight wavelengths and estimated dispersion relations between 300 and 1600 nm. *Phys. Med. Biol.*, 51(6):1479–1489, 2006.

[148] A. V. Smith, B. T. Do, G. R. Hadley, and R. L. Farrow. Optical damage limits to pulse energy from fibers. *IEEE J. Sel. Top. in Quantum Electron.*, 15(1):153–158, 2009.

[149] K. König, P. T. C. So, W. W. Mantulin, and E. Gratton. Cellular response to near-infrared femtosecond laser pulses in two-photon microscopes. *Opt. Lett.*, 22(2):135, 1997.

[150] https://www.skincancer.org/prevention/uva-and-uvb.

[151] F. Aptel, N. Olivier, A. Deniset-Besseau, J. M. Legeais, K. Plamann, M. C. Schanne-Klein, and E. Beaurepaire. Multimodal nonlinear imaging of the human cornea. *Invest. Ophthalmol. Vis. Sci.*, 51(5):2459–2465, 2010.

[152] S. Witte, A. Negrean, J. C. Lodder, C. P. J. de Kock, G. Testa Silva, H. D. Mansvelder, and M. Louise Groot. Label-free live brain imaging and targeted patching with third-harmonic generation microscopy. *Proc. Natl. Acad. Sci. U.S.A.*, 108(15):5970–5975, 2011.

[153] B. Weigelin, G.-J. Bakker, and P. Friedl. Third harmonic generation microscopy of cells and tissue organization. *J. Cell Sci.*, 129(2):245–255, 2016.

[154] A. Hariharan, M. E. Fermann, M. L. Stock, D. J. Harter, and J. Squier. Alexandrite-pumped alexandrite regenerative amplifier for femtosecond pulse amplification. *Opt. Lett.*, 21(2):128–130, 1996.

[155] A. Atbot, A. Arbor, and S. Diego. Injection of ultrafast regenerative amplifiers with low energy femtosecond pulses from an er-doped fiber laser. *Opt. Commun.*, 132:469–473, 1996.

[156] D Träutlein, F Adler, K Moutzouris, a Jeromin, a Leitenstorfer, and E Ferrando-May. Highly versatile confocal microscopy system based on a tunable femtosecond Er:fiber source. *Journal of biophotonics*, 1(1):53–61, 2008.

[157] Lin Huang, Arthur K. Mills, Yuan Zhao, David J. Jones, and Shuo Tang. Miniature fiber-optic multiphoton microscopy system using frequency-doubled femtosecond Er-doped fiber laser. *Biomedical Optics Express*, 7(5):1948, 2016.

[158] Yuan Liu, Haohua Tu, and Stephen a. Boppart. Wave-breaking-extended fiber supercontinuum generation for high compression ratio transform-limited pulse compression. *Optics Letters*, 37(12):2172, 2012.

[159] J. Law. The development of specialties in science: the case of X-ray protein crystallography. *Sci. Stud.*, 3(3):275–303, 1978.

[160] E. Pennisi. Taking a structured approach to understanding proteins. *Science*, 279:978–979, 1998.

[161] K. Dierks, A. Meyer, D. Oberthür, G. Rapp, H. Einspahr, and C. Betzel. Efficient UV detection of protein crystals enabled by fluorescence excitation at wavelengths longer than 300 nm. *Acta. Cryst.*, F66:478–484, 2010.

[162] L. M. Haupert, E. L. DeWalt, and G. J. Simpson. Modeling the SHG activities of diverse protein crystals. *Acta. Cryst.*, D68:1513–1521, 2012.

[163] J. A. Newman and G. J. Simpson. Nonlinear optical characterization of membrane protein microcrystals and nanocrystals. *Adv. Exp. Med. Biol.*, 922:91–103, 2016.

[164] M. T. Neves-Petersen, S. Petersen, and G. P. Gajula. UV light effects on proteins: from photochemistry to nanomedicine. *Mol. Photochem.*, pages 125–158, 2012.

[165] D. J. Kissick, D. Wanapun, and G. J. Simpson. Second-order nonlinear optical imaging of chiral crystals. *Annu. Rev. Anal. Che.*, 4(1):419–437, 2011.

[166] L. M. Haupert and G. J. Simpson. Screening of protein crystallization trials by second order nonlinear optical imaging of chiral crystals (SONICC). *Methods*, 55(4):379–386, 2011.

[167] R. W. Terhune, P. D. Maker, and C. M. Savage. Optical harmonic generation in calcite. *Physc. Rev. Lett.*, 8(10):404–406, 1953.

[168] M. C. Skala, K. M. Riching, A. Gendron-Fitzpatrick, J. Eickhoff, K. W. Eliceiri, J. G. White, and N. Ramanujam. *In vivo* multiphoton microscopy of NADH and FAD redox states, fluorescence lifetimes, and cellular morphology in precancerous epithelia. *Proc. Natl. Acad. Sci. U.S.A.*, 104(49):19494–19499, 2007.

[169] P. S. Tsai, B. Friedman, A. I. Ifarraguerri, B. D. Thompson, V. Lev-Ram, C. B. Schaffer, Q. Xiong, R. Y. Tsien, J. A. Squier, and D. Kleinfeld. All-optical histology using ultrashort laser pulses. *Neuron*, 39(1):27–41, 2003.